

RCA

Review

September 1973 Volume 34 No. 3

RCAR 34(3) 383-550 (1973)

RCA Review, published quarterly in March, June, September and December by RCA Research and Engineering, RCA Corporation, Princeton, New Jersey 08540. Entered as second class matter July 3, 1950 under the Act of March 3, 1879. Second-class postage paid at Princeton, New Jersey, and at additional mailing offices. Effective Jan. 1, 1971, subscription rates as follows: United States and Canada: one year \$6.00, two years \$10.50, three years \$13.50; in other countries, one year \$6.40, two years \$11.30, three years \$14.70. Single copies (except for special issues) up to five years old \$3.00.

RCA Review

A technical journal published quarterly
by RCA Research and Engineering
in cooperation with the subsidiaries
and divisions of RCA.

Contents

- 385** Lensless Optical Detection of Bubble Domains
R. Shahbender and J. Druguet
- 401** Vented-Bore He-Cd Lasers
K. G. Hernqvist
- 408** Scanning-Beam Performance from a Negative-Electron-Affinity Activated
Silicon Cold Cathode
A. D. Cope, E. Luedicke, and J. P. Carroll
- 429** Field-Effect Electroluminescence in Silicon
A. M. Goodman
- 442** Negative Resistance in Cadmium Selenide Powder—Relative Absorption
Coefficient
L. J. Nicastro and E. L. Offenbacher
- 457** Space-Charge Instabilities in Transferred Electron Devices
B. S. Perlman
- 489** Millimeter-Wave Phase Shifter
B. J. Levin and G. G. Weidner
- 506** Design of a Light-Weight Microwave Repeater for a 24-Channel Domestic
Satellite System
M. V. O'Donovan, C. M. Kudsia, and L. A. Keyes
- 539** Technical Papers
- 542** Patents
- 545** Authors

RCA Corporation

Robert W. Sarnoff Chairman of the Board and Chief Executive Officer
A. L. Conrad President and Chief Operating Officer

Editorial Advisory Board

Chairman, J. A. Rajchman RCA Laboratories

E. D. Becken RCA Global Communications
G. D. Cody RCA Laboratories
A. N. Goldsmith Honorary Vice President
N. L. Gordon RCA Laboratories
G. B. Herzog RCA Laboratories
J. Hillier RCA Research and Engineering
E. O. Johnson International Licensing
J. Kurshan RCA Laboratories
D. S. McCoy Consumer Electronics
H. F. Olson RCA Laboratories
K. H. Powers RCA Laboratories
R. E. Quinn RCA Laboratories
P. Rappaport RCA Laboratories
L. A. Shottliff International Licensing
T. O. Stanley RCA Laboratories
F. Sterzer RCA Laboratories
J. J. Tietjen RCA Laboratories
W. M. Webster RCA Laboratories

Secretary, Charles C. Foster RCA Laboratories

Editor Ralph F. Ciafone

Associate Editors

W. A. Chisholm RCA Limited (Canada)
M. G. Gander RCA Service Company
W. O. Hadlock RCA Research and Engineering
D. R. Higgs Missile and Surface Radar Division
W. A. Howard National Broadcasting Company
C. Hoyt Consumer Electronics Company
E. McElwee Solid-State Division
C. A. Meyer Electronic Components
M. G. Pietz Government and Commercial Systems
C. W. Sall RCA Laboratories
I. M. Seideman Astro-Electronics Division
R. N. Hurst Communications Systems Division

© RCA Corporation 1973 All Rights Reserved Printed in USA

Lensless Optical Detection of Bubble Domains

R. Shahbender and J. Druguet

RCA Laboratories, Princeton, N. J.

Abstract—A lens-less, all-solid-state optical detection technique for cylindrical "bubble" domains represents an attractive alternative for data readout in bubble domain devices. An edge-emitting light emitting diode is used to illuminate the bubble garnet film through a defining aperture and a polarizer. The beam emerging from the garnet film is transmitted through an analyzer onto a p-i-n photodiode. The emission characteristics of GaAs:Al diodes are well suited for use with high Faraday rotation garnets for optical detection. The optical response and electrical characteristics of silicon p-i-n detectors are suitable for detecting the optical signal generated by a bubble propagating across the illuminating beam at high data rates.

The Faraday rotation of the conventional rare earth bubble garnets is inadequate for generating sense signals of sufficient amplitude for reliable data detection. However, the signal generated from a Bi-containing garnet is adequate for reliable operation.

1. Introduction

Sensing of cylindrical domains in a bubble memory device is at present a limitation to the development and exploitation of bubble technology for the realization of low-cost, high-performance digital stores. A

number of approaches for reliable sensing of bubble domains have been proposed and are being intensively investigated. The most promising approaches are (1) magnetoresistive sensing and (2) magneto-optical sensing.

In a magnetoresistive detector (MRD), the change in resistivity of a permalloy film induced by the presence of a bubble in the vicinity of the detector is used to generate a sense signal. In the magneto-optical detector (MOD), the magneto-optic properties of the storage film—uniaxial magnetic garnet—are used to generate a sense signal. The advantages and limitations of both approaches in terms of fabrication technology and systems organizations must be considered to allow realistic trade-offs in design.

Briefly, the MRD detector offers the advantages of a single technology for the photolithographic fabrication of the permalloy conductor pattern necessary for bubble generation, propagation, and sensing. An MRD requires the use of a bubble expander to obtain a sense signal that is adequate for reliable sensing. This is economically justified in system organizations that utilize a single detector for a large number of bits.

An MOD combines the technologies of solid-state light emitters and detectors to obtain an adequate sense signal from an unexpanded bubble. Thus, it offers the advantage of a system organization that has rapid read access.

2. Magneto-Optic Detector

A lenseless, all-solid-state magneto-optic detector, shown schematically in Fig. 1, consists of an edge-emitting light-emitting diode (LED), an aperture that defines the area illuminated by the LED, a polarizer, the bubble garnet film on an optically transparent substrate, an analyzer, and a silicon p-i-n photodiode.

Let I_0 be the intensity of light incident on the bubble film, I_+ the intensity of light incident on the detector when a bubble domain intercepts the optical beam, and I_- the background intensity. For the bubble film the quantities I_+ and I_- correspond to the two possible states of magnetization $+M$ and $-M$, respectively. The signal difference generated by the detector, corresponding to the two binary states, is¹

$$\Delta I = I_+ - I_- = \frac{CI_0}{2} e^{-at} \sin(2\theta t) \quad [1]$$

where C = losses due to reflection at various surfaces, α = absorption coefficient, θ = Faraday rotation, and t = thickness of the bubble film.

In Eq. [1] it is assumed that the polarizer is set at 45° to the analyzer to maximize the signal difference ΔI . Reliable sensing of unexpanded small-diameter domains is possible if a high-intensity I_0 could be realized and if the total Faraday angle θt is sufficiently large.

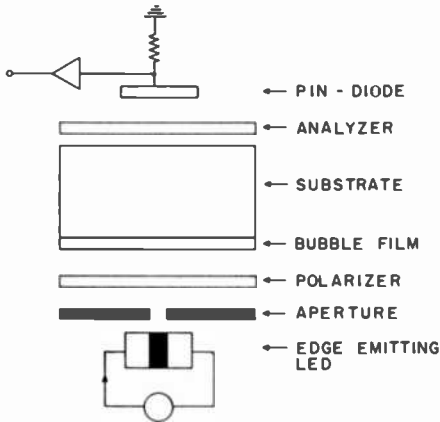


Fig. 1—Exploded view of lensless optical bubble detector.

2.1 Light-Emitting Diodes

A preliminary analysis indicated that a source brightness adequate for MOD of bubble domains in garnet films could be obtained from GaAs:Al noncoherent edge emitters.^{2,3} The emission characteristics of both single-heterojunction (SH), and double-heterojunction (DH) diodes were experimentally determined. Both types of diodes gave narrow-band emission, with peak emission occurring at 7600 Å for the SH diodes and 7500 Å for the DH diodes.

Fig. 2 shows schematically the geometry of an edge-emitting diode chip with dimensions of $L \times W \times D$. The effective width d of the emitting junction was estimated from the near-field radiation pattern as observed in a microscope. The angular spread of the emitted beam corresponding to W , the long side, and d , the short side, of the emitting area were determined by measuring the far-field radiation pattern in an optical scanner. The half-angles θ and ϕ correspond to the angles

at which the radiated intensity is one-half the peak intensity. Experimentally, it was found that 90% of the power radiated by the junction falls within a cone determined by 2θ and 2ϕ . The total power radiated by an emitting junction was determined by using a calibrated large-area p-i-n diode (UDT model, PIN 10) placed in close proximity to the emitting surface. For pulsed excitation of the LED, a 50-ohm load resistor was used with the PIN-10 to provide a short time constant of 23 nsec.

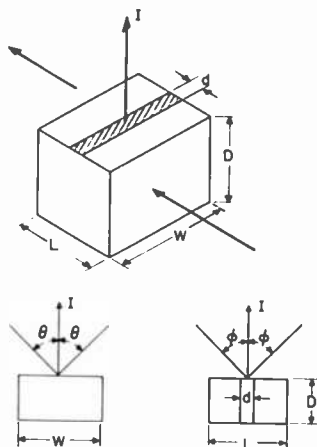


Fig. 2—Geometry of an edge-emitting LED.

Table 1 lists the measured characteristics for both SH and DH diodes of GaAs:Al. Fig. 3 shows the measured radiated power from a typical SH diode under the conditions of dc excitation and 1% duty cycle pulsed excitation.

2.2 Defining Aperture

The area illuminated by the LED may be defined by interposing an aperture between the LED and garnet film, as shown schematically in Fig. 1. The transmission efficiency of the aperture is a function of the geometrical relationships between the light source, the aperture, and the garnet film. For a circular aperture of area A illuminated by a rectangular source of dimension $L \times d$, assumed greater than the aperture diameter, the transmission efficiency for vanishingly small sep-

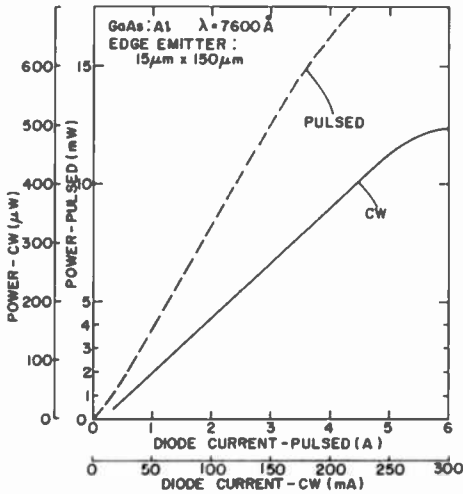


Fig. 3—LED optical power output.

arations between the source and aperture mask is given by $A/(Ld)$. Maximum transmission efficiency can be obtained by reducing the size of the light source to the dimensions of the aperture and by reducing the separation to zero. To achieve this desired set of conditions,

Table 1—Characteristics of GaAs:Al Edge-Emitting Diodes

Diode Type	SH	DH
Chip size $L \times W \times D$ (mils)	$6 \times 3 \times 10$	$2 \times 4 \times 6$
Junction width d (μm)	15	15
Junction area $L \times D$ (square mils)	60	12
Edge-emitting area $L \times d$ (square mils)	3.6	1.2
Radiated power with 1-A pulse excitation (μW)	2754	2227
Radiated power with 100-mA dc excitation (μW)	116	97
Half-angle θ (degrees)	30	52
Half-angle ϕ (degrees)	40	36
Power transmitted through $\frac{1}{4}$ -mil-thick mask with 1-mil-diameter aperture for 1-A pulse excitation (μW)	405	972
Mask efficiency (%)	14.7	43.6
Calculated mask efficiency (%)— $[A/(LD)]$	16.7	50

we successfully fabricated and tested aperture masks in 0.25-mil-thick aluminum foil. A 1-mil-diameter aperture was formed in the foil using an electric discharge milling machine. Fig. 4 is a photomicrograph of such an aperture. The face of the mask in contact with the LED is sprayed with an insulating plastic (Krylon) of neutral optical properties to prevent the diode from being short circuited.

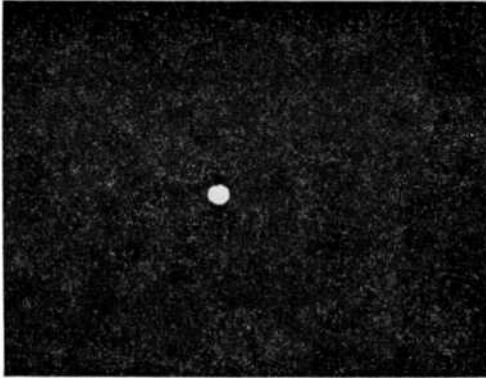


Fig. 4—Photomicrograph of 1-mil-diameter aperture in 0.25-mil-thick aluminum foil.

The foil masks were assembled with both SH and DH diodes, and the mask efficiencies experimentally determined. The data are given in Table 1. Excellent agreement with the computed efficiencies was obtained. For the DH diode with the smaller emitting junction area, the measured transmission efficiency is approximately 50%.

2.3 Characteristics of Polarizing Sheets

Fig. 5 shows the transmission efficiency of Polaroid HN-32 polarizing sheets as a function of wavelength as measured on a spectrometer. The transmission efficiency was measured for the two conditions of the polarizer-analyzer—uncrossed (parallel) and crossed. The HN-32 sheets are characterized by low losses and high extinction ratio up to 8000 Å.

To minimize the separation between the LED and garnet film it is necessary to utilize a thin polarizing sheet. Polaroid sheets with high transmission and extinction properties are not available in sheet form less than 10 mils thick. We were successful in polishing the

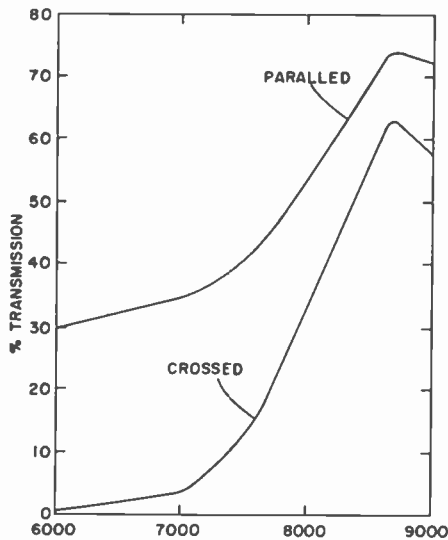


Fig. 5—Transmission properties of HN-32 polarizers.

plastic on both sides of an HN-32 Polaroid sheet with an original thickness of 10 mils to a final thickness of approximately 1 mil. The polishing caused no significant changes in the polarizing properties of the sheets.

2.4 Photodetector Circuits

The characteristics of the p-i-n diodes used in the evaluation of optical detection are listed in Table 2. The spectral sensitivity of a PIN-10 diode was separately measured, and the data are shown in Fig 6. The spectral sensitivity is essentially constant over the range from 6000 to 9500 Å.

Table 2—p-i-n Diode Photodetectors

UDT Device No.	Diameter of Active Area (mils)	Nominal Sensitivity at 8500Å ($\mu\text{A}/\mu\text{W}$)	Nominal Capacitance (pF)	
			$v=50$ V	$v=5$ V
PIN-5	88	0.3	5	30
PIN-10	500	0.3	130	360

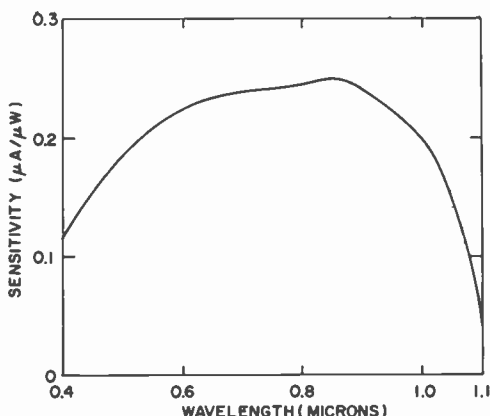


Fig. 6—Spectral sensitivity of PIN-10 silicon photodiode.

For dynamic detection experiments, the circuit shown in Fig. 7 was used. The circuit consists of a reverse-biased PIN-5 diode connected to a 5.1-kilohm load resistor. An integrated ac-coupled differential amplifier is used to increase the signal developed across the load resistor. The single-ended output of the amplifier is ac-coupled to an oscilloscope. The amplifier input impedance is 25 kilohms in shunt with a capacitance of 3 pF. For a PIN-5 diode, the capacitance is 18 pF, giving an input circuit time constant of 130 nsec and an equivalent 3-dB point of 1.2 MHz.

The amplifier gain is 34 dB (voltage ratio of 52) and is essentially constant over the pass band. With the input short circuited to ground, the rms noise voltage measured at the output is 1.6 mV. With approximately 20 μ W of light at a wavelength of 6328 Å (from an He-Ne laser) incident on the PIN-5 diode, the rms noise output is

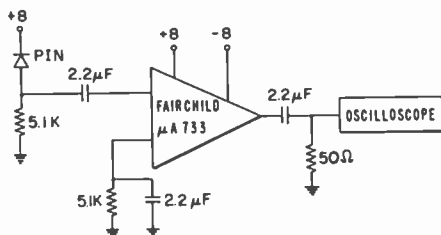


Fig. 7—Detector circuit.

1.7 mV. Thus, the main contribution to the noise is from the amplifier and not the p-i-n detector.

3. Optical Detection—Experimental

A number of critical experiments were undertaken to demonstrate optical detection of cylindrical domains.⁴ The results of these experiments are described below.

3.1 Laser Source

Orthoferrites—Using the experimental setup described in the Appendix, we showed that bubble domains with a diameter of 25 μm in $\text{Sm}_{.65}\text{Tb}_{.45}\text{FeO}_3$ orthoferrite platelets could be reliably detected using a laser as a light source. Briefly, the data obtained are as follows:

Source	Laser at 6328 Å
Polarizer & analyzer	HN-32 sheets, 10-mils thick
Bubble material	$\text{Sm}_{.65}\text{Tb}_{.45}\text{FeO}_3$ platelet, 0.8-mil thick
Detector	PIN-5 with 5-kilohm load
I_o	$\approx 40 \mu\text{W}$
ΔI	$\approx 1.8 \mu\text{W}$
Signal difference ΔV	2.7 mV
Signal-to-noise ratio SNR	40 dB

The signal difference ΔV corresponding to ΔI appears at the input of the amplifier. The SNR is referred to the amplifier output.

Garnets—Using the same setup as above we attempted to detect bubble domains propagating around a T-bar racetrack in a EuEr garnet film epitaxially grown on a GGG substrate. The setup was modified by the incorporation of a beam expander ahead of the microscope condenser to permit focusing of the laser to an 8- μm spot on the garnet film.

In an initial test we switched the magnetization of the garnet film with a normal magnetic field. This gave the maximum signal that could be obtained. The experimental data obtained are as follows:

Bubble material =	Epitaxial film of nominal composition
	$\text{Eu}_1\text{Er}_2\text{Ga}_{.7}\text{Fe}_{4.3}\text{O}_{12}$
Film thickness =	10 μm on surface containing racetrack and 6.2 μm on the opposite surface of the GGG

$I_o = 120 \mu\text{W}$ (147 mV developed by the p-i-n diode)

$\Delta I = 0.53 \mu\text{W}$ (0.66 mV developed by the p-i-n diode)

Light transmitted by garnet/light incident = $Ce^{-\alpha t} = 0.276$

Estimated Faraday rotation = $1.47^\circ/\text{mil}$

The estimated FR falls in the range of values measured for this composition.

The expected signal for detection of bubble domains propagating around the racetrack would be less than the 0.66 mV observed by switching the magnetization due to the following factors:

- (a) Disparity in size between 6- μm bubbles and 8- μm -diameter beam
- (b) Masking by propagation elements (estimated 0.38).
- (c) The Faraday rotation from one film only (10- μm thick) is effective in generating the signal (0.62).

The calculated peak signal to be expected under these condition is $\approx 90 \mu\text{V}$. When detection was actually attempted, no signal could be observed. The system random noise was $\approx 30 \mu\text{V}$ rms, so that the SNR was only 3. Additionally, residual stripe domains in the film on the reverse side of the GGG substrate produced dynamic effects that generated noise under the action of the rotating magnetic field. This noise interfered with the signal.

3.2 LED Sources

Using a setup similar to that shown schematically in Fig. 1, we were able to detect signal outputs from the photodetector when the magnetization in the bubble platelet was reversed by a magnetic field normal to the platelet. Experiments were conducted using samples of orthoferrites and garnets. The setup consisted of the following components.

LED	SH junction diode emitting at 7600 Å
Excitation	100 mA, dc, or 1-A pulse at a duty cycle of 0.1%
Total light output	116 μW dc or 2.75 mW pulsed
Aperture	1 mil diameter in 0.25-mil aluminum foil
Polarizer	1.5-mil-thick sheet of HN-32
Analyzer	10-mil-thick sheet of HN-32
Detector	PIN-10 with 5 kilohm load.

The sample characteristics are as follows:

- (a) Garnet composition: A (111) platelet of $\text{Bi}_{3-2x}\text{Ca}_{2x}\text{V}_x\text{Fe}_{5-x}\text{O}_{12}$ with $x \approx 1.14$ prepared from a flux crystal.⁵

Platelet thickness: 1.7 mils
 Absorption $e^{-\alpha t}$: 0.53
 Faraday rotation θ : $10.8^\circ/\text{mil}$

- (b) Orthoferrite composition: $\text{Sm}_{.55}\text{Tb}_{.45}\text{FeO}_3$

Platelet thickness: 1.08 mils
 Absorption $e^{-\alpha t}$: 0.25
 Faraday rotation θ : $6.5^\circ/\text{mil}$
 Birefringence ρ : $266^\circ/\text{mil}$

The experimental data obtained by switching the magnetization in the samples (340 Oe for the BCV garnet and 100 Oe for the SmTb orthoferrite) are given in Table 3.

Table 3—Experimental Data for MOD

LED Drive	BCV Garnet		SmTb Orthoferrite	
	100 mA dc	1 A pulsed	100 ma DC	1 A pulsed
I_o (μW)	8.9	200	8.4	200
ΔI (μW)	0.9	18	0.04	1

The results show that the pulsed signal output increases by a factor of approximately 24 for a factor-of-10 increase in LED drive current. This is accounted for by a measured increase in LED efficiency in the pulsed mode by a factor of 2.4.

In calculations using the garnet parameters given above and the expression

$$\Delta I = \frac{I_o}{2} e^{-\alpha t} \sin(2\theta t) \quad [2]$$

we obtain $\Delta I = 32 \mu\text{W}$. Calculated reflective losses at the garnet surface reduce ΔI by approximately 30% to yield $\Delta I = 22 \mu\text{W}$, in close agreement to the measured value of $18 \mu\text{W}$.

Fig. 8 shows the oscilloscope trace obtained with the BCV garnet sample under conditions differing slightly from the above data. The

p-i-n detector was connected to the oscilloscope input with several feet of coaxial cable resulting in the relatively long rise time seen in the traces. Since the polarizer analyzer are set at 45° , a pedestal of 27 mV corresponding to "1" binary state is generated. The difference signal of 18 mV corresponds to the switching of the magnetization in the garnet.

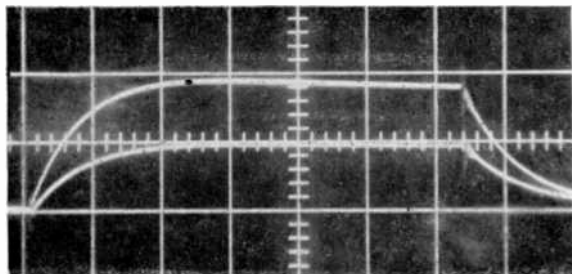


Fig. 8—Oscilloscope traces showing MOD output for binary states of BCV garnet platelet.

For the orthoferrite sample, similar calculations show reasonable agreement with the experimental data. Because of the high birefringence, the exact determination of the sample thickness is important.

4. Optical Detection—Projection

The light power required for the detection of bubble domains with a diameter of $8 \mu\text{m}$ may be estimated from the results presented above.

For the p-i-n diode the sensitivity is $\approx 0.25 \mu\text{A}/\mu\text{W}$, and the load resistor is 5 kilohms. Thus, a differential signal of 1 mV results from a ΔI of $0.8 \mu\text{W}$.

For a bubble film with magneto-optic properties of BCV and a thickness t of 0.5 mil ($12.5 \mu\text{m}$), a bubble diameter of $\frac{1}{3}$ mil ($8 \mu\text{m}$), absorption $e^{-\alpha t} = 0.83$, and reflection losses of 30%, the desired 1-mV sense signal may be obtained for

$$I_o = \frac{2\Delta I}{C e^{-\alpha t} \sin(2\theta t)} = 15.3 \mu\text{W},$$

where $C = 0.7$ accounts for reflection losses.

For a polarizer transmission efficiency of 46% (1 sheet of HN-32),

the power transmitted by the defining aperture should be $\approx 33.3 \mu\text{W}$. For an emitting junction area of 1.2 square mils and an aperture area of 0.09 square mil ($\frac{1}{3}$ -mil diameter aperture), the maximum aperture transmission efficiency is 7.5%. Thus, the power needed from the LED is $\approx 450 \mu\text{W}$.

Referring to Table 1, we note that the DH junction diode is potentially capable of generating the required light power if it is excited with approximately 200 mA. A reduction in the dimension D from 6 mils to 2 mils is not expected to lead to a reduction in light output but will reduce the required excitation to approximately 70 mA.

Detection of small-diameter bubbles may be accomplished with a p-i-n diode of small active area. Assuming that the optical beam is contained in a cone of half angle of 45° and that a GGG substrate 20 mils thick is used, then a diode with an active area having a diameter of 20 mils is large enough to intercept the optical beam. The decreased divergence of the beam is a result of the high index of refraction of GGG.

For a diode of 20 mils diameter, the time constant of the input circuit is estimated to be 50 nsec, with a corresponding 3-dB-down frequency of 3.2 MHz. A wider bandwidth may be realized by reducing the load resistor from the selected value of 5 kilohms.

The SNR for a signal of 1 mV and a bandwidth of 3.2 MHz is expected to be in excess of 26 dB. Considerable improvement in SNR may be realized by using a low-noise amplifier.

5. Conclusions

Optical detection of bubble domains requires a garnet film that combines bubble properties with superior magneto-optic properties. The Faraday rotation of conventional bubble garnet compositions is inadequate for optical sensing. The BCV garnet has desirable magneto-optic properties⁴ and has been shown to have uniaxial properties in slices cut from flux-grown crystals,⁵ but has not been grown as an epitaxial film on a non-magnetic substrate.

Recent data indicate that the Faraday rotation of YIG:Bi is high^{6,7} and that epitaxial films can be grown⁷ on $\text{Gd}_3\text{Ga}_5\text{O}_{12}$ substrates. Thus we can expect that bubble films of superior magneto-optic properties can be realized.

Acknowledgments

The authors wish to express their appreciation to Mrs. A. Akselrad for many helpful discussions, and for the samples and data on BCV

garnets. H. Kressel aided this work by providing the LED's and by his invaluable consultations. R. Clover was instrumental in establishing the experimental setup for dynamic bubble detection and for obtaining some of the data on the orthoferrites.

The research reported in this paper is jointly sponsored by the U. S. Air Force, Avionics Lab, Wright-Patterson Air Force Base, Dayton, Ohio, under contract #F33615-72-C-1528 and RCA Laboratories, Princeton, New Jersey.

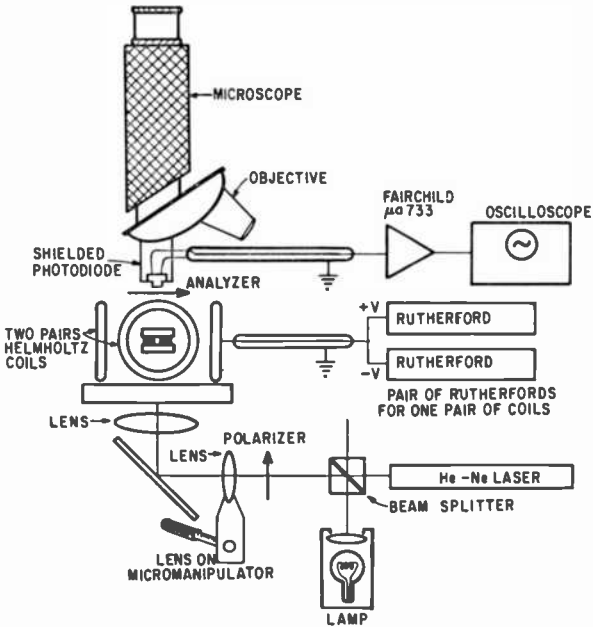


Fig. 9—Optical detection test apparatus.

Appendix—Experimental Setup for Dynamic Bubble Detection

The test system used is shown schematically in Fig. 9. A bubble platelet with a T-bar pattern on a glass overlay is located within two pairs of Helmholtz coils that were mounted on a microscope stage. The bubble circuit could be observed visually through the microscope when desired. For sensing, a silicon PIN-5 photodiode replaced the viewing objective by rotating the microscope turret.

Light from an He-Ne laser was focused to a 2-mil-diameter spot as shown in Fig. 10(a). This spot could be located at any point on the permalloy circuit.

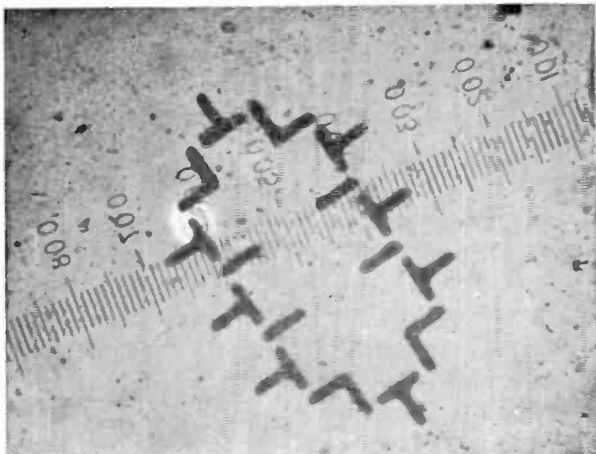


Fig. 10(a)—Bubble in $\text{Sm}_{0.65}\text{Tb}_{0.35}\text{FeO}_3$ illuminated by focused He-Ne laser beam (diameter approximately 2 mils).

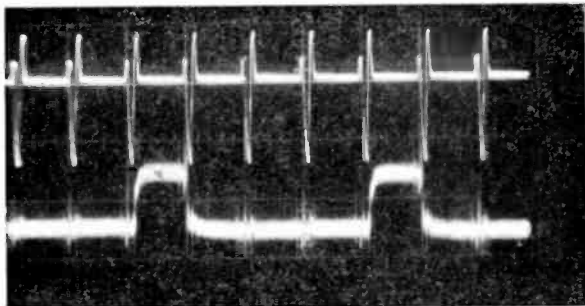


Fig. 10(b)—(Top) Drive pulses for generating rotating in-plane magnetic field ($15 \mu\text{sec}/\text{cycle}$) and (bottom) optical sense signal from bubble detected with a Si PIN-5 photodiode.

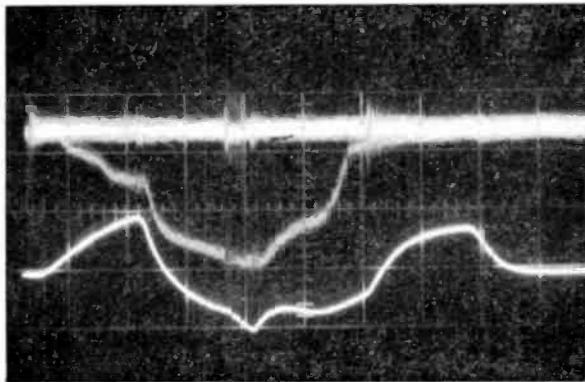


Fig. 10(c)—(Top) Optical sense signal for bubble detected "on the fly" and (bottom) drive current pulses for generating rotating in-plane field ($40 \mu\text{sec}/\text{cycle}$).

The coils were driven by a set of four Rutherford pulse generators to provide a rotating drive field in the plane of the bubble platelet. The subsequent magnetic switching of the T-bar elements resulted in bubbles circulating on the track. As a bubble passed by the focused light beam, a sense signal was generated, amplified, and observed on an oscilloscope.

The drive pulses were delivered at a fairly low duty cycle. Each series of pulses resulted in a 360° rotation of the drive field and the translation of the bubble by one period of the T-bar structure. In Fig. 10(b), a sense signal is shown that appears when the bubble is at rest between drive cycles. In Fig. 10(c), the position of the laser beam was shifted so that the sense signal was generated when the bubble was "on the fly."

In the case of orthoferrites, the signal difference is given by

$$\Delta I = \frac{CI_0}{2} \sin \chi \sin \phi$$

where $\chi = \tan^{-1} 2\theta/\rho$ and $\phi = \sqrt{\rho^2 + (2\theta)^2}t$. θ is the Faraday rotation and ρ the birefringence.

References:

- ¹ F. A. Jenkins and H. E. White, *Fundamentals of Optics*, McGraw-Hill Book Co., New York, N. Y. (1957).
- ² H. Kressel, F. Z. Hawrylo, and N. Almeleh, "Properties of Efficient Silicon-compensated Al_xGa_{1-x}As Electroluminescent Diode," *J. Appl. Phys.* Vol. 40, p. 2248 (1969).
- ³ D. J. Nuese, A. G. Sigal, and I. Kudman, "High Brightness Electroluminescent Diodes," Annual Report, Contract N00014-71-C-0198, NR 215-172, Jan. 1972.
- ⁴ R. Shahbender and J. Druguet, "Magneto-optic Detection of Bubble Domains," Paper presented at Intermag 1973 Conf., paper #19.3.
- ⁵ A. L. Akseilrad, "Magneto-optical Effects in Certain Calcium Vanadium Iron Garnets," *Proc. AIP Conf. on Magnetism and Magnetic Materials*, Chicago, Ill., Nov. 1971, No. 5, p. 249.
- ⁶ A. L. Akseilrad and H. Callen, "Growth-induced Noncubic Anisotropy Arising from the Tetrahedral Sites in Garnet," *Appl. Phys. Letters*, Vol. 19, p. 464 (1971).
- ⁷ R. Shahbender, A. L. Akseilrad, J. L. Druguet, and L. S. Onyshkevych, "Magneto-optic Interactions," Technical Report AFAL-TR-73-240.
- ⁸ S. Wittkock, J. M. Robertson, T. J. A. Popma, and P. F. Bongers, "Farady Rotation and Optical Absorption of Epitaxial Films of Y_{1-x}Bi_xFe₂O₇," *Proc. AIP Conf. on Magnetism and Magnetic Materials*, Chicago, Ill., Nov. 1972, No. 10, part 2, p. 1418.

Vented-Bore He-Cd Lasers

Karl G. Hernqvist

RCA Laboratories, Princeton, N. J. 08540

Abstract—A new type of He-Cd laser tube construction is described that allows accurate control of the cadmium vapor density in the discharge bore. A vented-bore tube is placed inside a cadmium-vapor reservoir. The construction and performance of such lasers is described. A two-fold increase of output power and a five-fold reduction of radiation noise is achieved as compared to the performance of conventional straight-bore lasers.

Introduction

Maximum output of an He-Cd laser occurs at a specific cadmium vapor density in the discharge bore. Common practice in these laser tubes^{1,2} is to supply cadmium vapor at a predetermined rate at the anode end of the bore and to let cataphoretic transport of cadmium by the discharge determine the vapor density along the full length of the bore. It has been found, however, that the cataphoretic effect does not uniquely define the vapor density in long bores, and considerable deviations from optimum density may occur both in time and position.³ As a consequence, the power output falls short of the potential

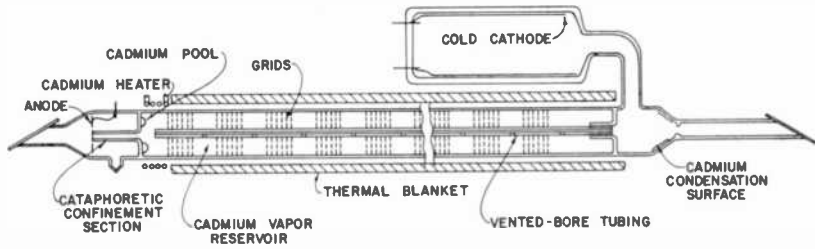


Fig. 1—Schematic drawing showing vented-bore He-Cd laser.

capability of the laser medium, and radiation noise may be excessive. To solve this problem, it is necessary to reinforce the optimum cadmium density at regular intervals along the length of the bore.^{3,4} We have found that the simplest and most accurate way of doing this is to place the discharge bore inside a larger cadmium vapor reservoir and to let the two chambers communicate via vent holes cut in the bore at appropriate intervals. This paper describes the construction and performance of such vented-bore lasers.

Generally these lasers achieve a two-fold increase of output power and a five-fold reduction of radiation noise compared to the performance of conventional straight-bore lasers. In addition, the gain in these lasers is high enough to allow use of natural cadmium, even for short tubes, thus simplifying construction and operation.

Construction of Vented-Bore He-Cd Lasers

Figs. 1 and 2 show the construction of a vented-bore He-Cd laser. The principal parts of the discharge conduction path include the cold cathode, the vented bore, the cataphoretic confinement section, and

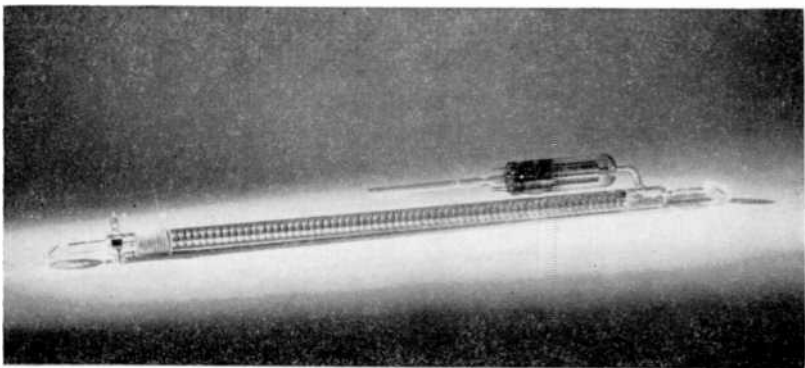


Fig. 2—Photograph showing vented-bore He-Cd laser.

the anode. The bore is coaxially positioned in the large-diameter gas reservoir, and the bore and the reservoir communicate via the evenly spaced vent holes. Metal grids between the vent holes prevent electrical breakdown in the reservoir. The cadmium pool is also positioned in the reservoir, and an external heater controls its temperature. The reservoir region is provided with external thermal isolation to assure that the cadmium pool region is the coolest part of the reservoir chamber during operation.

After the laser has been started, the heat from the discharge is sufficient to raise the reservoir temperature above the condensation temperature of cadmium at the pool (250–275°C). The cadmium vapor then uniformly fills the reservoir and the communication via the vent holes assures that the deviation of vapor density in the bore is kept to a minimum. Cadmium is transported by cataphoresis out to the cathode region, and a sufficient supply of cadmium must be provided for the life of the tube (of the order of 1 gram/1000 hours).¹ In principle, the cadmium pool could be located anywhere within the vapor reservoir. However, since there is a net cataphoretic transport of cadmium through the bore towards the cathode, a density gradient would have to be established within the reservoir if the pool were located anywhere except at the anode end of the reservoir.⁵ This density gradient would cause a corresponding deviation from the optimum density in the bore. Furthermore, it is essential that the pool communicates rapidly with any part of the reservoir. Since the transport rate (per unit area) of cadmium in the discharge bore is about 100 times higher than in the reservoir,⁵ a ratio of reservoir-to-bore diameter of about 10 is desirable to assure a minimum of density deviations.

The optimum separation of the vent holes is more difficult to estimate. Studies on recirculation-type lasers⁵ indicated that stable discharge striations existed for a length of about 2 cm in a 1.2-mm-bore tube. A reservoir separation of 6–8 cm in a 2-mm-bore tube was chosen in a segmented bore design.⁴ We have found that a value of 20 for the ratio of vent-hole separation to bore diameter yields good laser performance, yet does not complicate tube construction.

An essential part of the vented-bore design is the electrical isolation between the vent holes in the reservoir. A set of three pairs of metal grids (each pair electrically connected) has been found to be sufficient for this purpose.

Several vented-bore tubes of different sizes have been tested. The results are summarized in Table 1. They all use natural cadmium and one-way transport. The power outputs (for operation in the TEM₀₀

Table 1—Performance of Vented-Bore He-Cd Lasers

Bore Dia. D cm	Bore Length L cm	I mA	V Volts	P_{out} mW (442 nm)	P_{out} mW (325 nm)	I/D mA/cm	P_{out}/LD mW/cm ² (442 nm)	VD/L Volts
0.1	15	40	1200	8		400	5.3	8
0.12	30	50	1900	18	4.5	417	5	7.6
0.15	60	60	2500	50	12	400	5.5	6.2
0.24	180	100	6000	200	25	417	4.6	8

mode and corresponding to 2% RMS radiation noise) are 2.5 times higher than previously reported for similar discharge conditions.^{4,6} Table 1 also gives values for P_{out}/LD , I/D , and VD/L , where L and D are the length and diameter of the bore, respectively. These indicate that the scaling laws are similar to those of He-Ne lasers.⁷ A comparison of these values is given in Table 2. The vented-bore construction has also been used in connection with the recirculation geometry⁵ and shown to yield similar improvements in performance.

Several authors^{8,9} have reported a double-saturation effect in the output versus discharge current relationships for conventional straight-bore He-Cd lasers. This has been attributed to a change-over in the predominant laser excitation mechanism. In the vented-bore tubes (listed in Table 1), no such effects have been observed. Fig. 3 is a typical power-output-versus-current diagram showing the well-defined single saturation behavior. The possibility that the double-saturation effect is simply a result of discharge or cadmium distribution irregularities can therefore not be ruled out.

Radiation Noise Characteristics

Just as for the He-Ne laser, the radiation noise of an He-Cd laser depends on the discharge conditions.^{4,5} In general, both output and noise level increase with He pressure for an He-Cd laser. The dependence of the Cd vapor pressure and of the discharge current is more complex. Fig. 4 shows the radiation noise as a function of

Table 2—Comparison of Scaling Laws for He-Cd and He-Ne Lasers

	P_{out}/LD mW/cm ²	I/D mA/cm	VD/L Volts
He-Cd 442 nm	5	400	6-8
He-Ne 633 nm	1-1.5	100	9

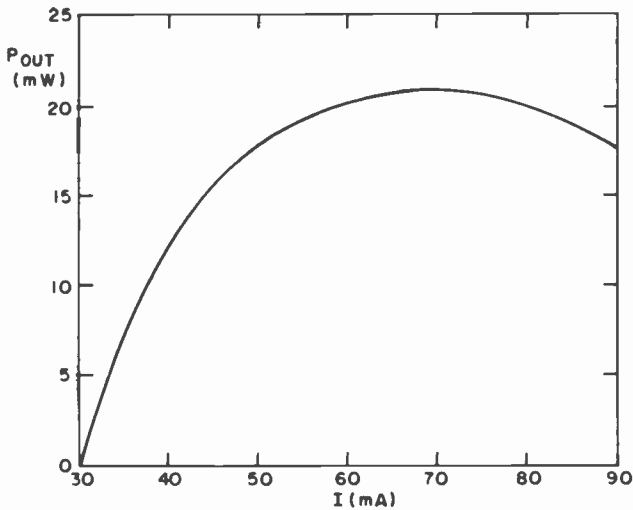


Fig. 3—Typical power output versus discharge current characteristic for vented bore He-Cd laser.

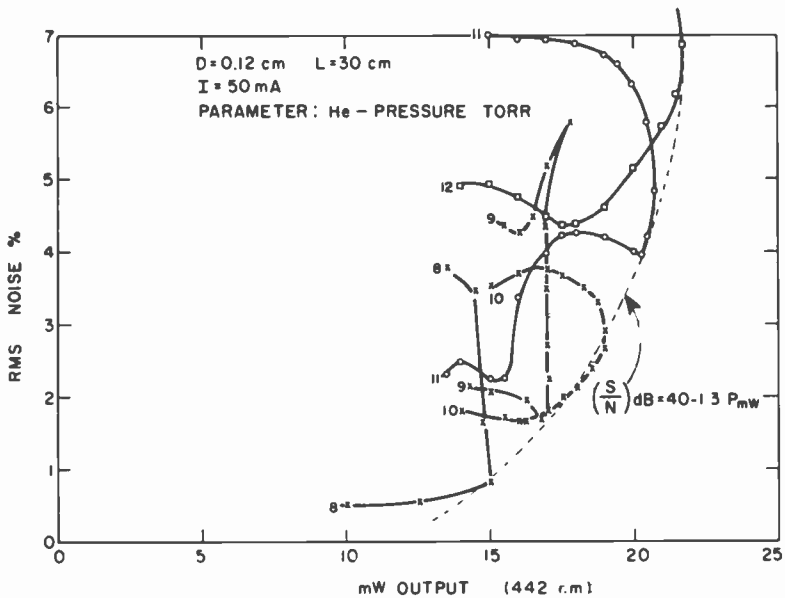


Fig. 4—Radiation noise versus output as Cd vapor pressure is varied.

power output for different helium pressures. For each of the curves plotted in Fig. 4, the cadmium vapor pressure is slowly increased and the output and noise level are recorded. As the curves show, the relationships are quite complicated. There is, however, a unique relationship for optimum Cd vapor pressure and for current near saturation between noise and power output (in mW) as the helium pressure is varied. For instance, for the 30-cm-long tube the signal-to-noise ratio in the range 10 to 20 dB is given by $(S/N)_{dB} = 40 - 1.3 P_{mW}$ where the corresponding helium pressure is $p(\text{Torr}) = 0.63 P_{mW} - 1.7$. Thus for each tube size, the desired noise level may be chosen by filling at the corresponding helium pressure.

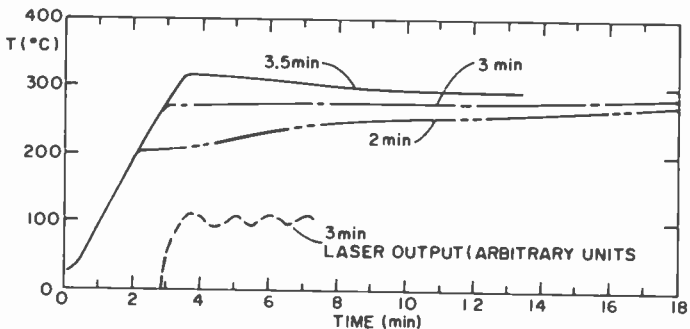


Fig. 5—Wall temperature versus time for He-Cd laser. Parameter is the "on" time for a 300-watt auxiliary heater. Also shown is the laser output versus time for the 3-minute heating case. Zero time represents the simultaneous laser ignition and heater turn-on.

Quick Warm-Up

The main disadvantage of the He-Cd laser as compared to the He-Ne laser is the longer warm-up time. Lasing does not commence as soon as the discharge is started but only after both the tube envelope and the cadmium pool have reached the appropriate temperatures ($\sim 250^\circ\text{C}$). For steady-state operation, the heat from the discharge suffices to keep the tube hot. However, to speed up the warm-up process, additional heat is required. For instance, the 30-cm active length tube listed in Table 1 requires about 12 minutes to reach operating temperature when relying solely on the discharge heat (about 100 watts). To shorten the warm-up time to the desired value, the 72 kilojoules required can be supplied partly by an external heater. For instance, a 300-watt heating tape wrapped around the tube and connected via a simple timing circuit shortens the warm-up

period to 3 minutes. Fig. 5 shows wall temperature as a function of time for different heating times (starting at ignition). Fig. 5 also shows the laser output corresponding to the optimum 3 minute heating time.

Conclusions

Vented-bore construction is a simple and accurate way of controlling the cadmium vapor density in He-Cd lasers. It makes possible the realization of the full capability of the laser medium.

Acknowledgment

The author is grateful for the able support of R. Carbonetta, H.E. McCandless, and D.C. Pultorak.

References:

- ¹ J. R. Fendley, I. Gorog, K. G. Hernqvist and C. Sun, "Characteristics of a Sealed-Off He³-Cd¹¹⁴ Laser," *RCA Review*, Vol. 30, p. 422 (1969).
- ² J. P. Goldsborough, "Stable, Long-Life CW Excitation of He-Cd Lasers by DC Cathodoluminescence," *Appl. Phys. Lett.*, Vol. 15, p. 159 (1969).
- ³ K. G. Hernqvist, "Stabilization of He-Cd Laser," *Appl. Phys. Lett.*, Vol. 16, p. 464 (1970).
- ⁴ W. T. Silfvast and L. H. Szeto, "Simplified Low-Noise He-Cd Laser with Segmented Bore," *Appl. Phys. Lett.*, Vol. 19, p. 445 (1971).
- ⁵ K. G. Hernqvist, *IEEE J. Quant. Elec.*, Vol. QE-8, p. 740 (1972).
- ⁶ D. T. Hodges, "He-Cd Laser Parameters," *Appl. Phys. Lett.*, Vol. 17, p. 11 (1970).
- ⁷ R. L. Field, "Operating Parameters of DC-Excited He-Ne Gas Lasers," *Rev. Sci. Instr.*, Vol. 38, p. 1720 (1967).
- ⁸ L. Csillag, M. Janossy, K. Kantor, K. Rozsa, and T. Salamon, "Investigation on a Continuous Wave 4416 Å Cadmium Ion Laser," *Brit. J. Appl. Phys. (J. Phys. D)*, Vol. 3, p. 64 (1970).
- ⁹ M. Janossy, V. V. Itagi, and L. Csillag, *Acta Phys. Sci. Hungaricae*, Vol. 32, p. 149 (1972).

Scanning-Beam Performance from a Negative-Electron-Affinity Activated Silicon Cold Cathode*

A. D. Cope and E. Luedicke

RCA Laboratories, Princeton, N. J.

J. P. Carroll

RCA Electronic Components, Princeton, N. J.

Abstract—The development and evaluation of a negative electron affinity (NEA) activated silicon cold cathode for a vidicon camera tube is reported. The emitter consists of a p region 25 or 50 μm in diameter grown on an n wafer to form a diode that is operated with forward bias. With the p surface processed for NEA, that part of the injected current reaching the NEA surface is emitted into vacuum. The means for adapting suitably structured silicon wafers into a gun structure is discussed. The complexities of NEA activation of silicon in gun structures and the relationship between activation procedures and extended cold-cathode operating life are reported. With current density in excess of 10^{-2} amp/cm², a maximum target of ≈ 70 nA/cm² was obtained from scanning a silicon mosaic target (total beam current >500 nA). Measurements indicate an energy spread of ≈ 0.3 eV from the NEA cathode which is degraded to 1.5 eV as the result of shortcomings in the initial gun design. Low-target-voltage operation, a uniform target cutoff, and resolution limited by the S/N of the low level signal are characteristics of these developmental tubes.

Emission density $>10\times$ higher than this has been obtained from NEA silicon cold cathodes in other configurations and should be attainable in guns with improved contacts, which would allow processing optimization and improved gun design. Avenues for further development of NEA activation of silicon cold cathodes that will improve initial performance and extend operating life beyond 50 hours have been identified.

* The research reported in this paper was sponsored in part by USAECOM, Night Vision Laboratory, Fort Belvoir, Va., under Contract No. DAAK02-72-C-0259.

Introduction

This paper describes an experimental study of techniques for preparing a silicon cold-cathode emitter with a geometry suitable for incorporation into the gun structure of a television camera tube. The silicon cold cathode is a small area p-n diode in which the p surface has been processed to a state of negative electron affinity (NEA). When such a diode is operated in forward bias, the portion of the injected electrons that traverse the p region are emitted from the NEA surface as free electrons. The energy-band diagram of such a structure is shown in Fig. 1.

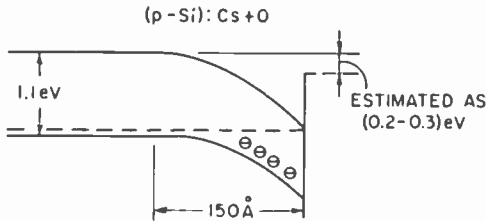


Fig. 1—Band diagram of silicon diode with negative electron (NEA) activation.

The preparation of suitable diode geometries on n-type wafers and the development of techniques for mounting and activating small-area diodes to a high emission current density was a first objective. Incorporating such a diode structure into a vidicon tube design and determining the capability for the cold-cathode emission current to be formed into a beam suitable for use in a camera tube was a second objective.

Of particular concern was the emitted current density and peak emission current for stable operation both initially and during operational life. The emitted electron energy distribution and spot size at the target were studied and related to the operating characteristics of a camera tube with a silicon mosaic target.

Small-Area NEA Silicon Cold Cathode

Prior work by E. S. Kohn¹ has shown that, at ambient temperature, high density electron emission is obtained from a forward-biased silicon p-n junction after the p-surface has been activated to a state of negative electron affinity. A current of several hundred nanoamperes from a small-area silicon junction, which represents a cur-

rent density in excess of 1 amp/cm², had been obtained over several hours of continuous operation in a simple cathode-anode tube configuration. However, no beam-forming electron optics using this type of emitter had been built and evaluated.

The potential capability of a silicon NEA cathode to provide, from a small emitting area, a high current density of electrons with a narrow spread in their initial energies is attractive for use in camera tubes. These tubes almost universally depend upon cathode-potential stabilization of the scanned side of the storage target as the means for video readout.

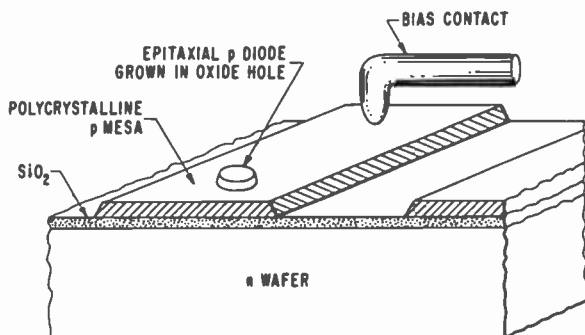


Fig. 2—Silicon cold-cathode mesa structure.

The samples studied were all prepared from n type (100) silicon wafers approximately 5 mils thick and doped with antimony at $2 \times 10^{18}/\text{cm}^3$. A masking oxide is grown to a thickness of $1\mu\text{m}$ and then, using an appropriate mask with photolithographic and etching technology, a pattern of diode openings is cut through the SiO₂. Next, a p layer of silicon is grown using silane vapor reaction technology. Approximately $2\text{-}2.5\mu\text{m}$ of vapor-grown polycrystalline Si, doped p type with boron at $8 \times 10^{19}/\text{cm}^3$, is deposited in the mesa region. The growth of epitaxial material in the diode openings proceeds at a more rapid rate than the polycrystalline growth, so that, in the completed sample, the diode surface is slightly higher than the surrounding mesa. Next, a second oxide is grown, and, using photolithography with a second mask followed by further etching, the final pattern is produced. As shown in Fig. 2, this consists of a polycrystalline-silicon-covered SiO₂ mesa surrounding each diode.

Fig. 3, which is a photomicrograph of a shallow-angle cross-section through one diode, has been stained to darken the p region. The

relative growth rate of the epitaxial and polycrystalline material proved to be a sensitive indicator of the diode quality. When the epitaxial surface was depressed relative to the polycrystalline surface, as sometimes occurred, the measured diode rectification characteristics were poor. Frequently, evidence of polycrystallinity in the diode was also observed. This most probably can be related to incomplete removal of oxide or etchants from the diode hole, although occasional improper temperature or gas-flow conditions in the silane reactor produced poor quality epitaxial growth.

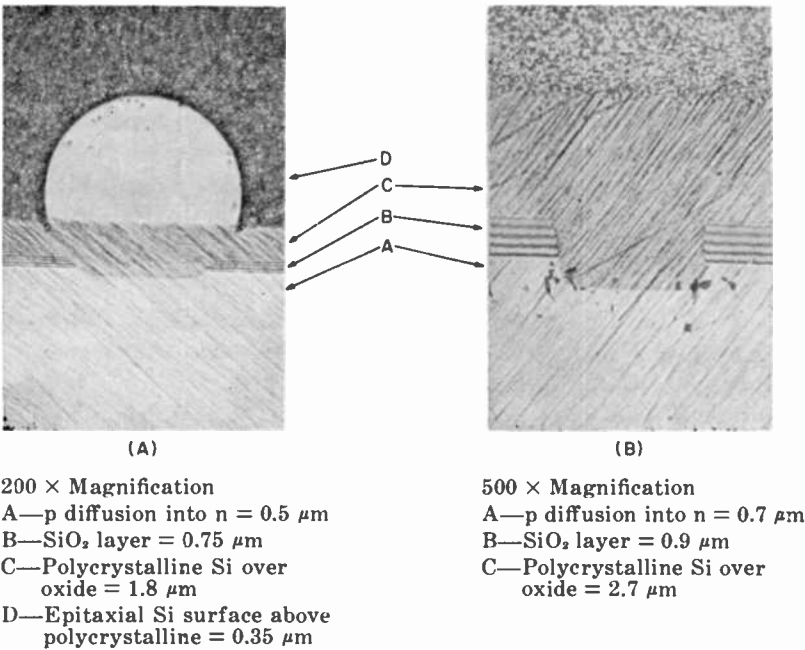


Fig. 3—Photomicrographs of a shallow-angle cross-section of a silicon cold-cathode diode.

Returning to consideration of Fig. 3, the n Si, the dark stained p Si, and the SiO₂ regions are clearly distinguished. Since these samples had been heated several times to temperatures between 800 and 1200°C to produce NEA activation, the more highly doped p material has diffused into the n region. The tolerable amount of diffusion is of concern in establishing the parameters both for the

silicon cold-cathode doping levels and the subsequent activation procedures, since diffusion in effect moves the junction away from the emitting surface. Kohn has shown that the number of injected electrons that reach the emitting surface per second, η , for bias voltage $V \gg kt$ and with an electron diffusion length in the p region $> s$, where s is the thickness of the p region, is

$$\eta = \frac{D_e n_p e^{V/kt}}{s}$$

Here, D_e is the electron diffusion constant and n_p the density of minority carriers in p region. Junction diffusion of the order of $1 \mu\text{m}$ does not appear to reduce the emission density from the NEA surface. Diffusions markedly greater than $1 \mu\text{m}$ were encountered only when there had been excessive heating of the cold-cathode wafer in the attempt to obtain NEA activation from a contaminated sample.

One possible means for slowing the rate of junction diffusion is to deposit a more highly doped n^+ surface on the wafer before it is structured. No significant differences in emission density were observed from such samples. At some later stage in cold-cathode development, a more critical evaluation of the diffusion parameters might be in order to optimize the emission efficiency.

By providing individual contact to each of several diodes, it has been possible to measure the performance of multiple diodes on a single wafer. The first test bottles activated made use of wafers that had been prepared from a mask containing two rows of repeating pattern of 5-, 2-, 1-, and 0.5-mil-diameter diodes. In the later work with gun structures, a pattern composed of a four diode cluster was employed. In order that the emission be limited to the one diode of known size and location, it is important that there be no spurious breaks in the pattern-defining oxide of the associated mesa. Spurious emission from both pinholes and over-etched mesa edges was encountered during the process development.

After the initial activation of test bottles had established that one- and two-mil-diameter diodes could be activated with reasonable consistency, the diode-cluster mask was designed to provide two square diodes of one-mil and two of two-mil size with minimum separation (Fig. 4). Since any one of the four diodes is close enough to the tube axis to be usable in a vidicon structure, redundancy could be provided in each activated cathode assembly.

Negative Electron Affinity Activation

Prior work by R. U. Martinelli² on secondary electron emission and photoemission from p type silicon with a NEA surface has established the basic activation procedures. This work has been augmented by the analytical studies of B. Goldstein³ and J. Levine⁴ using Auger

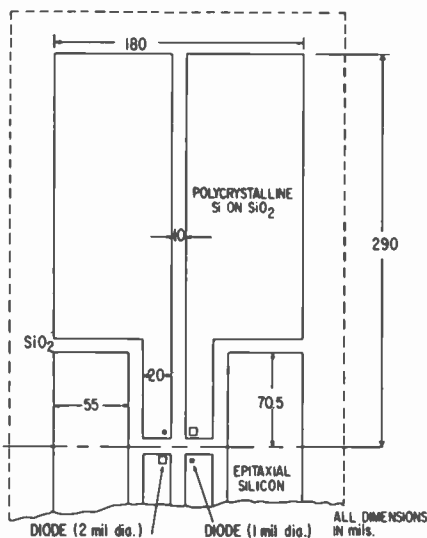


Fig. 4—Diode cluster pattern for silicon cold cathode.

spectroscopy and LEED (low energy electron diffraction) measurements to determine the details of the NEA silicon surface. The model evolved is as follows. On the surface of (100) p silicon, a complex monolayer is formed consisting of cesium and oxygen located at prescribed sites associated with the reconstructed silicon surface lattice. In order for this monolayer to form, the silicon surface must be free of oxide or foreign material such as metal or carbon atoms. The cesium is deposited first, defining the available sites for the oxygen atoms to be deposited later.

Obtaining a clean silicon surface is a key part of the NEA activation procedure. This starts with a rigorous chemical cleaning of the patterned wafer after it has been cleaved to the desired shape for mounting in a tube structure. The cleaning procedure is designed to remove any organic or metallic residues and to strip away the thin layer of oxide which has formed on the exposed surfaces.

After the chemically cleaned sample has been clamped into the support structure and the p contacts have been placed, it is sealed into a glass bottle that is then sealed to a vacuum pumping system. The entire bulb assembly is vacuum baked for several hours at 350-400°C, so as to outgas the mount and bulb, in particular ridding the tube of absorbed water molecules.

Since both the chemical cleaning and the handling of the wafer during the mounting and sealing of the glass-tube envelope have a large effect upon the condition of the wafer surface, considerable attention was devoted to these procedures. Although passivation of the silicon surface might well have relieved assembly problems, an investigation of the technique for silicon iodide passivation described by Lieberman and Klein⁵ gave no encouraging evidence of easier preparation for activation.

Sealing of the glass bulb proved to be the greatest source of a heavy SiO₂ growth on the silicon surfaces, making it virtually impossible to activate the sample. Eventually, this problem was avoided by using a metal gasket-flange seal, made at room temperature, to close the bottle. No particular problem associated with tipoff of the glass tubulation was identified, although a metal pinch-off tubulation might be a more desirable alternative.

Ideally, the initial thermal processing is required to remove only the thin SiO₂ layer that has formed spontaneously with exposure to a dry atmosphere following the chemical cleaning. When the problems associated with forming excess oxide on the surface of the cold cathode wafer had been overcome, the yield of successful NEA activations came to depend upon the ability to heat the crystal to a uniform temperature close to its melting point without either distorting the wafer or losing contact to the diodes.

The first samples activated as part of this program, following the practice of prior photosensitivity studies, were brought to a peak of NEA activity before removal from the pumping system. It was observed quite early that the photoemission peak from epitaxial p areas adjacent to the diodes did not coincide with the peak emission from a forward-biased diode. No more systematic relationship was evident here than had been observed with the variability of peak photosensitivity in different regions of an extended-area photoemissive sample.

The room temperature emission from samples brought to peak NEA activity immediately before being removed from the vacuum systems showed a characteristic drop in emission during operational life. In studying the relationship between NEA activation and the

operating life of the cold-cathode emitter, it was observed that loss of oxygen from the NEA surface is the factor most often responsible for the drop in emission. By cyclically operating the cathode on the exhaust system and, after an emission slump had occurred, replacing the lost oxygen, two changes were observed. After a number of repeat oxygen treatment cycles both the rate of slump and the amount of slump decreased. Several samples that had stabilized at an emission level about $\frac{1}{3}$ the activation peak were operated after removal from the exhaust system. These samples gave noticeably longer life without loss of emission than earlier unstabilized samples. Such results suggest a promising area for further experimental investigation that could provide significant improvement in NEA silicon cold cathode performance.

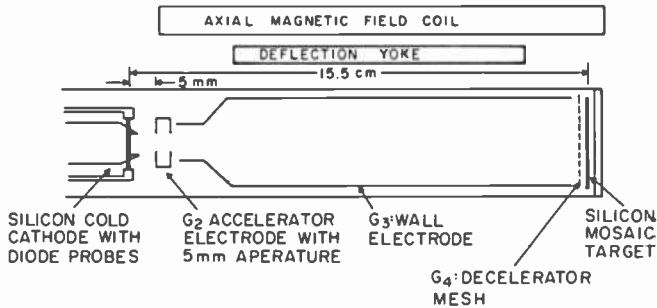


Fig. 5—Silicon cold-cathode vidicon tube design.

Cold-Cathode Vidicon Gun Design

For this initial NEA silicon cathode, an uncomplicated diode gun design was chosen that could easily be adapted to the electron optics of a standard 1.5-inch vidicon employing magnetic focus and deflection. The tube configuration is shown schematically in Fig. 5. Since the forward bias of the p-n junction regulates the amount of injected current and, thus, the emission current, the diode bias provides a beam control function equivalent to the G_1 voltage in the conventional triode gun. The positively biased G_2 provides the field necessary to draw the emitted electrons away from the cathode. To avoid having the G_2 electrode intercept any of the emission current, the aperture was made very large. In the magnetically focused tube, which re-images the emitter area on the target with unity magnification, the

well-defined area of the diode is relied upon to set the size of the scanning beam spot at the target. For this initial evaluation of the NEA emission, it seemed desirable not to collimate the beam in order that the full spread of electron energies at the target could be determined. The 5-mm spacing between the cathode and the G_2 electrode was dictated by the presence of the probe contacts to the diodes and the need to allow for illumination of the cathode surface during the NEA activation.

The support clamps and contact structure for the silicon cold-cathode wafers was made from either tantalum or tungsten to avoid possible contamination during the high-temperature heating required for the cathode processing.

The role of variation in contact resistance at the clamps was not determined, since no samples with bonded metal electrodes were completed. Preparation of samples with ohmic contacts to both the n wafer and the polycrystalline p silicon covering each mesa was delayed by difficulties in depositing adherent layers of tungsten or molybdenum. A technique for electroding a structured silicon device with refractory materials that will survive heating to 1200°C has not been necessary in prior device technology and remains to be developed.

Contact to the p silicon of the diode mesa is made by pointed tungsten probes formed into a one-turn spring in order to apply positive contact pressure. Lateral strain, which will cause the probe to shift position, must be avoided. A serious problem with the probe is its variable contact resistance. Considerable variation in the rectification characteristics was observed among individual diodes, and at times, large changes occurred during the NEA activation cycle. High emission levels were not obtained from diodes with poor rectification characteristics. Fig. 6 shows a typical rectifier characteristic for a good diode.

As mentioned earlier, the large size of the G_2 aperture and the wide spacing between the cathode and G_2 do not represent an optimum gun design. The silicon cathode was positioned so that the tube axis passed through the center of the square whose corners are defined by the four diodes of the cluster mask (see Fig. 4). Thus, no diode was located on axis, and, in operation, magnetic re-alignment was required for each individual diode.

The G_3 (wall) and G_4 (mesh) are the focus electrodes for the beam. A standard 16-mm diagonal silicon mosaic target was used as the photosensor.

The potentials on G_2 and G_3 that yield the best beam quality are

those for which the equipotentials at the G_2 aperture are flat. Based on the earlier experience that diode emission operating life is degraded by high G_2 potentials, the G_2 potential was limited to 100 volts.

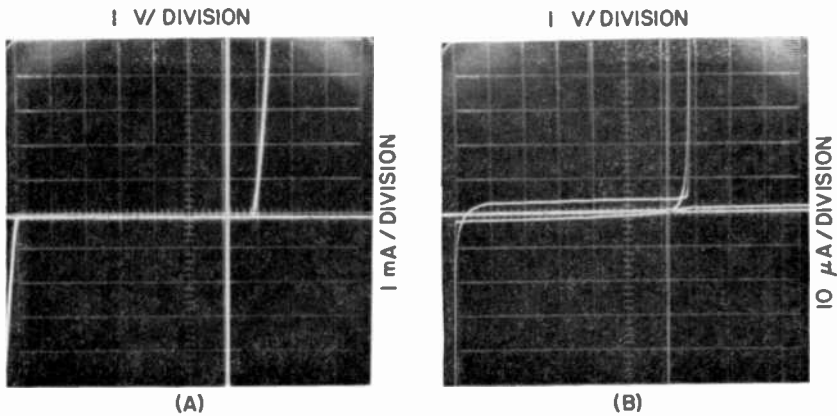


Fig. 6—Rectifier characteristic of silicon diode in cold-cathode structure.

Cold-Cathode Vidicon Gun Performance Evaluation

The basic emission efficiency and current density data for the various size diodes of the different cold-cathode patterns was provided by a series of test bottles containing only the silicon cold-cathode samples and an anode electrode. Emission current as a function of diode bias is shown in Fig. 7. The potential of the anode electrode was observed to exert a strong influence on the operating life of the NEA diode, as shown in Fig. 8. The more rapid drop in emission at higher anode potential suggests that positive ions generated at the anode cause bombardment damage at the cathode. The initial rise in emission shown in this figure is typical for cold cathodes in sealed bottles which have not been operated for a period of time.

The first vidicon tube with a NEA silicon diode cathode had no G_2 mesh to establish a planar decelerating field at the target, so this tube was incapable of providing a focused beam spot other than at the tube axis. The measured current to the target as a function of target potential is shown in Fig. 9. The 100-fold increase of target current in the first half volt above the cutoff potential is an indication of a narrow energy spread in the cold cathode beam.

The significant data for the beam-forming capability of silicon

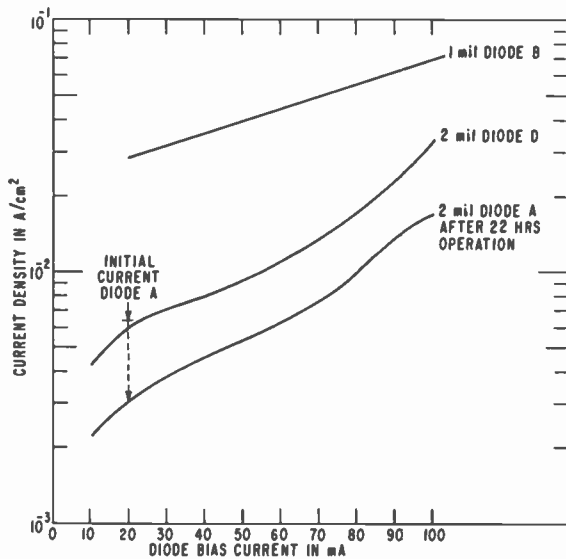
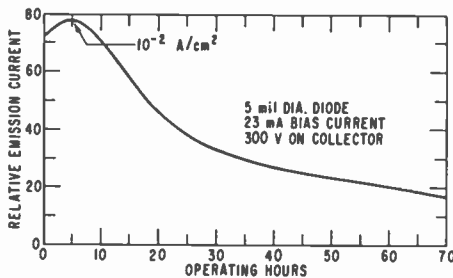
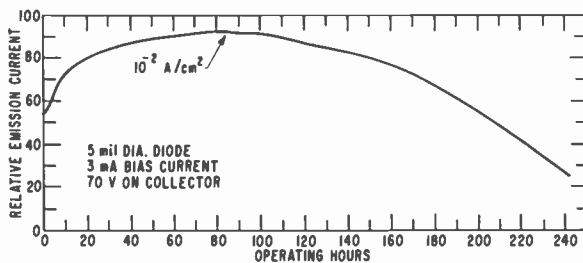


Fig. 7—NEA silicon emission current as a function of diode bias.



(a)



(b)

Fig. 8—NEA silicon emission as a function of operating life.

diode NEA emitters in vidicon tube structures of the design shown in Figs. 5 and 10 were obtained from three samples, CX-13, CX-15, and CX-19. Typical operating potentials were $G_2 = 100$ V, $G_3 = 225$ V, $G_4 = 360$ V; axial magnetic field was 40 gauss. As would be expected from a common design, there is considerable similarity in the measured characteristics.

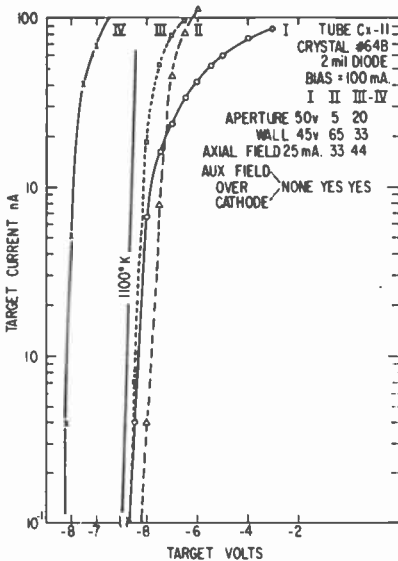


Fig. 9—Beam current collected at target as a function of target potential for cold-cathode vidicon tube CX-11 (no field mesh).

The performance feature that most clearly distinguishes these cold-cathode guns from the standard thermionic cathode in a similar vidicon tube is the target current versus target voltage. With the target made conducting by uniform illumination at high intensity and with a constant emission current from the cathode, the target current will reach a saturation value at some particular voltage above its cutoff potential. As shown in Figs. 11, 12, and 13, this value for the NEA silicon cathode is 1.5 volts; for a thermionic cathode it is typically 6-8 volts. This comparison is taken as proof that the energy spread among the electrons from the NEA cathode is significantly less than that from the thermionic cathode. Since this 1.5 volt spread is 3 times greater than was measured in the sample without the G_4 mesh, it is

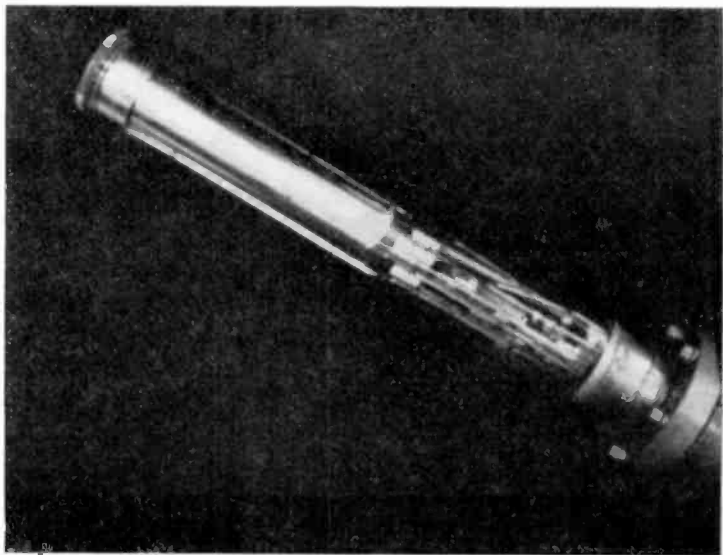


Fig. 10(a)—Photograph of experimental silicon cold-cathode vidicon tube.

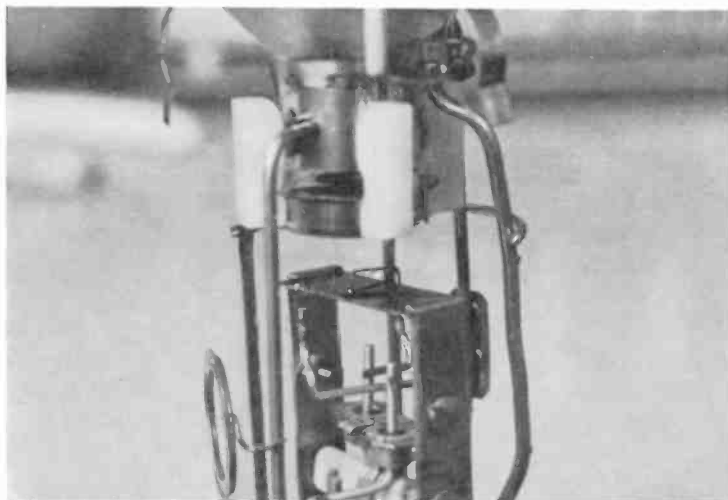


Fig. 10(b)—Detail of cathode mounting.

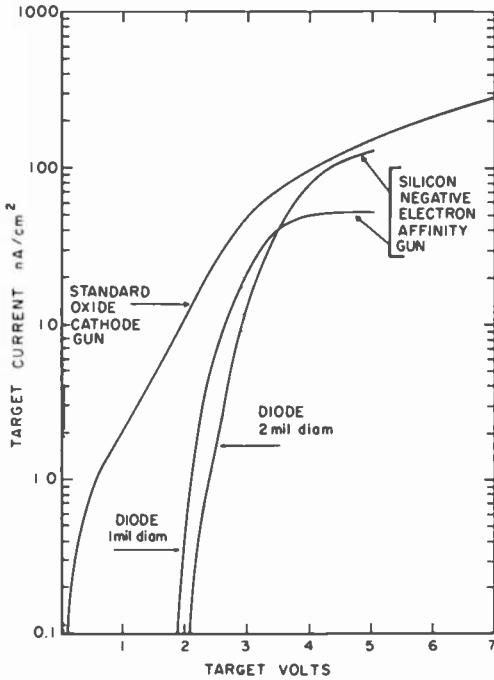


Fig. 11—Beam current collected at target as a function of target potential for cold-cathode vidicon tube CX-15. This is compared with typical thermionic cathode target current versus target voltage.

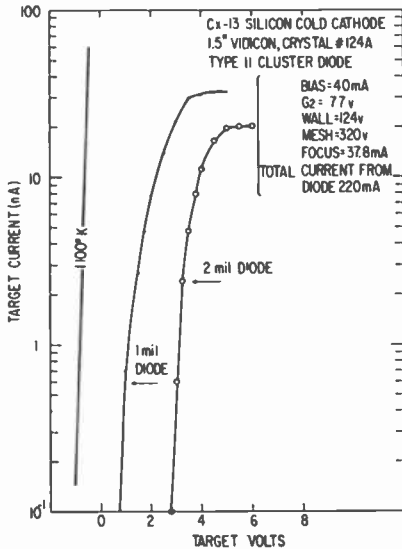


Fig. 12—Beam current collected at target as a function of target potential for cold-cathode vidicon tube CX-13.

evident that passage through the mesh broadens the electron energy spread within the beam by a significant amount.

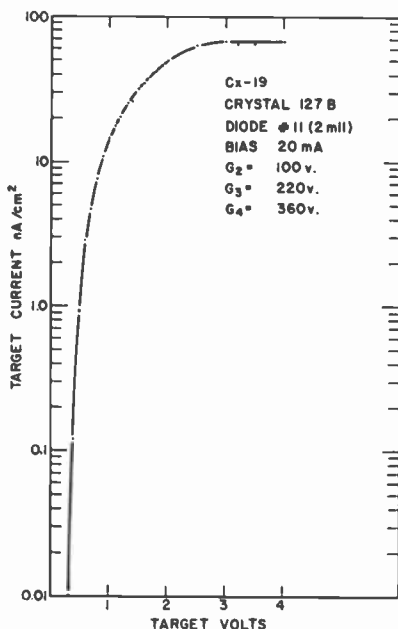


Fig. 13—Beam current collected at target as a function of target potential for cold-cathode vidicon tube CX-19.

A more exact measurement of the emission energy distribution at the NEA cathode was made by an ac retarding-potential method similar to that reported by Spicer and Berglund.⁶ The planar geometry of the G_2 electrode in the silicon vidicon tubes limits the accuracy of this measurement; nevertheless, the results shown in Fig. 14 represent the actual performance of the present geometry and can be viewed as a worst case limit. If an electrode structure were provided to prevent lateral spreading of the electrons in the region between the cathode and G_2 , the peak of the energy spread should be narrowed, and the low-energy tail that is present in the plots of Fig. 14 should be eliminated.

This retarding potential measurement was performed as follows: The G_2 , G_3 , and G_4 electrodes were connected together to serve as an anode to which a slowly varying retarding potential relative to the emitting surface (p side of the diode) was applied. An ac modulation of 25-30 mV was added to the dc potential which was swept through

a range of several volts from negative to positive. The output signal, plotted by an x - y recorder, is the derivative of the anode current as a function of the retarding potential between cathode and anode. Fig. 15 shows the circuit employed.

Constant cathode emission of $N_E(dE)$ electrons per second with energy between E and $E + dE$ yields an anode current I_A which is

$$I_A = e \int_{-eV_A}^{\infty} N_E dE.$$

Thus, $\left. \frac{dI_A}{dV_A} \right|_{V_{A1}}^{V_{A2}}$ as a function of retarding potential V_A is propor-

tional to the energy distribution of the emitted electrons when I_A is sufficiently small that space charge can be neglected. This ac detection method allows significantly smaller values of I_A to be used than in a dc measurement.

Curves A and B of Fig. 14 give the energy distribution from IR photoexcitation of the illuminated diode and mesa. Curves C and D give the cold emission energy distribution from the same diode when forward biased. Results are similar and indicate that the energy spread is of the order of 0.3 eV at the mid-point of the distribution peak. The high-energy side has a sharp cutoff, whereas the low-energy side is characterized by a low-amplitude tail that extends over more than 1.5 volts. Varying the diode current (either photoemission or diode injection emission) by 20% produced no measurable change in the energy distribution.

The major limitation in vidicon performance for the tubes with NEA silicon cathodes was the low value of the saturated target current which did not exceed 80 nA/cm². A target current of 700-800 nA/cm² is required for the silicon target tube. Evident in the measured performance is the small fraction of the total beam current that reaches the target. The mesh current is between 5 and 10 times greater than the target current. The mesh transmission is between 50 and 55%, and the fraction of the beam absorbed by the silicon target is reported⁷ to be 0.36, which would predict that the beam current is 5.6 times greater than the target current. Cesium adsorption at the target could further reduce the beam acceptance accounting for the experimental results.

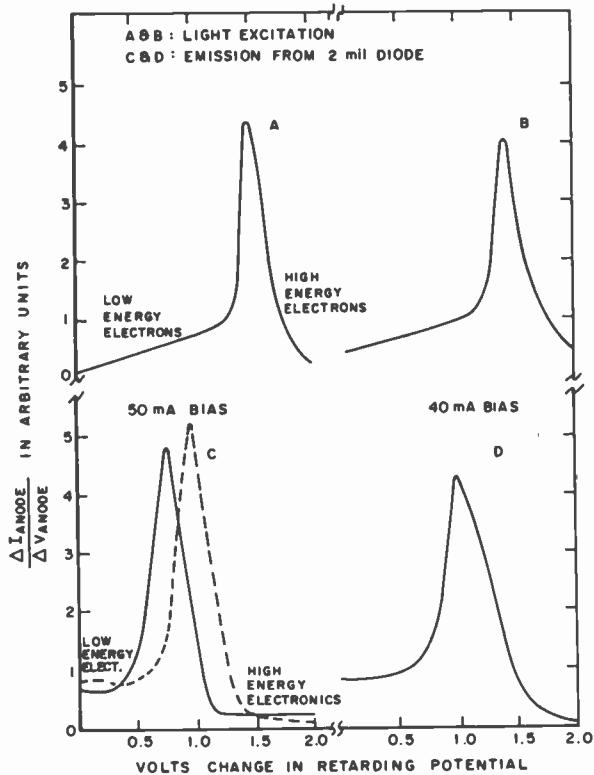


Fig. 14—Emitted electron energy distribution ($\Delta I/\Delta V$) from a NEA silicon diode as measured by ac retarding potential technique.

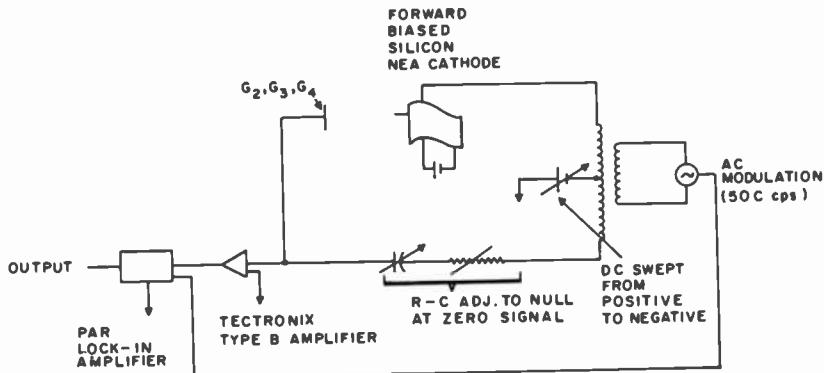


Fig. 15—Diagram of ac retarding potential emission energy measurement circuit.

With the signal level at the target in the 50-70 nA/cm² range, a low signal-to-noise ratio limits the performance to such an extent that no significant difference either in resolution or rate of signal rise and decay could be detected when the performance of the NEA silicon cathode tubes were compared with the standard thermionic-cathode silicon vidicons operating at the same target current.

Fig. 16 is a photograph of the kinescope display of the video signal from a silicon cold-cathode vidicon illuminated by a resolution pattern. The highlight level is 70 nA/cm².

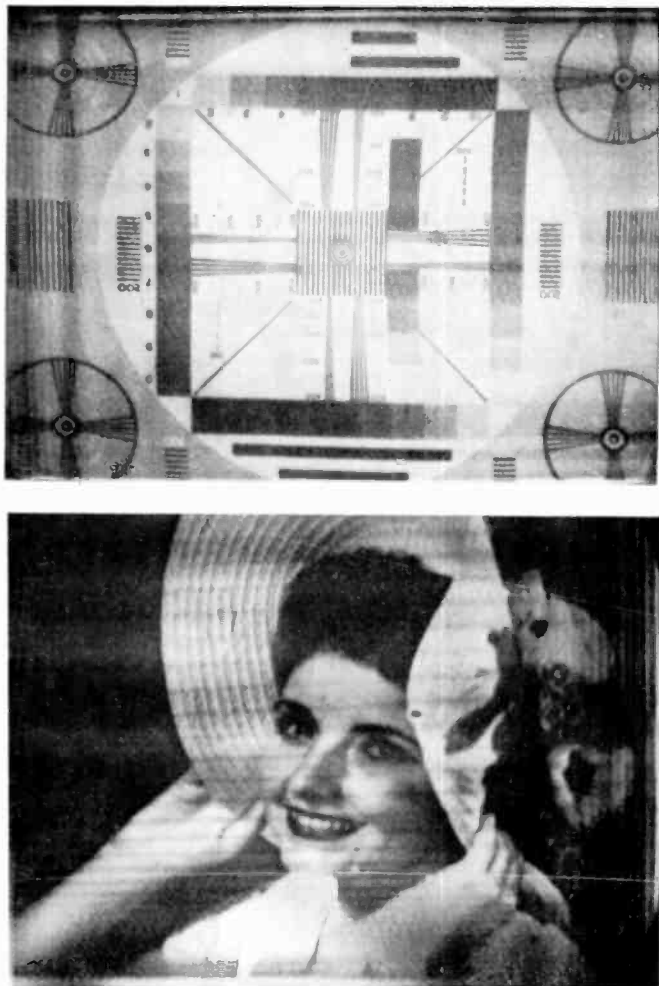


Fig. 16—Photograph of video display from the output signal of a silicon cold-cathode vidicon.

Fig. 17 shows the rate of signal rise and decay in time increments of 1/60 sec field scan rate for the cold-cathode vidicon. There is no significant difference between the cold-cathode dynamic behavior and the thermionic-cathode vidicon at this signal level.

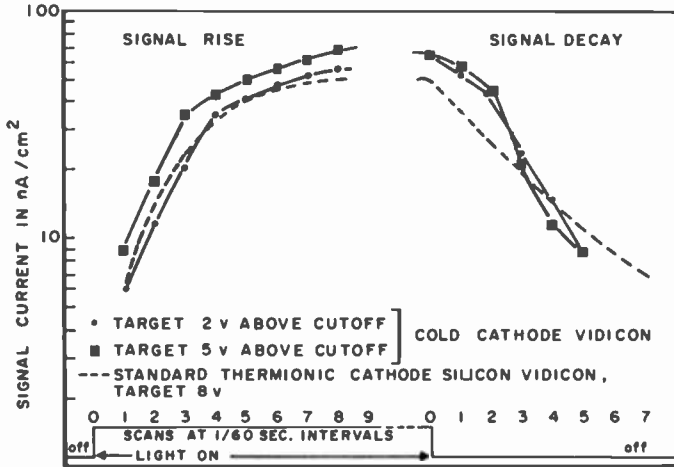


Fig. 17—Rate of signal rise and decay of a silicon cold-cathode vidicon compared with the standard thermionic-cathode vidicon at 50 nA/cm² signal level.

In the cold-cathode vidicon, the signal uniformity remains unchanged as the target is biased to cutoff, indicating that a uniform potential is maintained across the entire surface at small target modulations. This characteristic should yield resolution uniformity and reliable contrast discrimination exceeding that of the normal thermionic-cathode tube.

By applying a -40 V blanking pulse on the G₂ electrode operating at 100 V, the return traces were effectively blanked from the video signal.

The current density from the operable diodes in the three tubes that provided most of the operating data is given in Table 1. These values are lower than the best NEA silicon diode activations obtained in test bottles. The expectation that stable emission values between 10⁻¹ and 1 amp/cm² can be obtained in gun structures is not overly optimistic. The 4-6 volt drop across the diode leads when operating at 20-50 mA bias is excessive and should be reduced by improved contacts,

Conclusions

A negative-electron-affinity-activated silicon-diode cold cathode has been successfully adapted to a vidicon gun structure. The narrow spread in emission energy of the electrons forming the cold-cathode beam was measured both at the cathode and at the silicon mosaic target of the experimental vidicon tubes that were built. Even with the increase over the initial emission-energy spread resulting from the limitations of the simplified gun design that was used (from 0.3 eV to 1.5 eV), the cold-cathode beam contains markedly less energy spread than the beam from the conventional thermionic cathode, which is 4-5 times greater.

Table 1—Emission Current Density Obtained with Three Experimental Diodes

Tube	Emission Current Density (amp/cm ²)		Stable Operating Time (hours)
	25- μ m diameter diode	50- μ m diameter diode	
CX-13		10 ⁻²	3
CX-15	1.2 \times 10 ⁻²	2 \times 10 ⁻³	12
CX-19	5 \times 10 ⁻²	5 \times 10 ⁻²	45

It is evident from the spread of beam electron energies measured at the target (\approx 1.5 eV), as compared with the energy spread measured at the cathode (\approx 0.3 eV) that this gun design should be improved in future work. What appears to be required is an electrode configuration that would prevent the high current density at the cathode from being reduced through lateral spreading as the electrons are accelerated toward the target. This is similar to the problem of beam-injecting guns for magnetrons or travelling-wave tubes and would probably benefit from the type of beam-forming electrodes employed in Pierce gun designs.⁶

The capability to obtain a saturated target current at a bias of 2-3 volts on the silicon mosaic target, rather than 8 volts, could provide a significant reduction in the operating dark current of a silicon vidicon. Although the peak target current from the tubes that were completed for this project is only 70 nA per cm² (about 1/10 the current required for a good vidicon gun), the emission current density was less than 1/10 that which has been obtained in the best NEA activations of similar diodes. With further experience in improving the stabilized activation of the NEA silicon surface, the required increase in current should be attainable.

The maximum life for stable emission was increased from 2 to 3 hours to more than 40 hours of operation by modification of the activation process. Since this stable emission level is only $\frac{1}{3}$ the peak emission, it appears reasonable to anticipate further improvement.

The absence of thermal radiation from a hot cathode along with a beam composed of electrons having a narrow range of emission energies makes this type of cold cathode hold considerable promise for application in infrared and low-light-level devices. However, the variable results of the high-temperature processing of the structured silicon cold-cathode wafer that has been employed to prepare the surface for NEA activation suggest that initial processing of the cathode outside the final structure might be required. This calls for development of a successful means for transfer of a pre-processed cathode into the final device.

The well-defined area of the emitting diode does not require further collimation to define the scanning spot size. Diodes with 25 and 50 μm cross-sections were evaluated in this program. There does not appear to be any fundamental reason why 10 μm diodes of good quality cannot be grown. Experience in operating small diodes may reveal a limitation related to the current density at the perimeter of the diode, which will determine the maximum emission density. No such problem was evident in comparing the 25- and 50- μm diodes.

Acknowledgments

The authors are indebted to G. S. Briggs and C. P. Hadley of RCA Electronic Components, Lancaster, Pa., who prepared the structured wafers for this program. Also, consultations with E. S. Kohn, R. U. Martinelli, and the administrative direction of B. F. Williams are gratefully acknowledged.

References:

- ¹ E. S. Kohn, "Cold-Cathode Electron Emission from Silicon," *Appl. Phys. Letters*, Vol. 18, p. 272, 1 April 1971; "The Silicon Cold Cathode," *IEEE Trans. Electron Devices*, Vol. ED-20, p. 321 (1973).
- ² R. U. Martinelli, "Infrared Photoemission from Silicon," *Appl. Phys. Letters*, Vol. 16, p. 261, 1 April 1970; "Negative Electron Affinity Surfaces on Silicon Using a Rubidium/Oxygen Dipole Layer," *J. Appl. Phys.*, Vol. 44, p. 2566, June 1973.
- ³ B. Goldstein, "LEED, Auger, and Plasmon Studies of Negative Electron Affinity on Si Produced by the Adsorption of Cs and O," *Surface Sciences*, Vol. 35, p. 227, March 1973.
- ⁴ J. D. Levine, "Structural and Electronic Model of Negative Electron Affinity on the Si/Cs/O Surface," *Surface Sciences*, Vol. 34, p. 90 (1973).
- ⁵ R. Lieberman and D. L. Klein, "Temporary Protection of Silicon Surfaces by Iodine Films," *J. Electrochem. Soc.*, Vol. 113, p. 956, Sept. 1966.
- ⁶ W. E. Spicer and C. N. Berglund, "Measurement of Photoemitted Electron Energy Distributions by an AC Method," *Rev. Sci. Instr.*, Vol. 35, p. 1665 (1964).
- ⁷ R. W. Engstrom and J. H. Sternberg, "The Silicon Return-Beam Vidicon—A High-Resolution Camera Tube," *RCA Rev.*, Vol. 33, p. 501, Sept. 1972.
- ⁸ J. R. Pierce, *Theory and Design of Electron Beams*, 2nd. ed., D. van Nostrand Co., New York, N. Y. (1954).

Field-Effect Electroluminescence in Silicon*

Alvin M. Goodman

RCA Laboratories, Princeton, N.J. 08540

Abstract—A new approach is suggested for overcoming the primary difficulties that have impeded the development of high efficiency visible dc electroluminescence. The essential feature of the suggested devices is the use of one or more insulated-gate field-effect electrodes to induce a p-n junction (or a p-i-n junction with a narrow i-region) in a previously homogeneous semiconductor material. The junction is then forward-biased to produce injection electroluminescence. The possible use of field-assisted injection of carriers at a blocking contact is also suggested.

In this work, model devices employing silicon as the semiconductor (and emitting in the infrared region of the spectrum) have been used to demonstrate field-assisted injection of carriers at a blocking contact and dc field-effect electroluminescence. The use of higher bandgap (preferably direct) material is necessary to produce useful operation of field-effect electroluminescent devices in the visible region of the spectrum.

1. Introduction

The most efficient solid-state dc electroluminescent device configuration is that of a forward-biased p-n junction in a III-V compound or alloy. Such devices have external quantum efficiencies as high as 15% and 32% in the red¹ and infrared² regions of the spectrum, respectively, but drop to values of the order of 0.1% in the yellow and green. Several approaches exist for extending the region of efficient electro-

* A preliminary version of this paper was presented at the European Semiconductor Device Research Conference, Munich, Germany in March 1971.

luminescence to shorter wavelengths. One is the development of new high-energy direct-bandgap III-V materials such as $\text{In}_{1-x}\text{Ga}_x\text{P}$ and GaN .^{3,4} A second is the exploration of impurity recombination in indirect bandgap GaP where red,⁵ yellow,⁶ and green,^{7,8} luminescence have been attained. A third approach is that of double injection into a normally insulating highly efficient luminescent material in which p-n junctions cannot be fabricated; e.g., anthracene in which an external quantum efficiency of 8% has been achieved.⁹ A fourth approach is that of field ionization of deep traps in the insulating region of an M-i-n (metal-insulating-n-type) diode structure; light is generated when the ionized trap is neutralized by a radiative transition. An example of this is in work with $\text{GaN}:\text{Zn}$; here, blue-green light has been obtained with 1% external quantum efficiency.¹⁰ A fifth approach—to be treated in this paper—involves the use of one or more field-effect electrodes to induce a p-n or narrow p-i-n junction in a material that can not be doped both p- and n-type.

In past years, a considerable amount of work has been carried out on II-VI compounds, which are well known to be efficient materials for photoluminescence and cathodoluminescence in the visible region of the spectrum.¹¹ The major stumbling-block to the use of large bandgap II-VI materials has been the difficulty of fabricating p-n homojunctions by any conventional technique.*^{12,13} One possibility is that a field-effect electrode could be employed to invert the conductivity type of part of a semiconductor luminescent layer, creating a p-n junction electrically.¹⁴ Thus, the major problem with the II-VI compounds would be by-passed. A similar but somewhat simpler scheme requiring ac excitation has been demonstrated.**¹⁵

The purpose of this paper is (1) to extend the ideas previously described in Ref. [14] and (2) to describe the structure and operation of a working field-effect electroluminescent device (FEELD). In spite of its bandgap in the infrared region of the spectrum and its very low photoluminescent quantum efficiency ($\sim 10^{-5}$), silicon was chosen as the luminescent host material for a demonstration device or model because (1) silicon device technology is highly developed, (2) high quality silicon is available, and (3) silicon surfaces can be passivated

* High resistivity p-type conduction has been obtained in both CdS ¹² and ZnSe ,¹³ but this has not, as yet, led to useful electroluminescent devices.

** An ac-operated two-terminal electroluminescent device employing an insulated field-effect electrode to produce a p-n junction electrically in gallium arsenide has been described by C. N. Berglund.¹⁵ This device uses Zener or avalanche generation of hole-electron pairs to produce minority carriers in the region adjacent to the field plate insulator. The minority carriers are then swept into the bulk (on alternate half cycles of applied voltage) where they recombine radiatively.

with ease (a *sine qua non* for field-effect devices). The extension of this work to higher bandgap materials is by no means trivial or obvious; it does, however, represent one possible approach to the further development of high efficiency visible electroluminescence.

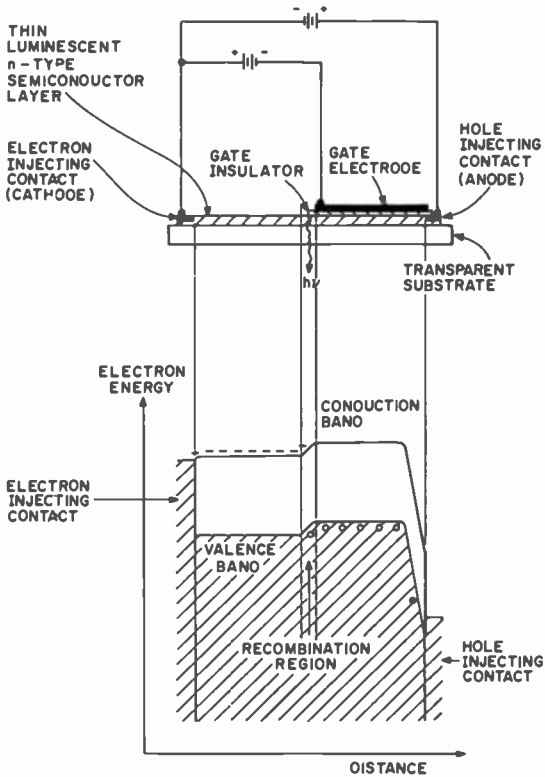


Fig. 1—Simplified electrode-configuration cross-section, schematic circuit, and energy-band picture for a single-gate FEELD. In this example the cathode is an ohmic contact for electrons; at the anode, holes enter by either thermionic emission or field-assisted injection.

2. Qualitative Theory

In this section the qualitative theory of two types of FEELD is presented along with a discussion of some contact considerations.

2.1 Single-Gate Device—Semiconducting Base Material

In Fig. 1 a simplified diagram showing the electrode configuration cross-section and energy-band picture of one variation of the device

is used to illustrate its operation. The energy-band picture is a profile along a line between the cathode and anode just beneath the semiconductor surface adjacent to the gate. For the sake of definiteness, the original semiconductor is assumed to be n-type ($n \sim 10^{16}/\text{cm}^3$). In this case, the majority carriers are electrons in the region not under the gate (field-effect electrode) and are holes in the inversion region under the gate. The electron-injecting contact (cathode) is assumed to be ohmic.

The hole-injecting contact (anode) may or may not be ohmic. If it is ohmic, holes may be injected with negligible voltage drop at the contact. If a barrier exists, the holes may be injected into the inversion region either by thermionic emission (possibly aided by Schottky effect) or by tunnel effect. Since the inversion region is depleted of electrons, tunnel-effect injection of holes can be quite efficient; i.e., there would be negligible electron extraction at the anode. Alternatively, hole-electron pairs may be produced by avalanche generation in the high-field region adjacent to the anode. The avalanche-generated holes would be swept into the inversion region and the avalanche-generated electrons would be extracted through the positive contact. The effect would be equivalent to injecting holes at the anode. Each of these modes of minority-carrier injection could be described by the generic term, *field-assisted injection*. The potential difference between the anode and the gate would in each case control the hole injection.

The barrier to recombination, and hence the recombination itself, would be controlled by the potential difference between the cathode and the gate. A modulating signal could be applied to any of the three terminals of the device.

The contacts are shown as metals in Fig. 1. Alternatively, semiconductor contacts (heterojunctions) could be used to inject holes and/or electrons into the luminescent layer. Only one electrode geometry has been shown in Fig. 1; many others are possible. In some of these, the electrodes and insulators could be applied in the form of strips (or other patterns) by evaporation through a mask or by photolithographic techniques. If the injecting contact (anode and cathode) strips were perpendicular to the gate strips, it would be possible to select those portions of a large-area array that are to be illuminated by placing the proper potentials on the electrode lead matrix.

2.2 Double-Gate Device—Insulating Base Material

In Fig. 2 a simplified diagram showing the electrode configuration cross-section, schematic circuit, and energy-band picture is used to

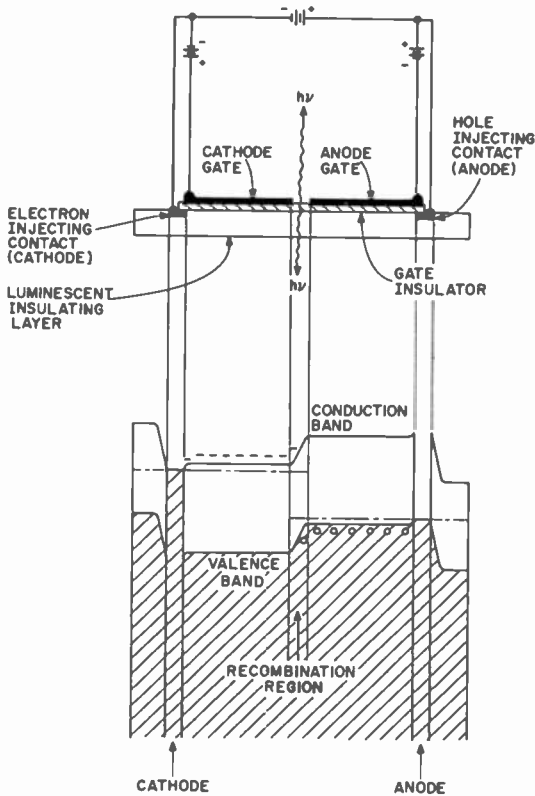


Fig. 2—Simplified electrode-configuration cross-section, schematic circuit, and energy-band picture for a double-gate FEELD. In this example, both the electron- and hole-injecting contacts are assumed to be ohmic.

illustrate the operation of the double-gate device.

The base material is insulating before the application of voltage to the electrodes. When a negative voltage is applied to the anode gate relative to the anode, the region just under the anode gate insulator becomes a p-type accumulation layer. Similarly, when a positive voltage is applied to the cathode gate relative to the cathode, the region just under the cathode gate insulator becomes an n-type accumulation layer. A voltage applied between the anode and cathode (as shown in Fig. 1) causes both electrons and holes to be injected into the region between the accumulation layers where they can recombine. The resulting luminescence can then be viewed from above (if the insulating layer is transparent) or below (if the self-absorption of the insulator is not too great).

It has been assumed in this explanation that the anode and cathode contacts are ohmic for holes and electrons, respectively. If this is not true, carrier injection at a barrier contact may be obtained by field-assisted injection as described in Section 2.1 above.

The electrode arrangement shown in Fig. 2 is one variation of the double gate FEELD; many others are possible.

3. Experiments

3.1 Rationale

To fabricate a working device of the type described in the last section, it is desirable to start with a host luminescent material for which the following statements are true:

1. Surface passivation is possible to the extent that the density of electronic states at the interface between the semiconductor and the gate insulator is of the order of $10^{11}/\text{cm}^2$ or less. This will permit the electric field lines from the gate to penetrate the interface and terminate on charges inside the semiconductor.
2. The technology exists for making electrical contacts to the material and for forming or applying a thin dielectric layer of high breakdown strength on its surface.
3. The material is of good quality with a density of deep-lying states in the forbidden gap of the order of $10^{15}/\text{cm}^3$ or less.
4. The material exhibits efficient photoluminescence in the visible region of the spectrum.

Unfortunately, at the present time, no material fulfills these conditions completely. The one material that is accurately described by the first three statements, (silicon) is a very inefficient luminescent material and, further, its bandgap radiation is in the infra-red region of the spectrum. Nevertheless, it offered the best chance to demonstrate a working FEELD, albeit an inefficient one, without an extensive program of research and development on luminescent materials per se.

Section 3.2 below describes the use of a standard silicon transistor, to demonstrate field-assisted injection of minority carriers with the resulting emission of light. In Section 3.3, the structure and operation of a double-gate FEELD are described.

3.2 Half-Gate Transistor Experiment

A half gate n-channel MOS transistor (with protective can removed) was operated as shown in Fig. 3. Note that the polarity of the source and drain are inverted relative to the usual circuitry for this type of

transistor.¹⁶ When $V_G = -14\text{V}$, the unit was cut off; i.e., no current flowed through the transistor and there was no electroluminescence. When $V_G = -26\text{V}$, field-assisted injection of holes occurred from the source into the base as shown by the plot of source current versus source voltage in Fig. 3c, and light was detected by the PbS cell.

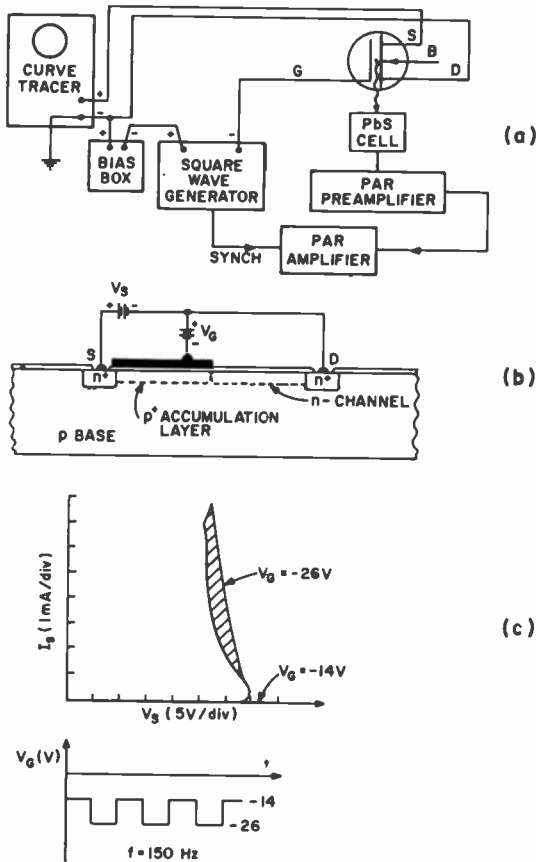


Fig. 3—Field-assisted injection of minority carriers resulting in electroluminescence; (a) experimental arrangement, (b) electrode arrangement and polarities of applied voltages, and (c) source current versus source voltage and gate voltage versus time.

Although the field-assisted injection of holes at a barrier contact (reverse-biased p-n junction) is unambiguous, the source of the light is not. It could be emanating either from the forward-biased junction formed by the n-channel and the p⁺ accumulation layer (and the p-type base) or from the hole-injection contact if the injection is due to avalanche breakdown.

As a result of this experiment, it was clear that a different type of structure (one not requiring field-assisted injection) was needed to demonstrate, unambiguously, injection electroluminescence at a field-induced p-n or p-i-n junction. Such a structure is considered in the next section.

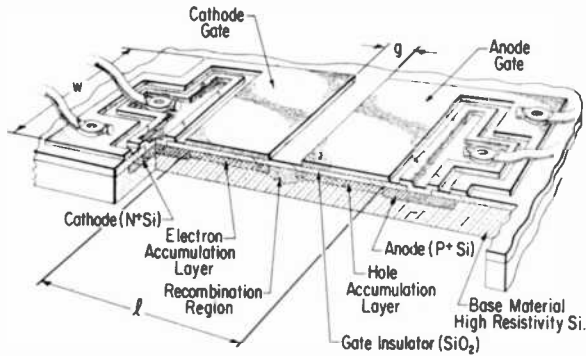


FIG. 4

Fig. 4—Cut-away sketch of a double-gate silicon FEELD.

3.3 Double-Gate FEELD

A double-gate device similar to that described in Sec. 2.2 was fabricated using high resistivity silicon ($\rho > 1500$ ohm-cm) as the base material. A cutaway sketch of the device structure is shown in Fig. 4. The structure and circuit are similar to those shown in Fig. 2 with the exception that the cathode and anode are n⁺ and p⁺ Si, respectively, in order to avoid the necessity for field-assisted injection. The gap g is 0.002 inch and the distance l between the cathode and anode is approximately 0.012 inch. The width w of each gate electrode is 0.012 inch. The dependence of the current-voltage characteristic of the device on gate bias polarity is illustrated in Fig. 5. For the uppermost curve, the polarities are those shown in Fig. 2. For the lowest curve, the gate polarities have been reversed. The current flow is much reduced but is not cut off as it would be if the Si base were truly insulating. The second curve from the top is primarily due to electron current, because the polarity of both gates is positive relative to the corresponding injecting electrodes. The second curve from the bottom is primarily due to holes, because the polarity of both gate electrodes is negative.

The experimental arrangement shown in Fig. 6 was used to detect the light output of the FEELD. A plot of light output versus current

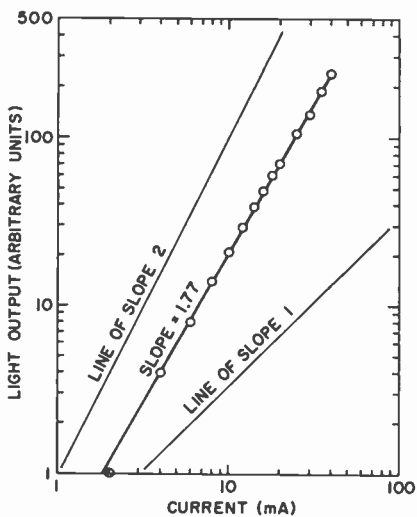


Fig. 7—Relative light output versus current of a double-gate silicon FEELD.

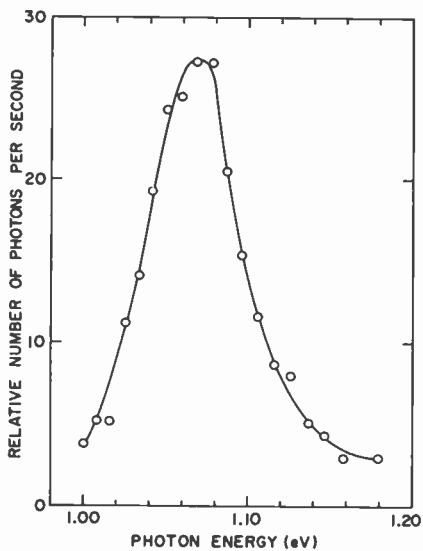


Fig. 8—Relative light output versus photon energy of a double-gate silicon FEELD.

To demonstrate the gate modulation capability of the device, the mechanical light chopper was removed from the beam and the light was modulated instead by a square-wave voltage applied to one of the two gates. The experimental arrangement was similar to that in Fig. 3(a). A plot of modulated light output versus gate modulation voltage is shown in Fig. 9. Note that the modulation voltage causes

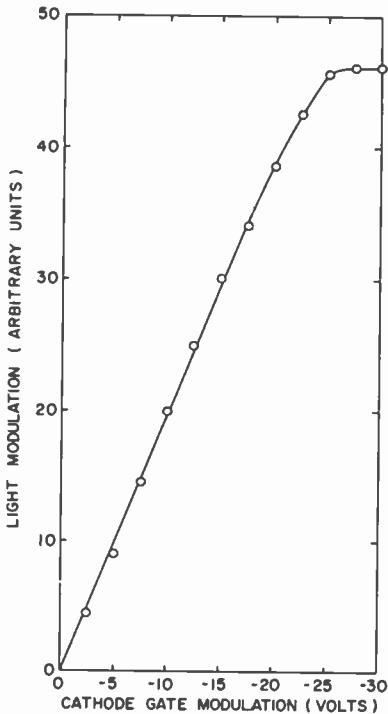


Fig. 9—Modulated light output versus cathode-gate modulation voltage of a double-gate FEELD.

a decrease in the magnitude of the total voltage applied to the gate and, thus, the modulation represents a decrease from a maximum light output. The saturation occurs when increasing negative modulation voltage on the cathode gate can no longer decrease the electron current through the device. A similar result was obtained for anode gate modulation.

It may be argued that similar EL could have been obtained more simply by double injection from contacts separated by a narrow intrinsic region. It is therefore appropriate to state the advantages of the double-gate device configuration.

1. If one of the contacts were blocking or partially blocking, the gate could be used to promote field-assisted injection. This would prevent carrier extraction at the blocking electrode.
2. If both contacts were blocking or partially blocking, gate electrodes would make carrier injection possible without extremely narrow cathode-anode spacing.
3. The use of gates allows the region of recombination to be physically separated from the contact region. This may be important if the contact fabrication process spoils the adjacent material for luminescence.
4. The use of gates allows an additional flexibility in the control of the light output.

4. Summary

Model devices employing Si as the semiconductor have been used to demonstrate that the principle of field-effect electroluminescence is sound. However, the use of higher-bandgap (preferably direct) material is necessary to produce useful operation of field-effect electroluminescent devices in the visible region of the spectrum.

Acknowledgment

The author is indebted to A.G. Fischer, A.G. Kokkas, and J.H. Scott for helpful discussions; A.G. Kokkas and J. Murr, Jr., for fabrication of the double-gate silicon devices; J.M. Breece for assistance with the experiments; and C. J. Nuese and J. I. Pankove for constructive comments on the manuscript.

References:

- ¹ R. Solomon and D. DeFever, "Efficiency Shift in Very High Efficiency GaP (Zn-0) Diodes," *Appl. Phys. Letters*, Vol. 21, p. 257 (1972).
- ² I. Ladany, "Electroluminescence Characteristics and Efficiency of GaAs:Si Diodes," *J. Appl. Phys.*, Vol. 42, p. 654 (1971).
- ³ C. J. Nuese, A. G. Sigai, and J. J. Gannon, "Orange Laser Emission and Bright Electroluminescence from In_{1-x}Ga_xP Vapor Grown P-N Junctions," *Appl. Phys. Letters*, Vol. 20, p. 431 (1972).
- ⁴ J. I. Pankove, E. A. Miller, D. Richman, and J. E. Berkeyheiser, "Electroluminescence in GaN," *J. Luminescence*, Vol. 4, p. 63 (1971).
- ⁵ H. G. Grimmeiss and H. Scholz, "Efficiency of Recombination Radiation in GaP," *Phys. Letters*, Vol. 8, p. 233 (1964).
- ⁶ R. Nicklin, C. D. Mobsby, G. Lidgard, and P. B. Hart, "Efficient Yellow Luminescence from Vapour Grown Gallium Phosphide with High Nitrogen Content," *J. Physics*, Vol. C4, p. L344 (1971).
- ⁷ P. J. Dean, M. Gershenson, and G. Kaminsky, "Green Electroluminescence from Gallium Phosphide Diodes near Room Temperature," *J. Appl. Phys.*, Vol. 38, p. 5332 (1967).

- ⁸ I. Ladany and H. Kressel, "An Experimental Study of High-Efficiency GaP:N Green-Light-Emitting Diodes," *RCA Review*, Vol. 33, p. 517 (1972).
- ⁹ J. Dresner, "Double Injection Electroluminescence in Anthracene," *RCA Review*, Vol. 30, p. 322 (1969).
- ¹⁰ J. Pankove, "Blue-Green Numeric Display Using Electroluminescent GaN," *RCA Review*, Vol. 34, p. 336, June 1973.
- ¹¹ A. G. Fischer, "Electroluminescence in II-VI Compounds" in *Luminescence of Inorganic Compounds*, edited by Paul Goldberg, Academic Press, New York 1966.
- ¹² M. Lichtensteiger, I. Lagnado, and H. C. Gatos, "P-type Cadmium Sulfide Crystalline Films," *Appl. Phys. Letters*, Vol. 15, p. 418 (1969).
- ¹³ P. Won Yu and Y. S. Park, "P-type Conduction in Undoped ZnSe," *Appl. Phys. Letters*, Vol. 22, p. 345 (1973).
- ¹⁴ A. M. Goodman, "Electroluminescent Device and Method of Operating," U.S. Patent No. 3492548, Jan. 27, 1970.
- ¹⁵ C. N. Berglund, "Electroluminescence using GaAs MIS Structures," *Appl. Phys. Letters*, Vol. 9, p. 441 (1966).
- ¹⁶ RCA Transistor Manual, Technical Series SC-13 (RCA Electronic Components, Harrison, N.J.) 1967.
- ¹⁷ J. R. Haynes and W. C. Westphal, "Radiation Resulting from Recombination of Holes and Electrons in Silicon," *Phys. Rev.*, Vol. 101, p. 1676 (1956).
- ¹⁸ W. C. Dash and R. Newman, "Intrinsic Optical Absorption in Single-Crystal Germanium and Silicon at 77°K and 300°K," *Phys. Review*, Vol. 99, p. 1151 (1955).

Negative Resistance in Cadmium Selenide Powder—Relative Absorption Coefficient

L. J. Nicastro

RCA Advanced Technology Laboratories, Camden, N. J.

E. L. Offenbacher

Temple University, Philadelphia, Pa.

Abstract—Cadmium Selenide powder, upon the incorporation of copper and chlorine impurities, exhibits a negative resistance type of current-voltage behavior when the voltage across the sample exceeds a certain threshold value, V_{th} . The value of this threshold is reduced when visible or near infrared electromagnetic radiation is incident upon the sample. This was reported and explained in an earlier paper.⁴

The amount that V_{th} is reduced depends on the fraction of the incident radiation that is absorbed. This fraction is characterized by the absorption coefficient α of the material. In CdSe, α is a strong function of the wavelength of the monochromatic light used, especially for photon energies near the crystal bandgap energy. In this communication the V_{th} dependence on the wavelength of the incident light is reported for 44 different wavelengths. On the basis of the model previously described, one can calculate from these data the dependence of α on wavelength. It was found that the α curve peaks at energies corresponding to transitions between the conduction band and certain known acceptor levels. Consequently the results of this type of experiment can be used to identify the impurity states that take part in the negative resistance effects of CdSe.

1. Introduction

Pure cadmium selenide (CdSe) is an insulator with a bandgap energy of 1.7 eV. Negative resistance in the current-voltage characteristic of CdSe powder was first reported by Nicoll.¹ The effect is observed only after copper and chlorine impurities are added to CdSe powder through a series of specialized processes described by Hinnenkamp.²

When the voltage applied across a sample of this CdSe powder exceeds a certain threshold value V_{th} , negative resistance is observed as an abrupt increase in current, while the voltage across the sample decreases. This dark threshold voltage is reduced by irradiating the sample with visible or near infrared radiation.¹ Smith³ also observed that after the threshold voltage has been exceeded, the material emits radiation equivalent to the bandgap and lower frequencies. In accordance with a model described in a previous paper,⁴ this emission of light is due to radiative recombination of conduction-band electrons both with unfilled acceptor levels and with holes in the valence band; the reabsorption of part of the recombination radiation within the material provides excess electrons to the conduction band. When external light is incident on the sample the production of excess electrons in the conduction band is enhanced, and thus the threshold voltage is reduced.

The model previously described⁴ is based on the rate equation for the production of excess electrons in the conduction band in conjunction with the following assumptions. (1) The initial current density is proportional to the first power of the voltage. (2) The quantum efficiency for radiative recombination of current carriers is an increasing function of the current density. (3) The effective current density consists of the sum of the pre-breakdown current and a linear photocurrent generated by the absorption of electron-hole recombination radiation. This model is very similar to the model first described by Dumke^{5,6} and extended by Weiser⁷ to explain the negative-resistance characteristic in single-crystal GaAs p-i-n junctions. It differs only in that their model assumed a quadratic dependence of the pre-breakdown current on voltage, while a linear dependence of pre-breakdown current on voltage gives the best representation for the experimental results obtained with CdSe.

The model predicts that the threshold voltage with incident light present, $V_{th(I)}$, is proportional to $1/\sqrt{\alpha I}$, where α is the absorption coefficient and I is the incident light intensity. An investigation of the variation of threshold voltage with light intensity at two wavelengths (constant α at each wavelength) has been reported,⁴ and cor-

relation between the theoretical relation and experiment was found to be good. In this paper, measurements of the threshold voltage with light incident at 44 wavelengths in the visible and near infrared are reported, and the data from the observations are used to obtain the relative absorption coefficient of CdSe powder as a function of wavelength.

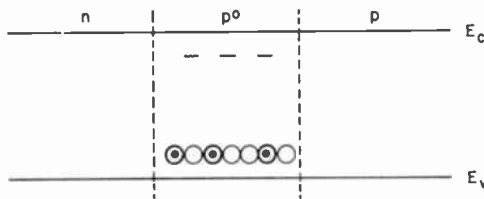


Fig. 1—Impurity scheme of p-p⁰-n material. E_c and E_v are the edges of the conduction and valence bands. The dashes signify ionized donors, dotted circles signify acceptors ionized by electrons, and the open circles correspond to acceptor levels that are not ionized. The n and p regions are heavily doped.

2. Theory of Negative Resistance

2.1 Description of the Model

An energy diagram of the model on which the theory is based is shown in Fig. 1. The n and p regions are considered to be heavily doped, the high-resistivity central region (the p⁰ region) is assumed to be lightly doped p-type, and it is also assumed that the width of the p⁰ region is many times the diffusion length of either electrons or holes. With these assumptions, negative resistance is brought about as follows. Under the positive bias voltage illustrated in Fig. 2, the electrons that traverse the high-resistance region combine with holes near the p⁰-p boundary. This recombination is partly radiative and some of the emitted light is absorbed in the p⁰ region, creating electron-hole pairs. Because of the presence of the negatively charged centers, which are presumed to have a large capture cross section for holes, the holes are immobilized and do not contribute to the conduction process. Therefore, the result of each absorption in the p⁰ region is to provide an additional electron to the conduction band and to produce a hole bound to a previously filled acceptor site. Until this hole decays, the additional electron in the conduction band contributes to the conduction process. Together with the injected electrons, the photo-generated electrons flow to the p⁰-p interface, recombine in part

radiatively, and hence create more electron-hole pairs. Thus, a regenerative process sets in if the quantum efficiency for radiative recombination is high enough and the field is strong enough for new electrons to be created in the p^o region at a rate faster than that at which they decay. Furthermore, the process leads to a negative resistance, as opposed to a simple feedback process, only if the quantum efficiency is an increasing function of the current at the beginning of the process. Under these conditions, the regenerative process can continue at lower and lower voltages as the quantum efficiency increases. When the quantum efficiency reaches a constant value, the process stops, and the dynamic resistance becomes positive again.

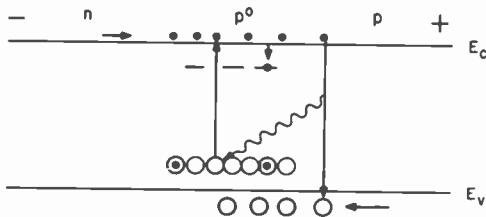


Fig. 2— p - p^o - n material with voltage applied.

2.2 Theoretical Relation Between $V_{th(I)}$ and I

It has already been noted that the pre-breakdown current-voltage relation across the p^o layer, which provides the best representation of the experimental results obtained with CdSe, is

$$j = aV, \quad [1]$$

where j is the current density, V is the voltage across the p^o layer (the total voltage across the material minus the voltage across the n - p^o junction), and a is a constant of the material. The current is carried by electrons and holes flowing toward the p^o - p junction (see Fig. 2), and some of the electrons that reach the p^o - p interface recombine radiatively with the holes of the p region. The flux density f of photons produced by radiative recombination is given by

$$f = \frac{\gamma j}{e}, \quad [2]$$

where γ is the internal quantum efficiency for radiative recombination

(≤ 1) and e is the electronic charge. A fraction ϕ of these photons are absorbed by filled acceptors of the p^0 region, producing conduction electrons and holes bound to the acceptors. The rate of production of excess electrons per unit volume Δn is

$$\frac{d(\Delta n)}{dt} = \frac{\phi}{L} f - \frac{\Delta n}{\tau}, \quad [3]$$

where L is the thickness of the p^0 region and τ is the recombination life-time of conduction electrons. In Eq. [3], the first term is the rate of absorption of recombination photons in the p^0 -region and the second term is the rate of decay of excess conduction electrons. On combining Eqs. [2] and [3], the rate at which excess electrons are produced is given by

$$\frac{d(\Delta n)}{dt} = \frac{\phi \gamma(j)}{Le} j - \frac{\Delta n}{\tau}, \quad [4]$$

where $\gamma(j)$ implies that the quantum efficiency is a function of the current density.

If, at time zero, the current is that given by Eq. [1], the presence of the extra electrons produced by the absorbed recombination radiation will add an ohmic component to the current, since the extra holes are assumed to be *immobile*. The total current density will then be given by

$$j = aV + \frac{\Delta ne\mu V}{L}, \quad [5]$$

where μ is the electron mobility. On substitution of Eq. [5] into Eq. [4], the rate equation becomes

$$\frac{d(\Delta n)}{dt} = \frac{\phi \gamma(j)}{Le} \left(aV + \Delta ne\mu \frac{V}{L} \right) - \frac{\Delta n}{\tau}. \quad [6]$$

The general case of letting the quantum efficiency be a function of current density is carried out by using the simple form of the dependence of γ on j suggested by Dumke,⁶ that is,

$$\gamma = \frac{\gamma_{\infty} j}{j + b}. \quad [7]$$

The solution of the rate equation is greatly facilitated by assuming that at the threshold of negative resistance, the quantum efficiency depends strongly on the current density, so that Eq. [7] is adequately approximated by

$$\gamma \approx \frac{\gamma_x j}{b}. \quad [8]$$

Using the above assumption, Eq. [6] becomes

$$\frac{d(\Delta n)}{dt} = \frac{\phi \gamma_\infty}{Leb} \left(aV + \Delta n e \mu \frac{V}{L} \right)^2 - \frac{\Delta n}{\tau}. \quad [9]$$

Integration of Eq. [9] yields the dark threshold voltage, V_{th} , in terms of the constants of the material.^{4,7}

In the absence of external illumination, the negative resistance is brought about by the generation of electrons in the p^o region by light given off at the p^o - p boundary, therefore a lowering of the threshold voltage is expected with light incident on the material. Making the assumption that the light is uniformly absorbed in the p^o layer, the rate equation may be written to take into account the presence of external illumination of intensity I . Thus, Eq. [9] becomes

$$\frac{d(\Delta n)}{dt} = \frac{\phi \gamma_\infty}{Leb} \left(aV + \Delta n e \mu \frac{V}{L} \right)^2 - \frac{\Delta n}{\tau} + \alpha I, \quad [10]$$

where I is given in photons/cm²/sec, and α is the absorption coefficient (cm⁻¹) of the p^o region. Integration of Eq. [10] yields

$$I = \frac{V_{th} j_{th} L}{\alpha e \mu \tau (V_{th(I)})^2} \left[1 - \left(\frac{V_{th(I)}}{V_{th}} \right)^2 \right], \quad [11]$$

where V_{th} is the dark threshold voltage, and j_{th} is the current density at the dark threshold voltage.^{4,7} This expression relates the threshold voltage $V_{th(I)}$ to the incident light intensity I and to the absorption coefficient α . It may be observed that $V_{th(I)}$ is proportional to $(\alpha I)^{-1/2}$ in the case where the light intensity is high enough so that the threshold voltage is reduced considerably, that is, when the term in brackets in Eq. [11] can be neglected.

2.3 Method of Determining Relative Absorption Coefficient

The relation between $V_{th(l)}$, I , and α in Eq. [11] depends on the wavelength of the incident light through the absorption coefficient α . If we let

$$v = \frac{V_{th(l)}}{\sqrt{1 - \left(\frac{V_{th(l)}}{V_{th}}\right)^2}} \quad [12]$$

in Eq. [11], then, after rearranging, the relation can be written

$$\alpha I v^2 = \frac{V_{th} j_{th} L}{e \mu \tau} \quad [13]$$

In this equation, all the variables have been placed on the left side; the right side of the equation is a constant independent of wavelength. Since Eq. [13] holds for all absorbed wavelengths, the relation can be written for any two wavelengths, and the constants of Eq. [13] can be eliminated. The result is

$$\alpha_1 I_1 v_1^2 = \alpha_2 I_2 v_2^2, \quad [14]$$

where the subscripts refer to two different wavelengths. If threshold voltages with light incident on the material are measured at various wavelengths and intensities of light, then relative absorption coefficients (α_2/α_1) can be obtained from Eq. [14]. When the absorption coefficient of a particular wavelength is known, the absorption coefficient for various wavelengths can be obtained relative to the known absorption coefficient. For purposes of comparison, the known absorption coefficient was taken to be that given by Parsons, Wardzynski, and Yoffe⁸ for pure, single-crystal CdSe at 500 nm. The absorption coefficient at 500 nm ($1.55 \times 10^5 \text{ cm}^{-1}$) was selected for comparison, because it is one of the shortest wavelengths (highest energy) for which the absorption coefficient was reported by Parsons, et al, and it was assumed that the energy at this wavelength was high enough for imperfection absorption to be negligible.

3. Methods and Procedures Used in the Experimental Investigation

The method of observing the current-voltage characteristic of CdSe in the dark is illustrated in Fig. 3. The circuit is shown simply as a

series circuit with dc-voltage source, an ammeter, and the CdSe sample. In Fig. 3, the current axis denotes the current through the circuit; the voltage axis depicts the voltage across the CdSe sample *only*. If the voltage across the sample-ammeter combination is increased from zero, at first there is no measurable current through the sample. When the voltage across the material reaches the threshold voltage V_{th} , the current rises rapidly while the voltage across the sample decreases. This is the negative-resistance region, which is indicated by the line with negative slope in Fig. 3. The passage

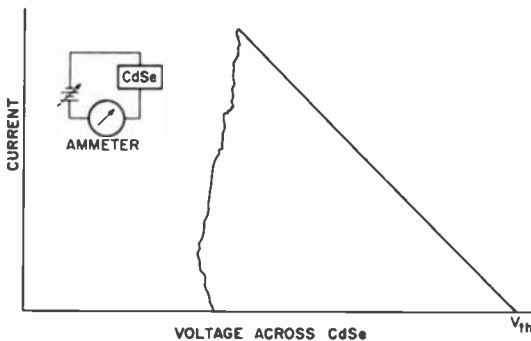


Fig. 3—Current-voltage characteristic of CdSe in the dark.

through the negative-resistance region is so rapid that a point-by-point observation of the current-voltage characteristic in this region cannot be made. At the uppermost part of the curve, the negative resistance region ceases because of the resistance limitation provided by the ammeter. Without this resistance limitation, the current goes to such a high level that the sample is destroyed. At the point of highest current, the total voltage is still V_{th} , even though the voltage across the sample has decreased. The difference in voltage appears across the ammeter. If the voltage across the combination is decreased, the current decreases in the noisy fashion shown in the figure. After the current reaches zero, the process may be repeated.

When the CdSe sample is illuminated with light, the threshold voltage is reduced. In Fig. 4, the lowering of the threshold voltage is illustrated for three different light intensities. From Figs. 3 and 4, it may be noted that CdSe is a good insulator before the threshold voltage is reached.

3.1 Experimental Setup

The experimental setup used to measure the threshold voltage of CdSe

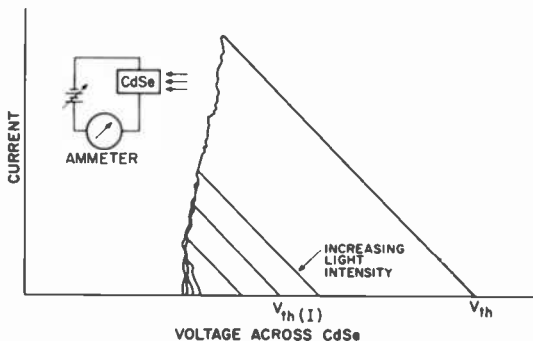


Fig. 4—Current-voltage characteristic of CdSe with light incident.

powder as a function of light intensity and wavelength is illustrated in Fig. 5. The light intensity at the exit slit of the monochromator as a function of wavelength was measured using a calibrated phototube. This equipment was also used to calibrate the transmission of various neutral density filters as a function of wavelength. The voltage across the CdSe sample was measured by subtracting the voltage across terminals B from the total voltage across terminals A. This voltage, A minus B, was recorded as the x -coordinate on an X-Y recorder. The voltage across the B terminals was proportional to the current

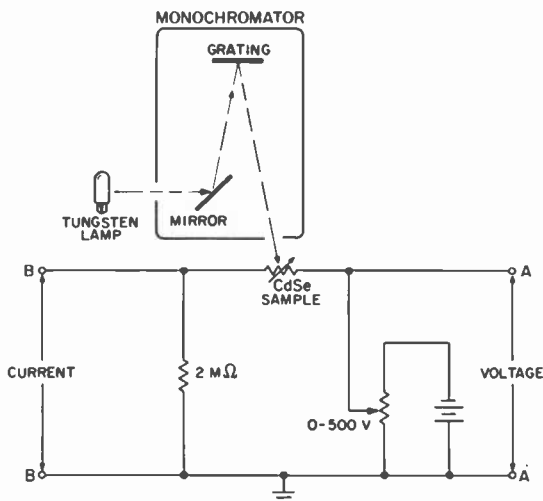


Fig. 5—Experimental setup for measuring the threshold voltage of CdSe powder with light incident on the sample.

through the CdSe, and was recorded as the y -coordinate on the X - Y recorder.

3.2 Samples

The CdSe samples used in the experiments were prepared by stretching a 10-mil copper wire over a piece of glass with 10 strips of transparent, conductive tin oxide coated on the surface. The strips of tin oxide were 0.010-inch wide, separated by 0.040 inch, and were placed perpendicular to the copper wire. In this way, ten samples were made in each setup. The spacing between the wire and the glass was set at 100 μm (0.004 inch), and the copper wire and conductive coating of the glass provided the electrodes for the small amount of CdSe powder dropped between them. The particle size of the CdSe powder was of the order of 50 μm in diameter.

3.3 Experimental Procedure

Measurements of threshold voltage with light incident on the CdSe sample were carried out at 44 different wavelengths between 400 and 1100 nm. The monochromator of Fig. 5 was set at one of these wavelengths, and the light from the exit slit was allowed to fall on the CdSe sample. The sample was positioned so that the light emerging from the exit slit fell where the material made contact with the conductive coating of the glass. The absorption due to the glass and the conductive coating was measured before preparing the samples and was taken into account in determining the incident-light intensity. By placing the various previously calibrated neutral-density filters between the exit slit and the CdSe, the intensity of the light incident on the sample was adjusted so that the voltage at threshold was of the order of 50 volts for all wavelengths. With this light incident on the sample, the voltage across the sample was increased from zero until the threshold was reached. The material passed through the negative resistance region rapidly, then the voltage was returned slowly to zero. This process was repeated five times for each wavelength.

Fig. 6 shows an example of the measurement of $V_{th(I)}$ with light of intensity I incident on the sample. For each of the five measurements, the zero-axis of current on the X - Y recorder was shifted. From Fig. 6, it is observed that, below about 30 volts, no measurable current passes through the sample either before or after breakdown. This was always found to be the case, except under conditions of extremely

high light intensity (room light or direct light from the tungsten source incident on the sample). Under these conditions, the negative resistance disappeared. However, even with the disappearance of negative resistance for high light intensities, 21 volts still had to be applied across the sample before a measurable current would flow. The value of 21 volts (the average of 25 readings) was therefore taken to be the junction bias voltage. In the example of Fig. 6, the value of $V_{th(I)}$ is about 40 volts (total voltage minus junction bias-voltage). This method of determining $V_{th(I)}$ was used in all measurements of the threshold voltage. In a similar manner, the dark threshold voltage V_{th} was found to be 69 volts.

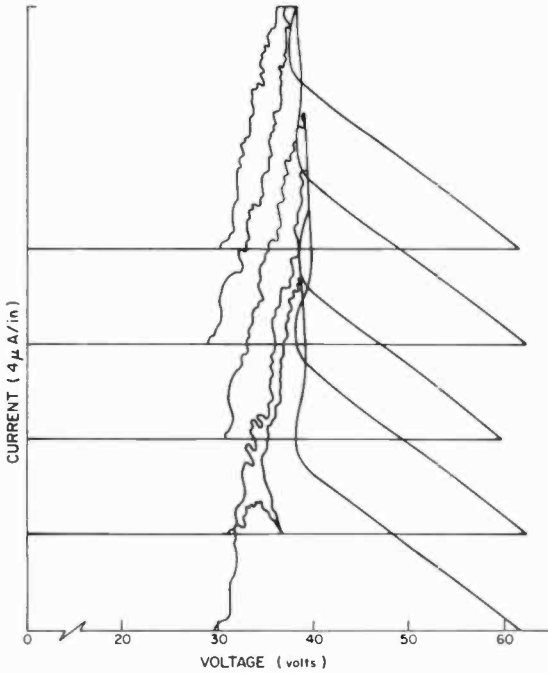


Fig. 6—Measurement of threshold voltage with light incident on the sample ($\lambda = 9000 \text{ \AA}$, $I = 1.06 \times 10^{11} \text{ photons/cm}^2/\text{sec}$).

In summary, measurements of threshold voltage with light incident on the CdSe sample were carried out with light at 44 wavelengths between 400 and 1100 nm. These experimental data were then used to obtain, by means of Eq. [14], the absorption coefficient, relative to the Parsons,⁸ et al, value at 500 nm, as a function of wavelength.

4. Relative Absorption Coefficient from Threshold Measurements

4.1 Results

Fig. 7 shows the relative absorption coefficient values versus wavelength (energy). In the figure, the crosses represent the relative absorption coefficient values determined from threshold voltage meas-

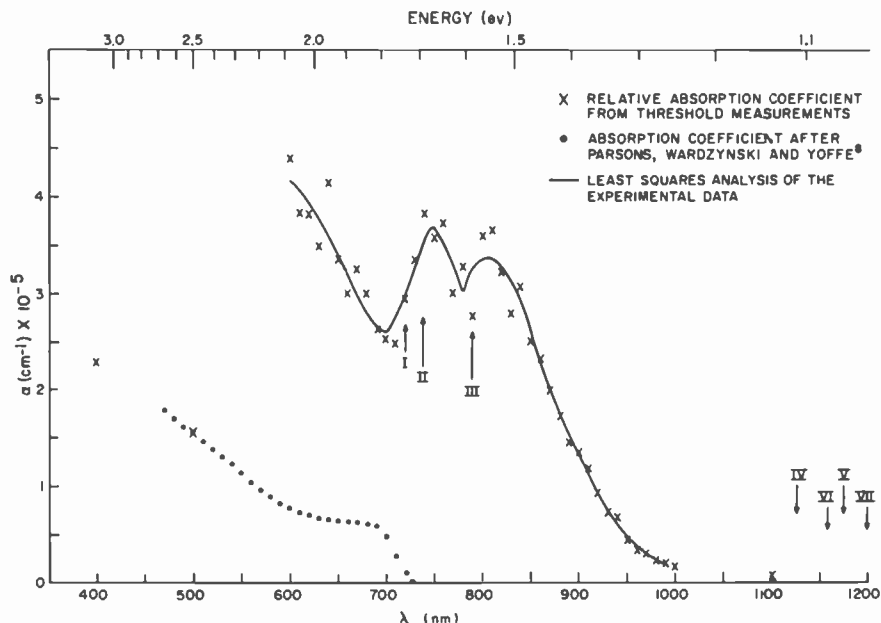


Fig. 7—Relative absorption coefficient versus wavelength.

urements with light incident on the CdSe powder; the dots represent the values of absorption coefficient reported by Parsons, Wardzynski and Yoffe⁸ for pure single-crystal CdSe; the solid line was obtained from a least squares analysis of the experimental data.

4.2 Discussion

Since the relative absorption coefficient values of Fig. 7 were obtained from measurements of the threshold voltage with light at various wavelengths incident on the material, high absorption corresponds to a large reduction in threshold voltage. Also, since the energy level scheme of CdSe is known, the relative absorption is a measure of the effect that absorptions involving imperfection sites have on the

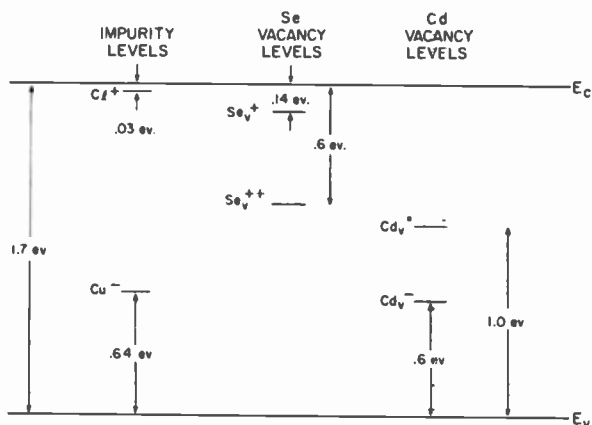


Fig. 8—Bandgap and imperfection levels of CdSe. The Se vacancies and the Cl impurity are depicted as ionized donor levels; the Cd vacancies and the Cu impurity are depicted as ionized acceptor levels.

threshold voltage. Alternately, if the energy level scheme of a material with negative resistance is unknown, the structure in Fig. 7 suggests that information on the locations of imperfections with respect to the bandgap can be obtained by measurements of the type described here.

The bandgap and imperfection levels of CdSe as given by Bube⁹ are illustrated in Fig. 8. The minimum energies required for absorptive transitions, as obtained from Fig. 8, are listed in Table 1. The Roman numerals associated with the arrows in Fig. 7 correspond to the Roman numerals assigned to the absorptive transition limits listed in Table 1.

As shown in Fig. 7, light of wavelength less than 600 nm is not very effective in reducing the threshold voltage. This is so because

Table 1—Absorptive Transitions of CdSe

Transition Designation	Initial Level	Final Level	Minimum Energy Difference (eV)	Wavelength (nm)
I	E_v	E_c	1.70	728
II	E_v	Cl	1.67	741
III	E_v	Se_v	1.56	793
IV	Cd_v^-	E_c	1.10	1125
V	Cu ⁻	E_c	1.06	1167
VI	Cd_v^-	Cl	1.07	1156
VII	Cu ⁻	Cl	1.03	1201

the absorption in this wavelength region is due almost exclusively to transitions between the valence and conduction bands. It is for this reason, of course, that the absorption coefficient is determined relative to the Parsons, et al, value⁸ at 500 nm.

With light of wavelength between 600 and 700 nm incident on the material, the absorption is due to transitions (1) between the valence and conduction bands, (2) between the valence band and Cl^+ levels, and (3) between the valence band and Se_V^+ levels (see Fig. 8). Because of the presence of imperfections, the absorption coefficient in this wavelength region is larger than that reported by Parsons, et al.⁸ As the light wavelength increases from 600 to 700 nm, the absorption decreases, as expected, toward a minimum at the bandgap energy (Arrow I in Fig. 7). At the energy of the bandgap, however, the value of α is rising. This increase in absorption is due to the onset of transitions from Cd_V^- levels to the conduction band. In the absence of these transitions, the absorption would decrease further to Arrow II, which is the absorption limit for valence band to Cl^+ transitions.

After reaching a maximum at about 750 nm, the absorption again decreases, approaching the minimum expected when transitions from the valence band to Se_V^+ levels cease (Arrow III). The second peak in absorption at 800 nm is due to the onset of transitions from Cu^- levels to the conduction band. After this final rise in α , the measured values of relative absorption decrease toward a minimum corresponding to the absorption limits of transitions from Cd_V^- and Cu^- levels to the conduction band (Arrows IV and V) and from Cd_V^- and Cu^- levels to the Cl^+ level (Arrows VI and VII).

It should be noted that all of the absorptive transitions terminate either in the conduction band or in ionized donor levels (traps). Transitions that terminate in the conduction band add extra electrons to the band; transitions that terminate in the ionized donor levels reduce the number of traps, thereby increasing the conductivity. In either case, the threshold voltage is reduced.

5. Conclusions

The following observations can be made about the results of the relative absorption coefficient measurements. Because of imperfections, the absorption of CdSe is extended into the infrared. Also, when absorption of radiation involves imperfection sites, electrons are excited either to the conduction band or to traps, and both kinds of absorption lead to a reduction in threshold voltage and, therefore, to a high relative absorption coefficient. A comparison of the relative

absorption with the known energy-level scheme of the imperfections in CdSe has shown that the experimental data can be interpreted in terms of the known energy levels. Finally, the measurements of relative absorption coefficient provide evidence that the negative resistance observed in CdSe powders conforms to the theory previously described, since the theory predicts a reduction in threshold voltage for absorptions involving imperfection levels.

Acknowledgments

The authors wish to acknowledge the contributions of J. Vollmer, D. J. Woywood, L. J. Krolak, J. J. Rudnick, and F. E. Shashoua of Advanced Technology Laboratories; S. A. Harper and F. J. Hinnenkamp of Electronic Components and Devices; P. Mark of Princeton University; and W. P. Dumke of the IBM Watson Research Center.

References:

- ¹ F. H. Nicoll, "A Hysteresis Effect in Cadmium Selenide and its Use in a Solid-State Image Storage Device," *RCA Rev.*, Vol. 19, p. 77 (1958).
- ² F. J. Hinnenkamp, *Hysteresis in Cadmium Selenide*, M. S. Thesis, Franklin and Marshall College, Lancaster, Pennsylvania, April, 1966.
- ³ R. W. Smith, Private Communication.
- ⁴ L. J. Nicasastro and E. L. Offenbacher, "Negative Resistance in Cadmium Selenide Powder—Comparison of Experiment and Theory," *RCA Rev.*, Vol. 33, p. 357 (1972).
- ⁵ W. P. Dumke, "Theory of Negative Resistance in GaAs pin Diodes," *Bull. Am. Phys. Soc.*, Vol. 9, p. 217 (1964).
- ⁶ W. P. Dumke, "Theory of Negative Resistance in P-I-N Diodes," *Proc. 7th International Conf., Phys. of Semiconductors*, Dunod, Paris (1964); p. 611.
- ⁷ K. Weiser, "Properties of GaAs Diodes with P-P⁻N Structures," *IBM J. Res. Dev.*, Vol. 9, p. 315 (1965).
- ⁸ R. B. Parsons, W. Wardzynski and A. D. Yoffe, "The Optical Properties of Single Crystals of Cadmium Selenide," *Proc. Roy. Soc. London*, Vol. 262A, p. 120 (1961).
- ⁹ R. H. Bube, *Photoconductivity of Solids*, John Wiley and Sons, Inc., New York, London, 1960.

Space-Charge Instabilities in Transferred-Electron Devices*

Barry S. Perlman

RCA Laboratories, Princeton, N. J. 08540

Abstract—This paper is concerned with the absolute and convective instabilities that result from majority carrier transport in a material characterized by a negative differential mobility (NDM). The characteristic space-charge growth can result in the appearance of a stable steady-state negative resistance that can be utilized for microwave amplification.

A small-signal analysis of the space-charge growth mechanism reveals several possible modes of device operation. (In these studies, the cathode nucleated Gunn type domain is not considered. The present analysis examines the steady-state electric field distribution and the resulting effective growth parameter, $\alpha(E, x)$. By means of a graded doping profile, the parameter $\alpha(E, x)$ becomes approximately independent of the spacial coordinate x . As a result, the analysis may be linearized (similar to a uniform electric field condition). A set of perturbation equations are then used to derive a dispersion relation, which is solved explicitly for the characteristic roots associated with the propagation vector. Under the influence of carrier diffusion, the charge carrier waves are found to exhibit two distinct forms of instability. An absolute instability (temporal growth), leading to a stable nonuniform high anode electric field, is capable of being sustained if a critical growth condition is satisfied while the effect of the field dependence of diffusion is limited. Otherwise, the convective (spacial) growth would exist so long as the excitation frequency is below a cutoff value.

* This paper is part of a dissertation submitted in partial fulfillment of the requirement for the Ph.D. degree of Electrophysics, Polytechnic Institute of Brooklyn, New York, N.Y.

1. Introduction

The propagation of space-charge waves within a medium characterized by a negative differential mobility (NDM) can lead to a growth condition that can be used for microwave amplification. In most cases, the material considered for this purpose has been GaAs, which exhibits the transferred-electron effect and sustains a field-controlled transfer of electrons between a high-mobility (000) conduction-band minimum to low-mobility (100) valleys 0.35 eV higher in energy.¹⁻⁶

A combination of theoretical and experimental studies has led to a significant increase in our understanding of the amplification mechanism in these devices. In particular, the work of McCumber and Chynoweth⁷ and Kroemer⁸ was useful in explaining the results of Thim, et al,^{9,10} with specific reference to the attainment of reflection-type amplification from subcritically doped GaAs devices. By utilizing a small-signal linearized theory, with the assumption of a uniform electric field profile, the theory indicates a critical product between the impurity density n_d and the active layer length l . More recent results by Perlman, et al,¹¹⁻¹⁴ and Magarshack and Mircea^{15,16} have clearly revealed the ambiguous nature of the critical $n_d l$ product as previously defined; its effective value is a dynamic function of the electric field distribution and bias voltage, the effective length of material biased above threshold, the level of NDM as effected by the electric field distribution, the circuit impedance, device temperature, contacts properties, diffusion effects, etc. Several of these effects have been considered, often through the use of numerical techniques to solve the nonlinear problem. These results usually lack a sufficient physical interpretation. Most analytical results on the other hand, have been oversimplified, lacking sufficient detail to explain many of the effects observed in practice. The present study is an attempt to unify many of the concepts considered earlier. A combination of numerical and analytical techniques are used to achieve a solution for the static field redistribution as a function of the impurity profile and applied bias voltage and to derive a dispersion relation that incorporates the effects of the field dependence of diffusion.

The effects of diffusion, ignored in most analyses, have been considered with respect to several forms of large-signal device behavior.¹⁷⁻²¹ The influence of diffusion on small-signal space-charge amplification has been restricted to the study of low activity devices (i.e., $n_d \ll (n_d l)_{crit}$) where it could be considered in the form of an approximation.²²⁻²⁷ When diffusion effects are properly accounted for, the charged carrier waves are found to exhibit two distinct forms of

instability; one is convective (spatial growth) and the other is absolute (temporal growth).^{28,29} Guéret³⁰ has considered these forms of instability for a device with ohmic contacts. A criterion is found relating the product of the diffusion constant, the NDM, and the impurity density n_d to a critical condition revealing the "absolute" instability. The factor of length l is not involved in this criterion. Further investigations into the nature of this instability have indicated that it should result in switching from a uniform electric field to a stationary nonuniform high electric field confined to the anode.^{31,32}

Once the criterion for an absolute instability is satisfied, the group velocity associated with the forward space-charge wave becomes infinite at $\omega = 0$. This effect can be shown to result in the appearance of a *static* negative resistance coupled with a *finite* static reactance.³³ The latter is evidence of the unstable nature of the "instability." Both Dohler³⁴ and Hauge³⁵ have considered the possibility of a static negative resistance by considering the effects of a nonphysical model for the field dependence of diffusion, but they do not note that the device they were dealing with no longer supports the convective instability. Their results are in agreement with Thim³¹ in that a stable nonuniform electric field would be supported. It will be shown here, that once the field dependence of diffusion is properly accounted for, it not only has a dissipative effect on space-charge growth, but also tends to eliminate the possibility of the absolute instability.

In the following discussion, we shall develop a small-signal steady-state theory for wave propagation in a one-dimensional device model that includes: (1) the effects of the field dependence of diffusion, (2) the relationship between the forward and backward waves, and (3) the appearance of and criterion for both the absolute and convective instabilities. The analysis assumes that the only charge carriers are electrons, with the effects of energy and momentum relaxation being negligible. The time required for intervalley transfer is assumed to be much less than the period of the applied rf wave and may therefore be taken to be equal to zero. Consequently, the average velocity may be assumed to be an instantaneous function of the field.

A preliminary investigation of the stationary solution for the electric field distributed throughout the active n-layer is discussed in Section 2. The influence of specific impurity profiles is considered with the objective of achieving a uniform growth condition. In Section 3 a set of linearized equations are introduced representing an ac perturbation of the static parameters. A dispersion relation is developed and solved explicitly, revealing the occurrence of the two distinct forms of instability, absolute and convective. Consideration

is given to the dispersive phase and group velocities associated with the space-charge waves. It is shown that in addition to causing an infinite group velocity at $\omega = 0$ for the absolute instability, diffusion retards forward-wave growth. The latter effect is particularly significant for the convective instability in the limit of low $n_d l$ products and high frequencies.^{25, 26}

2. Stationary Solution

When a constant dc voltage bias is applied across an n⁺-n-n⁺ GaAs device, the redistribution of charge associated with the transferred-electron effect will not necessarily support a uniform electric field throughout the n-layer. The growth of space charge within a region of fields where the material is characterized by a negative differential mobility (NDM) will usually result in a high anode field. When the sample length is sufficiently long, the spatial growth or domain formation is restricted to a region of discontinuity, presumably near the cathode. The resulting domain propagates giving rise to Gunn-type current oscillations at frequencies related to the transit time of the dipole layer. Conversely, when the sample length is short, or equivalently when the product of length and the doping density is less than some critical value consistent with the NDM associated with the device bias, a stationary electric-field distribution is obtained.⁷ In this latter mode, the device can support a stable negative resistance. The discussion that follows is concerned with this mode of device operation.

The dynamics associated with space-charge growth are strongly influenced by the nature of the stationary electric-field distribution. Since the space-charge growth is restricted to the region of the n-layer length characterized by an electric field that sustains an NDM, the frequency response of the device impedance will be affected by the nonuniformity of the field. A region of low activity, such as that near the anode in a uniformly doped n-type sample, may be shown to contribute little growth, due to a saturated velocity condition, while the region near the cathode is essentially dissipative due to below-threshold fields. The effective length of the remaining active region will support a geometrical resonance resulting in *bands* of negative resistance at frequencies near the transit-time frequency and its harmonics. This length can be significantly less than the physical length in the uniformly doped case, whereas, it can approach the physical length in a sample with a positively graded doping profile.

The total current density J flowing in one dimension comprises

a particle current J_p and a displacement current $\epsilon(\partial E/\partial t)$ such that

$$J = J_p + \epsilon \frac{\partial E}{\partial t}, \quad [1]$$

where the particle current J_p is the sum of convective and diffusion currents

$$J_p = nev(E) - \frac{e\partial}{\partial x} [D(E)n]. \quad [2]$$

Here n is the free carrier density, e is the magnitude of the electronic charge, $v(E)$ is the field dependent electron drift velocity, ϵ is the dielectric constant, E is the electric field, and $D(E)$ is the diffusion constant. The sign conventions used in Eqs. [1] and [2] and for all remaining equations in this text are described in Fig. (1).

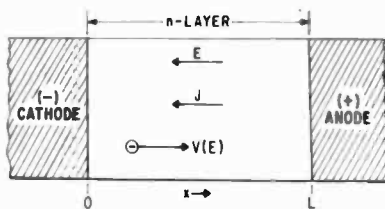


Fig. 1—Schematic cross section of a transferred-electron device.

The total current J is independent of position ($\partial J/\partial x = 0$) with continuity of charge flow given by

$$\frac{\partial}{\partial t} (en) + \frac{\partial J_p}{\partial x} = 0, \quad [3]$$

while the space charge is related to

$$\epsilon \frac{\partial E}{\partial x} = e[n(x) - n_d(x)], \quad [4]$$

where $n_d(x)$ represents the spacial profile associated with the donor density.

The total voltage across the device is given by

$$V = \int_0^L E(x) dx, \quad [5]$$

where L represents the physical length of the n layer. The voltage drop across the heavily doped n^+ regions has been assumed to be negligible.

For the purpose of evaluating the stationary solution for the electric field ($\partial/\partial t = 0$) we shall neglect diffusion, i.e., $D(E) = 0$. Since the current is assumed to be only convective, a normalized static electric field \bar{E}_0 may be described by

$$\frac{\partial \bar{E}_0}{\partial x} = \left[\frac{\bar{J}}{\bar{v}(E)} - \bar{n}_d(\bar{x}) \right] \quad [6]$$

with

$$\begin{aligned} \bar{E}_0 &= \frac{E_0}{E_m}; E_m = \text{threshold electric field for } v(E) = v_m \\ \bar{v}(E) &= \frac{v(E)}{v_m}; v_m = \text{peak threshold velocity} \\ \bar{x} &= \frac{x}{x_m}; x_m = \frac{\epsilon E_m}{en_d(0)}; n_d(0) = \text{donor density at } x = 0 \quad [7] \\ \bar{J} &= \frac{J}{J_m}; J_m = en_d(0)v_m \\ \bar{n}_d(\bar{x}) &= \frac{n_d(\bar{x})}{n_d(0)}. \end{aligned}$$

The use of normalized parameters in Eq. [6] is convenient in plotting solutions for $E[x]$.

An appropriate model for $v(E)$ has been taken from the work of Ruch and Fawcett³⁶ for $T = 300^\circ\text{K}$ and fitted to the analytic expression given in Eq. [8] (this model is qualitatively consistent with several other results³⁷⁻⁴⁰):

$$v(\bar{E}) = \frac{1.435 E + .275 (\bar{E})^{3.3}}{1 + .71 (\bar{E})^{3.3}}, \quad [8]$$

with the normalization constants $E_m = 3.4257$ kV/cm and $v_m = 2.063 \times 10^7$ cm/sec. A plot of Eq. [8] is shown in Fig. 2.

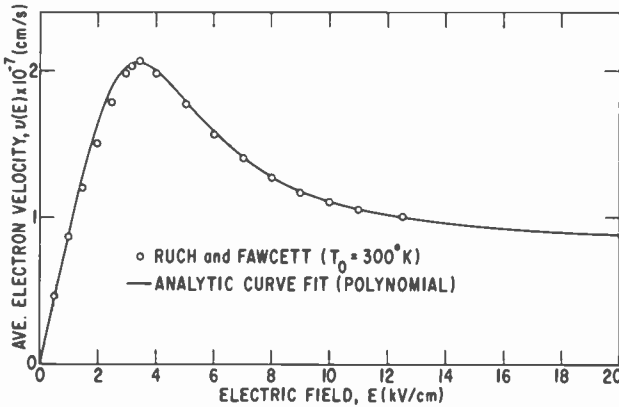


Fig. 2—Average electron velocity $v(E)$ as a function of the electric field. The polynomial curve fit is taken with respect to data from Ruch and Fawcett.³⁶

Solutions for $\bar{E}_o(x)$ have been computed numerically using a Runge-Kutta integration procedure for both a uniformly doped sample and a linearly graded one. An initial value for $E(0) = 0$ was chosen to represent a virtual cathode at $\bar{x} = 0$. In each case, all of the parameters have been normalized in order to generalize the results. The coordinate $x = \bar{x} x_m$ is readily found for a particular doping density $n_d(0)$ using

$$x \approx 2.38 \times 10^{10} \frac{\bar{x}}{n_d(0)} \quad [9]$$

2.1 Uniform Doping

A common device model, often considered in the literature, is one where the n-layer doping is uniform with $n_d(x) = n_d(0)$. A plot of the electric field for this case is shown in Fig. 3 where the normalized current $\bar{J} = J_o/J_m$ has been used as a parameter.

The substantial nonlinearity of the electric-field distribution is due

to a lack of space-charge neutrality throughout the n-layer. If the condition for charge neutrality were maintained, the maximum current that could be passed through the bulk would be J_m or $\bar{J} = 1$. So long as $\bar{J} \leq 1$, the electric field can not exceed its threshold value E_m .

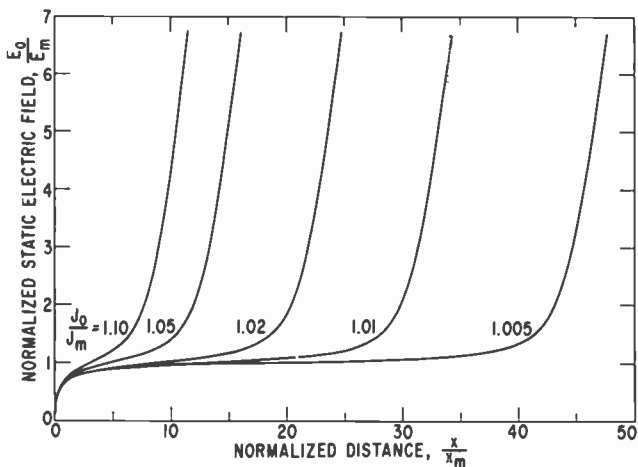


Fig. 3—Normalized static electric field as a function of the normalized distance from the (virtual) cathode. The normalized current density \bar{J} is used as a parameter.

On the other hand, by increasing the current to a value just slightly greater than J_m , the electric field increases rapidly to a value significantly larger than its threshold value. Since the area under each curve is equal to the applied voltage bias, it can be readily seen that a substantial increase in voltage result in only an insignificant increase in current. This saturated current condition is referred to as being space-charge limited. One obvious feature of these curves is that the static current is a monotonically increasing function of the applied voltage. Thus in this diffusion-free case, the device is characterized by a positive static resistance.

A plot of the normalized voltage, $\bar{V} = V/V_m$ is given in Fig. 4, where V is the actual voltage and $V_m = E_m L$, with L being the total length of the n-layer. For each combination of length, doping density, and applied voltage, a corresponding value of \bar{J} may be found (i.e., although \bar{J} was used as an independent integration parameter, the applied voltage is physically the independent variable).

Additional insight into the space-charge-growth mechanism within the active n-layer may be achieved by studying the parameter

$$\alpha(E, X) = \frac{J_0}{\epsilon v^2(E)} \frac{\partial v(E)}{\partial E}$$

This growth parameter will be shown to correspond to the real part of a complex wave-propagation vector for the general case where $dE_0/dx \neq 0$ and in the absence of diffusion. In the case where $dE_0/dx = 0$, $\alpha = \omega_p/v(E)$ where $\omega_p = (n_d e/\epsilon)(\partial v(E)/\partial E)$ is the dielectric

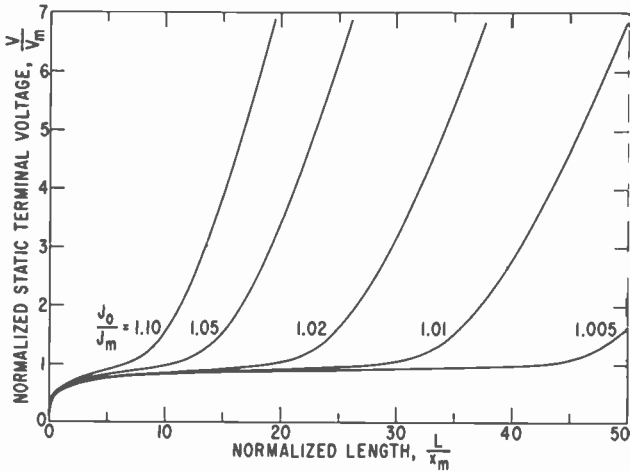


Fig. 4—Normalized static terminal voltage as a function of the normalized device length. The normalized current density \bar{J} is used as a parameter.

relaxation frequency. When the differential mobility $\mu_1 = \partial v(E)/\partial E$ is negative as is the case for fields above the threshold value E_m , α becomes negative, causing a nearly exponential growth of space charge. The stability of the crystal will be shown to be directly affected by both the magnitude of α and the actual length over which a negative value is sustained.

The spatial distribution for $\alpha(x)$ is readily found by computing its value using the parameters $v(E)$ and $\partial v(E)/\partial E$ as derived from Eq. [8] and using the actual values for $E(x)$ (Fig. 3). A plot of the normalized parameter $\bar{\alpha}(x) = \alpha(x) x_m$ is shown in Fig. 5. For current densities that are greater than threshold (i.e., $J/J_m > 1$), a finite region of length l exists where $\alpha < 0$. This region begins near the anode and moves towards the cathode as the current density is increased. Both the actual magnitude of $\alpha = \bar{\alpha}/x_m$ and the physical extent of this region of activity are directly dependent upon the doping density $n_d(0)$ and can be found using Eq. [9].

Two additional regions are observed, one near the cathode, where $\alpha > 0$, and one with $\alpha = 0$ beginning at the anode and extending towards the region of negative activity. The cathode region, which is reduced in extent as the current density is increased, is the result of below-threshold fields near the cathode contact, whereas the anode region ($\alpha = 0$) is caused by a saturated velocity condition due to excessively high anode fields.

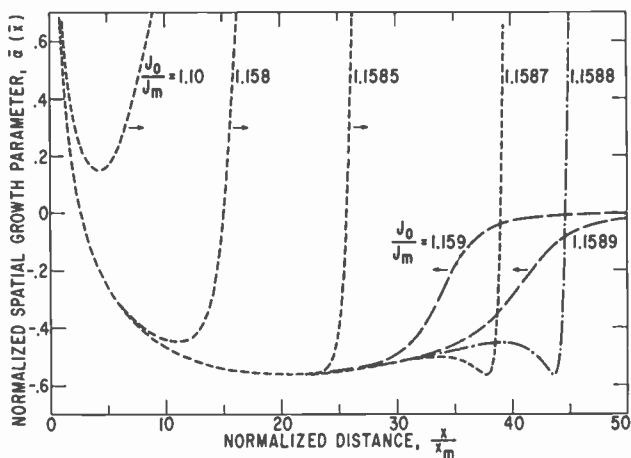


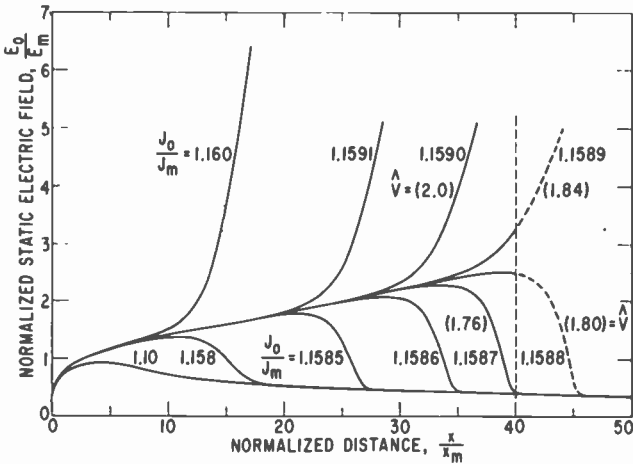
Fig. 5—Normalized growth parameter $\bar{\alpha}(\bar{x})$ as a function of the normalized distance from the (virtual) cathode for a uniformly doped device ($n_d(x) = n_d(0)$).

From the point of view of an actual device, the physical length of the n-layer should be designed to minimize the extent of the saturated anode region, since it only contributes to an unnecessary phase shift while absorbing voltage to support the high anode field.

2.2 Graded Doping

An examination of Eq. [6] reveals an inverse dependance of the derivative of the electric field upon the function $\bar{v}(\bar{E})$ that may be compensated by a suitable donor density profile $\bar{n}_d(\bar{x})$. By specifying a function $\bar{n}_d(\bar{x})$ that increases with \bar{x} , while the velocity is decreasing for electric fields above threshold, a constant value of $d\bar{E}_o/d\bar{x}$ may be achieved. An important objective is to provide a growth factor $\bar{\alpha}(\bar{x})$ that remains essentially constant and equal to its maximum value throughout the n-layer.

A simple but effective doping profile is a linearly graded one. An estimate of the required slope may be formed by noting that the normalized velocity approaches a saturated value of 0.5 for a high anode field. The slope of the electric field remains positive so long as the background density $\bar{n}_d(\bar{x})$ remains less than $\bar{J}/\bar{v}(\bar{E})$. A desirable condition is to let the slope $d\bar{E}_o/d\bar{x} \rightarrow 0$ near the anode by specifying an anode donor density that compensates the saturated velocity condition. The required anode doping is therefore nearly twice its value at the cathode.



sity, resulting from an increase in bias voltage, produces a rising anode field condition similar to that observed in the uniformly doped case.

The significance of the use of the graded doping profile is revealed in the plot of $\bar{\alpha}(\bar{x})$ shown in Fig. 7. As the current density is increased,

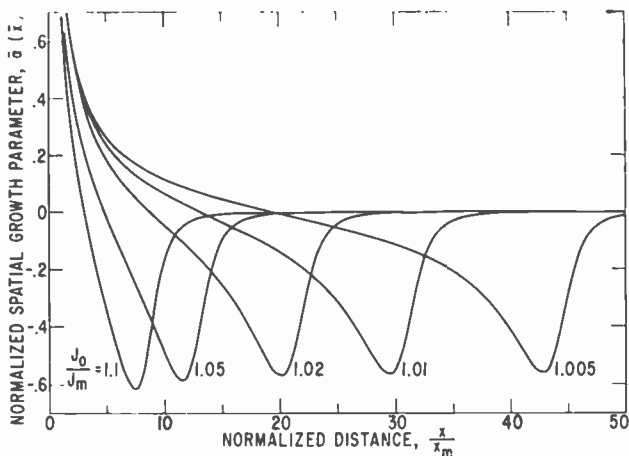


Fig. 7—Normalized growth parameter $\bar{\alpha}(\bar{x})$ as a function of the normalized distance from the (virtual) cathode for a device with a normalized length of 40 and 2:1 graded doping profile. Arrows indicate the progressive variation in $\bar{\alpha}(\bar{x})$ as the bias voltage is increased.

an active region of length l , with $\alpha < 0$, is swept out, extending from near the cathode right to the anode. The value of $\bar{\alpha}(\bar{x})$ remains essentially constant over more than 75% of the physical length of the n-layer. (i.e., $l \geq 0.75L$). Regardless of the current through the sample, the characteristic of the cathode region remains approximately the same, in direct contrast with the uniform case (Fig. 5). Once the applied voltage exceeds the value corresponding to providing activity up through the anode, the behavior begins to resemble the uniformly doped case. Further increases in voltage reduces the active area, moving it closer towards the cathode. The fact that there is a voltage that results in filling the sample with activity is significant in that this particular type of device will produce a larger space-charge growth than that associated with the uniformly doped case, thereby supporting a larger negative resistance and providing a lower transit-time-limited frequency of operation. This effect occurs because the transit length l through the active material approaches the physical length L ,

which is in direct contrast with the uniformly doped case. At the same time, this device will be more likely to be unstable⁴¹ due to the enhancement of the αl product, unless the $n_d(0)l$ product is less than some critical value.⁷

From the point of view of regulating the NDM and, hence, the growth parameter $\alpha(x)$, it is often desirable to operate the device such that the average electric field is considerably above its threshold value E_m . This is particularly true with regard to stabilizing those device that are supercritically doped,^{11,14-16,42} where the average value of $n_d l \geq 10^{12}$ cm⁻². By introducing a doping notch (decrease) at the cathode, followed by a positively graded doping density, the device will sustain a nearly uniform electric field at a value determined by the properties of the notch.⁴³ This type of device will provide a reduced level of activity, consistent with remaining stable, at a bias voltage in excess of twice its threshold value.

3. The AC Disturbance and Device Instabilities

A stream of electrons flowing through an infinitely long n-type semiconductor will support ac disturbances in the form of two traveling waves in addition to a nondispersive uniform mode. One of the longitudinal waves propagates with the electron stream, while the other moves in a backward direction. The existence of this backward wave is the result of diffusion and is normally neglected in most analysis, since in the limit of small diffusion, it is evanescent and decays within a short distance (of the order of a few Debye lengths). On the other hand, when the activity for a device exhibiting an NDM is sufficiently high, the coupling of this backward wave to the growing forward wave can result in a significant influence on both the device impedance and its stability.

The growing space-charge wave, in addition to the uniform mode, is associated with a convective instability that provides the basis of the negative-resistance behavior for the transferred-electron device. In a finite sample, the overall effect is achieved by mixing these natural modes in a manner consistent with the boundary conditions. The growing forward space-charge wave can be shown to be strongly influenced by the degree of carrier injection at the cathode, while the diffusion-controlled backward wave is affected by the electrical properties at the anode.³³ When the effects of diffusion are considered, the device is conditionally able to exhibit an absolute instability with the appearance of space-charge waves that are characterized by an infinite group velocity.

3.1 Small Signal AC Perturbation Analysis

In order to study the dynamic properties of the active device, we shall examine the effect of small perturbations on the equations of motion. Once again, the spatial analysis will be restricted to one dimension. The static terms shall be denoted with a subscript o while the small-signal time-varying terms, varying as $e^{j\omega t}$, will incorporate the subscript 1. The following set of first-order equations defines the perturbed variables:

$$E(x,t) = E_o(x) + E_1(x,t) \quad [10]$$

$$n(x,t) = n_o(x) + n_1(x,t) \quad [11]$$

$$v(E) = v_o(E_o) + v'(E_o)E_1(x,t) \quad [12]$$

$$D(E) = D_o(E_o) + D'(E_o)E_1(x,t) \quad [13]$$

where $E_1 \ll E_o$ and $n_1 \ll n_o$. The use of the parentheses to indicate dependence on x and/or t will not necessarily be continued in the following derivations. Using Eq. [5],

$$n_o = n_d + \frac{\epsilon}{e} \frac{\partial E_o}{\partial x} \quad [14]$$

$$n_1 = \frac{\epsilon}{e} \frac{\partial E_1}{\partial x} \quad [15]$$

and

$$v' = \left. \frac{\partial v}{\partial E} \right|_{E=E_o} \quad [16]$$

$$D' = \left. \frac{\partial D}{\partial E} \right|_{E=E_o} \quad [17]$$

Substituting these perturbed variables into the current equation (Eq. [1]) and neglecting second- and higher-order terms in order to linearize the analysis, we find,

$$J_o = en_o v_o - J_{D_o} \quad [18]$$

$$J_1 = \epsilon v_o \left[\alpha + j\beta + \frac{\partial}{\partial x} \right] E_1 - J_{D1} \quad [19]$$

with*

$$\alpha = \left(\frac{n_o e}{\epsilon} \right) \frac{v'}{v_o} = \frac{\omega_D}{v_o} \quad [20]$$

$$\beta = \frac{\omega}{v_o} \quad [21]$$

$$J_{D_o} = e \frac{\partial}{\partial x} (D_o n_o) \quad [22]$$

$$J_{D1} = e \frac{\partial}{\partial x} (n_1 (D_o + D'E_1) + n_o D'). \quad [23]$$

The static diffusion current J_{D_o} has been included here for completeness. As in the previous section, the influence of J_{D_o} on the total current is assumed to be sufficiently small, compared with the conduction current, to justify neglecting it in the derivation of the static device solutions. An expansion of J_{D_o} indicates that it is a strong function of both the slope of the donor density $n_d(x)$ and the electric-field profile $E_o(x)$:

$$\begin{aligned} J_{D_o} &\approx e D_o \frac{\partial n_o}{\partial x} + e D' n_o \frac{e}{\epsilon} \left[(n_o - n_d) \right] \\ &= D_o \left[e \frac{\partial n_d}{\partial x} + \epsilon \frac{\partial^2 E_o}{\partial x} \right] + D' \frac{\partial E_o}{\partial x} \left[e n_d + \epsilon \frac{\partial E_o}{\partial x} \right] \end{aligned} \quad [24]$$

So long as the donor density and electric-field profiles are not characterized by excessive slopes, with the exception of regions near the contacts, the contribution of J_{D_o} will remain relatively small. On the other hand, the significance of the ac component of current due

* It should be noted here that for the case of a finite diffusion coefficient, the solutions to Eq. [19], as written, are valid for the condition of constant coefficients. As pointed out earlier, this condition is well approximated for the case of a nonuniform doping profile (e.g., Fig. 7).

to diffusion J_{D1} will be shown under certain circumstances to substantially alter the stability of the active device. The current J_{D1} can be expanded as,

$$J_{D1} = \epsilon v_o \left[\gamma_o \frac{\partial^2 E_1}{\partial x^2} + \alpha \gamma' \left[\frac{\partial(\ln(n_o))}{\partial x} E_1 + \left(2 - \frac{n_d}{n_o} \right) \frac{\partial E_1}{\partial x} \right] \right] \quad [25]$$

with

$$\gamma_o = \frac{D_o}{v_o} \quad [26]$$

$$\gamma' = \frac{D'}{v'} \quad [27]$$

An estimate of the field dependence of diffusion is found by assuming that the energy distribution of carriers at each instant is described by an average carrier temperature⁷ T_c . By using a thermal energy relaxation time τ_T in conjunction with a solution of the energy transport equation in thermal equilibrium (ignoring spacial effects) and using the Einstein relation $D(E) = \mu(E)(KT_c/e)$ (K is Boltzmann's constant) to relate the diffusion constant $D(E)$ to the average mobility, $\mu(E) = v(E)/E$, we find

$$D(E) \approx \frac{v(E)}{E} \left[\frac{1}{40} + \frac{2}{3} \tau_T v(E) E \right]. \quad [28]$$

Plots of both $D(E)$ and γ' are shown in Fig. 8 where we have used a value of $\tau_T = 10^{12}$ sec. This result is in good quantitative agreement with the more detailed two-temperature model and theoretical predictions of Butcher and Fawcett³⁷ and the Monte Carlo calculations of Fawcett and Rees.⁴⁴ The experimental results of Ruch and Kino³⁹ are qualitatively similar but indicate a higher diffusion rate. Thus the simplified model for $D(E)$ represented by Eq. [28] is adequate for the purpose of estimating the quantities γ_o and γ' .

3.2 The Dispersion Equation and the AC Electric Field

A solution for the ac electric field is based on a mix of wave type solutions varying as $\exp j(\omega t - kx)$, with k corresponding to a complex propagation vector. In the finite semiconductor, the mix of these

natural modes is established in such a way as to satisfy the pertinent boundary conditions. By neglecting all of Maxwell's equations except that of Poisson, we have limited this discussion to slow traveling waves ($\omega/k \ll c$).

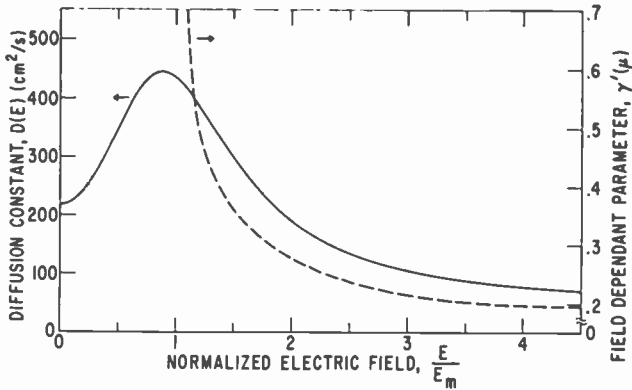


Fig. 8—Field-dependent diffusion constant $D(E)$ and normalized parameter γ' as functions of the electric field.

Substitution of the space-charge component of electric field E_{sc} , $\exp(-jkx)$ into Eq. [19] yields the dispersion relation

$$\alpha_e + j\beta - j\zeta_e k + \gamma_o k^2 = 0, \quad [29]$$

where

$$\alpha_e = \alpha \left[1 - \gamma' \frac{\partial(\ln(n_o))}{\partial x} \right] \quad [30]$$

$$\zeta_e = 1 - \alpha\gamma' \left(2 - \frac{n_d}{n_o} \right). \quad [31]$$

For n-GaAs with electric fields varying from 4 to 10 kV/cm, the diffusion constant is estimated (Fig. 8) to decrease from approximately 400 cm²/sec to near 100 cm²/sec (e.g., $D' \geq 0.05$ cm³/V-sec), and the carrier velocity has an average value near 1.4×10^7 cm/sec with a maximum differential mobility of about -2500 cm²/V-sec. At a field near $2.0 E_m$ the value for γ_o can be approximated to be equal to $0.2 \mu\text{m}$, while the corresponding value for γ' can be estimated to be near

0.28 μm . The parameter γ' has a value near 0.2 μm for fields in excess of $2.5 E_m$. For donor densities less than $n_d = 5 \times 10^{14} \text{ cm}^{-3}$, α is less than $1 \times 10^4 \text{ cm}^{-1}$ and $\zeta_e \approx 1$. On the other hand, if the active material is either more heavily doped ($n_d > 5 \times 10^{14} \text{ cm}^{-3}$), with a corresponding increase in the negative value of α , or is biased at fields in excess of twice threshold, thereby reducing the NDM (v') with a resulting increase in γ' , the result would be $\zeta_e > 1$ due to the influence of the field dependence of diffusion. So long as the static electron density n_o is reasonably uniform and without an excessive slope due to a nonuniform electric field, the value for $\alpha_e \approx \alpha$. The influence of γ' can become particularly significant in reducing α_e in those cases where the electric field profile is substantially nonuniform. This effect is characteristic of the region near the cathode and anode contacts where the value of n_o is increased. However, the influence of these regions is only significant when the active layer thickness becomes comparable to their extent.

3.3 The Uniform Solution

Three waves in all must be mixed in order to satisfy the appropriate boundary conditions. In addition to the two complex roots for k , which will be found by solving Eq. [29], there is a uniform mode (forced solution) which obeys the simple dispersion relation,

$$k_u = 0. \quad [32]$$

This uniform mode, having no variation with x , is in direct response to the applied voltage. The resulting total electric field can be expressed by

$$E_1(x,t) = \{E_u + E_{sc} \exp(-jkx)\} \exp(j\omega t), \quad [33]$$

where

$$E_u = \frac{J_1}{\epsilon v_o (\alpha_e + j\beta)}. \quad [34]$$

E_u is the amplitude of the uniform mode, E_{sc} is the amplitude of the space-charge mode, and the boundary conditions serve to specify the relationship between E_u and E_{sc} . It is interesting to note that although the space-charge term in Eq. [33] can provide substantial traveling-wave growth when the imaginary part of k is positive, it is not essential in producing a negative resistance in a finite device. In fact,

if it were not for the space-charge wave, the device impedance would be characterized by a static negative resistance. This hypothetical situation may be shown by integrating the uniform solution, Eq. [34]. In order to derive the series equivalent uniform impedance Z_u , it is assumed that the growth parameter α_e and phase parameter β are both constants,

$$Z_u = \frac{1}{C_o v_o} \left[\frac{\alpha_e - j\beta}{\alpha_e^2 + \beta^2} \right], \quad [35]$$

or more simply, the physically correct uniform admittance Y_u ,

$$Y_u = C_o [\omega_{De} + j\omega], \quad [36]$$

where

$$C_o = \frac{\epsilon A}{l} = \text{static bulk capacitance}$$

$$\omega_{De} = \alpha_e v_o = \text{effective negative dielectric relaxation frequency}^{37}$$

$$A = \text{cross sectional area of device}$$

$$l = \text{length of active n-region}$$

The real part of Z_u (or Y_u) would remain negative for all frequencies so long as $\alpha_e < 0$. However, since this uniform mode alone cannot satisfy the boundary conditions, we must consider the influence of the space-charge wave. The finite wavelength and growth associated with the space-charge disturbance in a material with an NDM can be shown to cause geometrical resonances resulting in a periodic positive-to-negative variation of the real part of the impedance of the finite system, whereas the uniform mode produces no such resonances. Although either mode is capable of supporting a two-terminal negative resistance, the usually dominant space-charge effect may be shown^{7,33} to cause band-limiting behavior. We can therefore conclude that a broad-band amplifier must be dominated by the uniform disturbance. Furthermore, the substitution of the total electric field (Eq. [33]) into Eq. [19] would reveal that all of the time-varying current J_1 is carried by the uniform disturbance. This latter condition is consistent with the complementary solutions for the space-charge waves associated with the dispersion relation Eq. [29]. So long as the field E_{sc} is finite, the space-charge wave carries no current. Thus, only the uniform mode is essential. This property of these devices has been considered with respect to the use of a non-ohmic cathode contact in order to effect a means to control the space-charge growth and thereby increase the available $-R$ bandwidth.^{33,45}

3.4 Complex Roots of the Dispersion Equation (Approximate Solution)

The dispersion relation (Eq. [29]) may be solved explicitly for a pair of complex roots,

$$k = j \frac{\zeta_c}{2\gamma_o} \left[1 \pm \left(1 + \frac{4\gamma_o(\alpha_e + j\beta)}{\zeta_e^2} \right)^{1/2} \right]. \quad [38]$$

A preliminary qualitative analysis of the significance of these roots can be obtained by neglecting the effects of field-dependent diffusion (i.e., $\alpha_e \approx \alpha$) and expanding Eq. [38] in the limit of low activity and low frequencies (i.e. $\alpha\gamma_o/\zeta_e^2 \ll 1$ and $\beta\gamma_o/\zeta_e^2 \ll 1$; for a device with $n_o \approx 10^{14} \text{ cm}^{-3}$, $\alpha \approx .2 \times 10^4 \text{ cm}^{-1}$, $\alpha\gamma_o \approx .04$, and $\zeta_e \approx 1$). The frequency approximation is valid for frequencies up to 10 GHz. The two simple solutions are

$$k_f \approx \beta(1 - 2\alpha\gamma_o) - j[\alpha - \gamma_o(\alpha^2 - \beta^2)] \quad [39]$$

$$k_b \approx -\beta(1 - 2\alpha\gamma_o) + j \left[\frac{1}{\gamma_o} + \alpha - \gamma_o(\alpha^2 - \beta^2) \right]. \quad [40]$$

In the derivations of these solutions, we have tacitly assumed that α and the drift velocity v_o are both constants. This assumption is justified following the discussion in Section 2.2.

An examination of these simplified equations reveals that the propagation vector associated with the forward wave k_f and that for the backward wave k_b are characterized by the same phase constant, $\beta(1 - 2\alpha\gamma_o)$. The corresponding approximation for the phase velocity v_p is given by

$$v_p = \frac{v_o}{1 - 2\alpha\gamma_o} = f\lambda \quad [41]$$

where λ the wavelength of the space-charge wave and f the signal frequency, i.e., $f = \omega/2\pi$. Each wave travels with the same group and phase velocity which become equal to the carrier drift velocity in the limit of zero diffusion, i.e., $\gamma_o \rightarrow 0$.

Although the preceding derivation is based upon the condition $\alpha\gamma_o \ll 1$, one important physical implication for the general case is evident. As $\alpha\gamma_o$ increases, with $\alpha < 0$, the phase velocity is found to *decrease*. This effect may be shown to decrease the fundamental

frequency band over which the device sustains a negative resistance as the result of an increase in the transit time of the space-charge wave.

An examination of the propagation constant k_b associated with the backward wave reveals that this wave is evanescent. The existence of this wave is supported by the mechanism of carrier diffusion corresponding to a finite value for $1/\gamma_0$, with its decay, primarily caused by the same factor (i.e., $1/\gamma_0 \approx 5 \times 10^4 \text{ cm}^{-1}$). The backward wave decays in just several fractions of a wavelength. Increasing the signal frequency also contributes to an increase in the attenuation of this reverse wave; on the other hand, there is a small compensating effect due to α through the parameter $\alpha(1 - \alpha\gamma_0)$.

3.5 Diffusion-Limited Space-Charge Growth

For the forward traveling wave to grow in space, the imaginary part of k_f must be greater than zero, a condition that requires the activity parameter α (Eq. [20]) to be less than zero. As demonstrated in Section 2, this condition is met for fields greater than a threshold value E_m , with the value of α remaining essentially constant for the condition where the donor density profile was graded with a positive slope of approximately 2 between cathode and anode.

The electrical behavior of the cathode contact, a region of non-uniform electric field, can affect the space-charge growth. In addition, the value of α must be sufficiently large to overcome the damping effect of diffusion. The latter condition is approximately satisfied when $\alpha + \gamma_0\beta^2 < 0$ (Eq. [39]) or, for space-charge waves with wavelengths larger than a critical wavelength λ_c (i.e., $\beta = 2\pi/\lambda$), where

$$\lambda_c = 2\pi \left(\frac{\gamma_0}{|\alpha|} \right)^{1/2}. \quad [42]$$

A similar characteristic length L_D , known as the Debye length, is associated with the random electronic motion of the charge carriers. Any local disturbances are attenuated in the characteristic distance L_D ,

$$L_D = \frac{1}{2\pi} \lambda_c. \quad [43]$$

For values of $-\alpha$ ranging from 10^3 to near $2 \times 10^4 \text{ cm}^{-1}$, corresponding to donor densities from about 5×10^{13} to 10^{15} cm^{-3} , the critical length λ_c varies from near 10 down to $2 \mu\text{m}$. The corresponding

cutoff frequency, $f_c = v_p/\lambda_c$, would be near 15 GHz for the very lightly doped case ($\lambda_c \approx 10 \mu\text{m}$), increasing to 70 GHz with the increase in doping ($\lambda_c = 2 \mu\text{m}$). In actual devices operating at relatively high ambient temperatures, at fields close to threshold or near velocity saturation, the NDM and correspondingly α are both reduced, thereby increasing λ_c . This practical effect would correspondingly reduce the cutoff frequency, above which the negative resistance would only be supported by the uniform mode.

3.6 Charge Carrier Waves (Exact Analysis)

A rigorous analysis of the dispersive effect of diffusion requires a closed-form solution for the roots of the complementary equation, Eq. [29]. The complete expressions for these complex roots may be found from Eq. [38] to be

$$k_f = \frac{1}{2\gamma_o} [d + j(\zeta_o - c)] \quad [44]$$

$$k_b = \frac{1}{2\gamma_o} [-d + j(\zeta_o + c)]. \quad [45]$$

The identity $c + jd = (a + jb)^{1/2}$ has been used with

$$a = \zeta_o^2 + 4\gamma_o\alpha_o \quad [46]$$

$$b = 4\gamma_o\beta \quad [47]$$

$$c = \frac{b}{2d} = \frac{1}{\sqrt{2}} (a + \sqrt{a^2 + b^2})^{1/2} \quad [48]$$

$$d = \frac{1}{\sqrt{2}} (-a + \sqrt{a^2 + b^2})^{1/2} \quad [49]$$

As before, the roots k_f and k_b correspond to the propagation vectors associated with a potentially growing forward wave and an evanescent backward wave (i.e., the imaginary parts k_{f_i} and k_{b_i} associated with the vectors k_f and k_b are positive). In this case, however, the influence of diffusion is seen to make both the real (phase) and imaginary (attenuation) components functions of frequency. In the limit of low

activity and low frequency, the closed-form solutions (Eqs. [44] and [45]) reduce to the simplified nondispersive forms expressed by Eqs. [39] and [40].

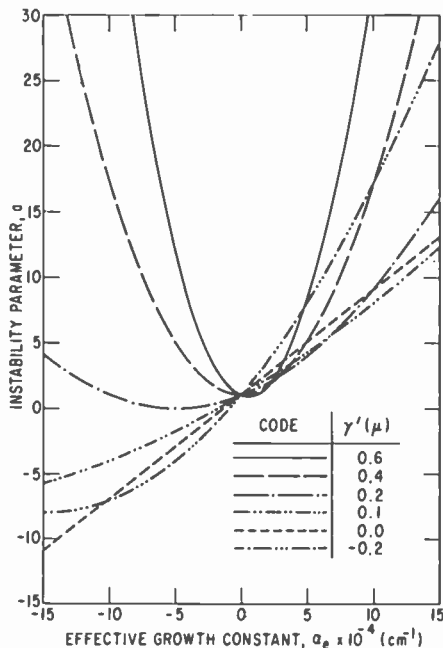


Fig. 9—Instability parameter a as a function of the growth constant α_e for the condition $\gamma_o = 0.2\mu$ and $n_d = n_o$ with γ' as a parameter.

3.6.1 Wave-Type Instabilities (Absolute and Convective)

Before we analyze the propagation vectors in more detail, we shall examine the variable a (Eq. [46]), which is related to the activity parameter α_c and is modified by the effects of diffusion. If there is no field dependence of the diffusion constant ($\gamma' = 0$) and if $\alpha_c < 0$, then $a < 1$, with the possibility that a could become negative. It will be shown that the sign of a must remain positive in order for the device to sustain a stable growing space-charge wave leading to a two-terminal negative resistance. The effect of the field-dependent diffusion (i.e., $\gamma' > 0$) will be shown to provide a damping effect on the device activity.

A plot of the variable a is shown in Fig. 9 in terms of the parameters α_e and γ' for the conditions $\gamma_o = 0.2\mu$ and $n_d = n_o$. As already discussed, when $\gamma' = 0$, the variable a varies from a negative value for

large negative values for α_e to a positive value for $\alpha_e > \alpha_c$, and α_c corresponds to the critical value of α_e at which $a = 0$ (i.e., $-\xi_e^2/4\gamma_0$). With $\gamma_0 = 0.2 \mu\text{m}$, $\alpha_c = -1.25 \times 10^4 \text{ cm}^{-1}$. As the effect of the field dependence of diffusion is increased (i.e., $\gamma' > 0$) the value of a is made progressively more positive in the region for $\alpha_e < 0$. In fact, when $\gamma' \geq 0.2 \mu\text{m}$, the corresponding value for a remains positive regardless of the value of α_e . In this latter condition, the variable a becomes a parabolic function of α_e evenly centered around α_c . This condition will be shown to result in nonunique values for the phase constant and the associated group and phase velocities. A negative value for γ' has been included, although this condition does not necessarily exist in a physical device.³⁵

The condition for $a < 0$ requires further consideration. In this case the phase constant associated with the real parts, k_{fr} and k_{br} , of the propagation vectors, retains a finite value as the frequency is reduced to zero (i.e., when $b = 0$, $d = \sqrt{a}$ and therefore $k_r \rightarrow \pm \sqrt{a}/2\gamma_u$). One of the implications of this condition is that, whereas the phase velocity v_p ($v_p = \omega/k_r$) is equal to the carrier drift velocity v_u in the absence of diffusion, it becomes equal to zero when $a < 0$. At the same time, the group velocity v_g ($v_g = \partial\omega/\partial k_r$) associated with the propagation of energy through the active material may be shown to approach infinity as $\omega \rightarrow 0$. Thus, in the absence of any applied signal ($\omega = 0$), a small perturbation E_1 would grow in *time* although remaining stationary in *space*. This latter condition is associated with the form of absolute instability defined by Briggs.²⁹

A necessary and sufficient condition for an infinite (unbounded and uniform) system to support amplifying waves is that a complex ω with a negative imaginary part ($\omega_i < 0$) be obtained from the dispersion equation (Eq. [29]) and that the imaginary part of k change sign as $\omega_i \rightarrow -\infty$. The usual statement on the stability of a wave is whether or not the dispersion equation yields complex ω for real k (with $\omega_i < 0$). The criterion developed²⁹ to determine whether a wave instability is nonconvective (an absolute instability) is to determine if there is a double root of k for some complex ω for $-\infty < \omega_i < 0$ for which the two merging roots come from different halves of the complex k -plane (upper and lower). The required mapping operation of lines of a constant real part of ω into the complex k -plane has been performed by Guéret³⁰ for the case where there is no field-dependent diffusion. These results are readily extended to be applicable to the present analysis corresponding to the condition $a < 0$, in agreement with our earlier conclusions.

The absolute instability results in the temporal growth of the

electric field at every point in space (nonconvective). On the other hand, by satisfying the condition $a \geq 0$ for $\alpha_e < 0$, the resulting convective wave grows in space as it propagates through the system with its time dependence at a fixed point in space exclusively determined by the time dependence of the excitation. A simple physical interpretation of the absolute instability is to note that with $\omega = 0$ and $a \leq 0$ we find, from Eqs. [44], [45], and [48] that with $c = 0$, $k_{fi} = k_{bi} = \zeta_e/2\gamma_o$ with $\zeta_e > 0$. In this case, the effective growth and attenuation parameters for the forward and backward waves, are equal in magnitude. Thus the loop gain associated with the feedback loop formed by these waves may be shown to always be equal to unity as the result of a zero phase constant and an infinite group velocity. It should be noted that these conclusions have been based upon an infinite system without consideration of the effects of boundaries. It is possible that the absolute instability could be controlled by modifying the reflective properties associated with the anode contact. Although the presence of an absolute instability and the associated temporal growth would require a nonlinear large signal analysis in order to substantiate its effect on the static field redistribution, it has been presumed that the end result should be a stationary, nonuniform, high anode-field condition.^{31,32} In this limit, because the small-signal, uniform-field criterion used here to develop this instability would not be applicable, particularly due to the highly nonuniform distribution of $\alpha(x)$ that would result (e.g., Fig. 5), the end result appears at this time to be purely speculative.

The instability condition $a = 0$ represents a critical point in device behavior. This condition has been plotted in Fig. 10 for the dependence of the required critical value of α_r ($\alpha_r = \alpha_c$) in terms of the diffusion parameters γ_o and γ' . The approximation that $n_o = n_d$ in Eq. [30] has been used. Once again, both negative as well as positive values for the field dependence of diffusion have been considered, although only the positive values are admissible from physical considerations. Since negative values of γ' have been considered in the literature,^{34,35} however, they will be admitted here in order to clarify their significance. In each case, as the static diffusion parameter γ_o is increased, the required value for α_r increases with an increase in γ' . Once γ' exceeds γ_o , however, the condition $a = 0$ cannot be satisfied for any α_r and the device remains in a *convectively* amplifying space-charge mode. It is apparent from these curves that the critical condition is caused by the static presence of diffusion (i.e., when $\gamma' = 0$, the critical value for α_r decreases in inverse proportion to γ_o). A positive value for γ' has the effect of compensating the growth effect of α_e , with the poten-

tial of completely eliminating the critical condition. On the other hand, if negative values for γ' were admissible, they would cause the absolute instability mode to appear for relatively small values of α_c .

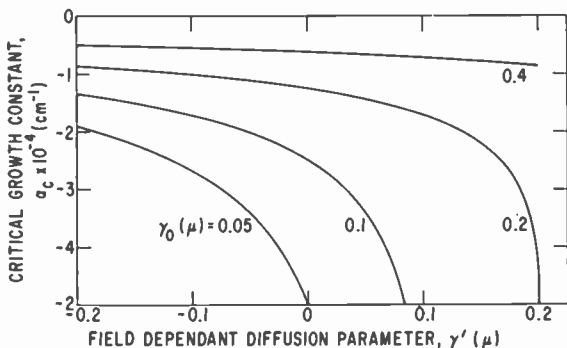


Fig. 10—Critical growth constant α_c in terms of the field-dependent diffusion parameter γ' for several values of γ_0 .

3.6.2 Phase and Group Velocities

An examination of the real parts k_{rr} and k_{br} of the propagation vectors, k_f and k_b indicates that they are equal in magnitude but opposite in phase. The corresponding phase velocity, v_p , which is equal to the velocity associated with the propagating space-charge equiphase wavefront, may be expressed relative to the carrier drift velocity v_o as

$$\frac{v_p}{v_o} = \left(\frac{k_r}{\beta} \right)^{-1} = \frac{\tau}{\tau_p}, \quad [50]$$

where τ and τ_p represent the transit times for the drifted carriers and space-charge waves, respectively. Similarly, we may express the group velocity v_g relative to the carrier drift velocity as

$$\frac{v_g}{v_o} = \left(\frac{\partial k_r}{\partial \beta} \right)^{-1} = \left(\frac{v_p}{v_o} \right)^{-1} (a^2 + b^2)^{1/2} = \frac{\tau}{\tau_g}, \quad [51]$$

with a group transit time τ_g . The physical significance of the group velocity is normally that it is the speed of travel of a modulation signal characterized by a small group of sinusoidal components

located in a narrow band of frequencies around a carrier frequency ω_0 . However, its validity is only justified when the propagation constant is characterized by a phase constant that is limited to a first-order relationship with frequency and when the attenuation constant is frequency independent. Otherwise, the individual frequency components associated with the modulation will be delayed differently, resulting in a distorted wave. In our specific case of a propagating space-charge wave, the group velocity can be interpreted to be associated with the energy of the wave.

From Eq. [51], the group velocity is seen to be inversely related to the phase velocity, such that their geometric mean becomes equal to the carrier drift velocity v_0 in the limit of low activity, small diffusion ($a \rightarrow 1$) and low frequency ($\omega \rightarrow 0$). In the case of low frequencies, both the group and phase velocities become equal with

$$\frac{v_g}{v_0} = \frac{v_p}{v_0} = \sqrt{a}, \quad b = 0, \quad a > 0 \quad [52]$$

At high frequencies, with $b \gg a$, the group velocity approaches a value twice as large as the phase velocity with,

$$\left. \begin{aligned} \frac{v_g}{v_0} &\rightarrow (2b)^{1/2} \\ \frac{v_p}{v_0} &\rightarrow \left(\frac{b}{2}\right)^{1/2} \end{aligned} \right\} \quad b \gg a \quad [53]$$

It is readily apparent that the increasing dependence of the phase velocity on frequency as the frequency is increased makes the semiconductor a dispersive propagation system. In addition, the condition $b \gg a$ generally should lead to decaying waves because of the diffusion cutoff.

The normalized phase and group velocities v_p/v_0 and v_g/v_0 are plotted against frequency in Figs. 11 and 12, respectively. In these examples, the static diffusion constant $\gamma_0 = 0.2 \mu\text{m}$, while the effect of the field dependent diffusion has been introduced as a parameter (i.e., $\gamma' = 0$ and $\gamma' = 0.2 \mu\text{m}$). The effect of γ' is observed to *increase* the phase velocity. The dependence of both velocities on frequency is clearly evident. Since both of these functions are directly related to the variable a , several interesting effects can be observed following an earlier discussion. So long as $\gamma' < \gamma_0$ (e.g., $\gamma' = 0$), both velocities

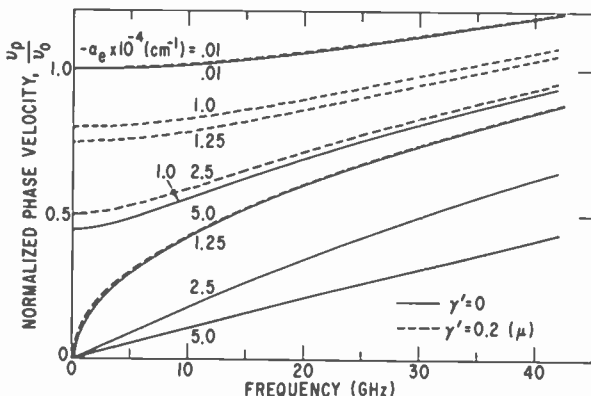


Fig. 11—Normalized phase velocity v_p/v_0 as a function of frequency and α_e for $\gamma_0 = 0.2 \mu\text{m}$ and $\gamma' = 0$ and $0.2 \mu\text{m}$.

are uniquely determined as a function of both frequency and the parameter α_e . In this case, the phase velocity steadily decreases as α_e is increased (in a negative sense), reaching zero for $\alpha_e \geq \alpha_c$ and $\omega = 0$. Thus when $\alpha_e > \alpha_c$ the group velocity approaches infinity as the frequency is reduced to zero. On the other hand, when $\gamma' \geq \gamma_0$ (see Fig. 9), the variable a is never negative, and consequently both the phase and group velocities approach zero as $\alpha_e \rightarrow \alpha_c$ and $\omega \rightarrow 0$. In this latter condition, any further increase of α_e results in these velocities retracing their previous values until $\alpha_e = 2\alpha_c$. This condition results in a retrace of the case where $\alpha_e \approx 0$. If $|\alpha_e| > |2\alpha_c|$, each of the velocities would become larger than the carrier velocity v_0 regard-

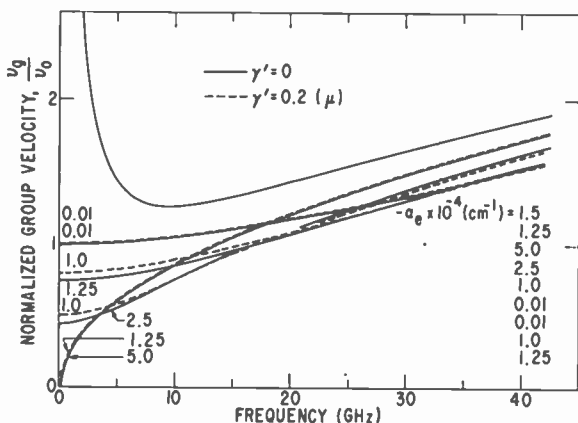


Fig. 12—Normalized group velocity v_g/v_0 as a function of frequency and α_e for $\gamma_0 = 0.2 \mu\text{m}$ and $\gamma' = 0$ and $0.2 \mu\text{m}$.

less of frequency. The most important observation from these curves is the virtual elimination of the possibility of an infinite group velocity as the effect of field-dependent diffusion is established. Under these circumstances, an absolute instability cannot be supported.

3.6.3 Forward Wave Growth—Backward Wave Decay

The frequency dependence of the effective growth (attenuation) constants k_{f1} and k_{b1} associated with the propagation of the forward and backward waves, normalized to the parameter $-\alpha_e$, are plotted in Figs. 13 and 14, respectively. In these examples, $\gamma_0 = 0.2 \mu\text{m}$ while γ' is used

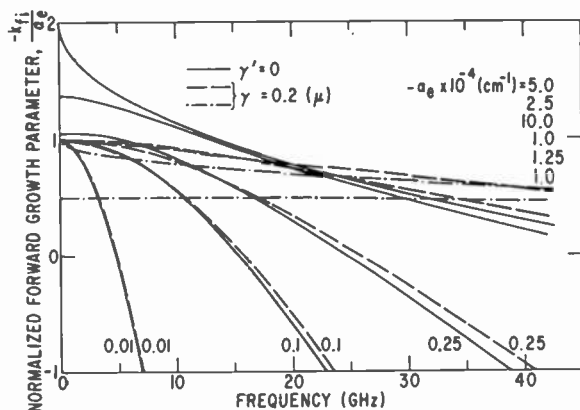


Fig. 13—Normalized forward growth parameter $-k_{f1}/\alpha_e$ as a function of frequency and α_e for $\gamma_0 = 0.2 \mu\text{m}$ and $\gamma' = 0$ and $0.2 \mu\text{m}$.

as a parameter (i.e., $\gamma' = 0$ and $\gamma' = 0.2 \mu\text{m}$). Positive values of the ordinate $-k_{f1}/\alpha_e$ (Fig. 13) represent a *growth* constant for the forward wave, with negative values indicating attenuation. On the other hand, taking into account the reversal in direction of propagation and the consequent reversal in sign of the spacial parameter x , the positive values of $-k_{b1}/\alpha_e$ (Fig. 14) represent attenuation for the backward wave. In the latter case, the wave is always attenuated, independent of the value of α_e . It is interesting to note that with $\gamma' = 0$, the attenuation constant k_{b1} decreases from $1/\gamma_0$ to $1/2\gamma_0$ for $\omega = 0$ as α_e is decreased from 0 to $\alpha_c = -1.25 \times 10^4 \text{ cm}^{-1}$. For $\alpha_e < \alpha_c$, the value of k_{b1} remains at $1/2\gamma_0$. In the case where $\gamma' = 0.2 \mu\text{m}$, the low-frequency value of k_{b1} remains equal to $1/\gamma_0$ for $\alpha_e \geq \alpha_c$ increasing to larger values for $\alpha_e < \alpha_c$. In any case, the value of k_{b1} is almost constant with respect to frequency.

In the case of the forward wave, the effect of diffusion and its influence on the frequency dependence of k_{fi} is apparent. When α_e is small (i.e., $|\alpha_e| < .1 \times 10^4 \text{ cm}^{-1}$), the effective growth constant is only marginally affected by γ' , with its value steadily decreasing from a growth into a decay mode as frequency is increased. The significance of a cutoff frequency and critical wavelength ($k_{fi} = 0$) (Eq. [42]) is clearly indicated. For the case where $\gamma' = 0$, there is a strong enhancement of the growth at low frequencies α_e approaches α_c (with $k_{fi} > -\alpha$). The influence of γ' is observed to remove this effect so that, when $\gamma' = 0.2 \mu\text{m}$, $k_{fi} < -\alpha_e$ for all values of α_e . For $|\alpha_e| > |\alpha_c|$, the effective value for k_{fi} begins to decrease away from $-\alpha_e$, although its value remains almost constant over a wide frequency band extending beyond 40 GHz.

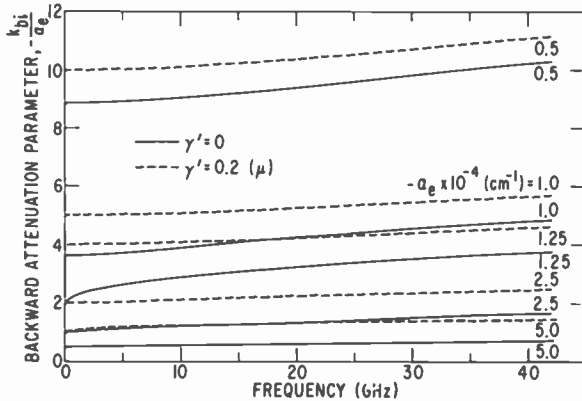


Fig. 14—Normalized backward attenuation parameter $-k_{bi}/\alpha$ as a function of frequency and α_e for $\gamma_0 = 0.2 \mu\text{m}$ and $\gamma' = 0$ and $0.2 \mu\text{m}$.

4. Conclusions

The present theoretical analysis has provided additional insight into the dynamics of space-charge growth in a transferred-electron device. By incorporating a positively graded doping profile between the cathode and anode contacts, the space-charge growth mechanism is found to become uniform. This condition has permitted the use of a rigorous linearized analysis leading to a closed-form solution for the dispersion relation. These results have been used to study the influence of field-dependent diffusion on the behavior of the charge carrier waves. These waves have been found to exhibit two distinct forms of instability. An absolute instability (temporal growth) leading to a

stable nonuniform distribution at high anode electric fields will be sustained if a critical growth condition is satisfied, so long as the effect of the field dependence of diffusion is limited. Otherwise, a convective (spatial) form of instability will be supported, so long as the excitation frequency is below a cutoff value.

The effect of the field dependence of diffusion has been shown to have a damping effect upon device activity. Whereas the presence of static diffusion induces a backward wave, giving rise to the possibility of an absolute instability, the negative differential effect of diffusion tends to reduce if not completely nullify that instability. In the convective mode, the overall effect of diffusion remains dissipative, tending to reduce growth as the excitation frequency is increased.

References:

- ¹ H. Ehrenreich, "Band Structure and Electron Transport of GaAs," *Phys. Rev.*, Vol. 120, p. 1951, Dec. 1960.
- ² B. K. Ridley and T. B. Watkins, "The Possibility of Negative Resistance Effects of Semiconductors," *Proc. Phys. Soc. (London)*, Vol. 78, p. 293, Aug. 1961.
- ³ C. Hilsum, "Transferred Electron Amplifiers and Oscillators," *Proc. IRE*, Vol. 50, p. 185-189, Feb. 1962.
- ⁴ B. K. Ridley, "Specific Negative Resistance in Solids," *Proc. Phys. Soc. (London)*, Vol. 82, p. 954, Dec. 1963.
- ⁵ B. K. Ridley, "The Propagation of Space-Charge Waves in a Conductor Exhibiting a Differential Negative Resistance," *Phys. Letters*, Vol. 16, p. 105, May 1965.
- ⁶ H. Kroemer, "Theory of the Gun Effect," *Proc. IEEE*, Vol. 52, p. 1736, Dec. 1964.
- ⁷ D. E. McCumber and A. G. Chynoweth, "Theory of Negative Conductance Amplification and of Gunn Instabilities in 'Two-Valley' Semiconductors," *IEEE Trans. Electron Devices*, Vol. ED-13, p. 4, Jan. 1966.
- ⁸ H. Kroemer, "External Negative Conductance of a Semiconductor with Negative Differential Mobility," *Proc. IEEE*, Vol. 53, p. 1246, Sept. 1965.
- ⁹ H. W. Thim, M. R. Barber, B. W. Hakki, S. Knight and M. Uenohara, "Microwave Amplification in a DC Biased Bulk Semiconductor," *Appl. Phys. Letters*, Vol. 7, p. 167, Sept. 1965.
- ¹⁰ H. W. Thim and M. R. Barber, "Microwave Amplification in a GaAs Bulk Semiconductor," *IEEE Trans. Electron Devices*, Vol. ED-13, p. 110, Jan. 1966.
- ¹¹ B. S. Perlman and T. E. Walsh, "Stabilized Supercritical Transferred Electron Amplifiers," *Digest Tech. Papers, ISSC Conf., Phila., Pa., Feb. 1969* and *IEEE Trans. Solid State Circuits*, Vol. SC-4 p. 374 Dec. 1969.
- ¹² B. S. Perlman, "CW Microwave Amplification from Circuit Stabilized Epitaxial GaAs Transferred Electron Devices," *Digest Tech. Papers, ISSC Conf., Phila., Pa., p. 134, Feb. 1970* and *IEEE Trans. Solid State Circuits*, Vol. SC-5, p. 331-337, Dec. 1970.
- ¹³ B. S. Perlman, L. C. Upadhyayula and R. E. Marx, "Wideband Reflection Type Transferred Electron Amplification," *IEEE Trans. Microwave Theory and Techniques*, Vol. MTT-18, p. 911-921, Nov. 1970.
- ¹⁴ B. S. Perlman, C. L. Upadhyayula and W. W. Siekanowicz, "Microwave Properties and Applications of Negative Conductive Transferred Electron Devices," *Proc. IEEE*, Vol. 59, p. 1229, Aug. 1971.
- ¹⁵ J. Magarshack and A. Mircea, "Wideband CW Amplification in X-Band with Gunn Diodes," *Digest Tech. Papers, ISSC Conf., Phila., Pa., p. 132, Feb. 1970*.
- ¹⁶ J. Magarshack and A. Mircea "Stabilization and Wideband Amplification Using Overcritically Doped Transferred Electron Diodes," *MOGA 70, Eighth Int'l Conf. on Microwave and Optical Generation and Amplification, Amsterdam, Sept. 1970*.
- ¹⁷ M. A. Lampert, "Stable Space-Charge Layers Associated with Bulk Negative Differential Conductivity: Further Analytic Results," *J. Appl. Phys.*, Vol. 40, p. 335, Jan. 1969.
- ¹⁸ P. N. Butcher, W. Fawcett and N. R. Ogg, "Effect of Field-Dependent Diffusion on Stable Domain Propagation in the Gunn Effect," *Brit. J. Appl. Phys.*, Vol. 18, p. 755, June 1967.

- ¹⁹ P. S. Hauge, "Domain Velocity in Semiconductors with Field Dependent Carrier Diffusion," *IEEE Trans. Electron Devices*,
- ²⁰ P. Jeppesen, "The Influence of Diffusion on the Stability of the Supercritical Transferred Electron Amplifier," *Proc. IEEE*, Vol. 60, p. 452, April 1972.
- ²¹ P. Jeppesen and B. I. Jeppsson, "A Simple Analysis of the Stable Field Profile in the Supercritical TEA," *IEEE Trans. Electron Devices*, Vol. ED-20, p. 371, April 1973.
- ²² J. E. Carroll, *Hot Electron Microwave Generators*, Arnold (Publishers) Ltd., London, 1970.
- ²³ H. Kroemer, "Detailed Theory of the Negative Conductance of Bulk Negative Mobility Amplifiers in the Limit of Zero Ion Density," *IEEE Trans. Electron Devices*, Vol. ED-14, p. 476-492, Sept. 1967.
- ²⁴ R. W. H. Engelmann and C. F. Quate, "Linear, or 'Small Signal', Theory for the Gunn Effect," *IEEE Trans. Electron Devices*, Vol. ED-13, p. 44, Jan. 1966.
- ²⁵ A. Sasaki and T. Takagi, "Conditions for Amplification, Oscillation in GaAs Bulk Semiconductor," *Proc. IEEE*, Vol. 54, p. 2027, Dec. 1966.
- ²⁶ Y. Suematsu and Y. Nishimura "Small Signal Admittance of Bulk Semiconductor Devices at Higher Frequencies," *Proc. IEEE*, Vol. 56, p. 242, Feb. 1968.
- ²⁷ R. W. H. Engelmann, "On 'Supercritical' Transferred-Electron Amplifiers," *AEU Electronics and Communications*, Vol. 26, p. 357, 1972.
- ²⁸ A. H. W. Beck, "Space Charge Waves," Pergamon Press, 1958.
- ²⁹ R. J. Briggs, "Electron-Stream Interaction With Plasmas," MIT Press, Cambridge, Mass., 1964.
- ³⁰ P. Guéret, "Convective and Absolute Instabilities in Semiconductors Exhibiting Negative Differential Mobility," *Phys. Rev. Letters*, Vol. 27, p. 256, Aug. 1971.
- ³¹ H. Thim, "Stability and Switching in Overcritically Doped Gunn Diodes," *Proc. IEEE*, Vol. 59, p. 1285, Aug. 1971.
- ³² P. Guéret and M. Reiser, "Switching Behavior of Over-critically Doped Gunn Diodes," *Appl. Phys. Letters*, Vol. 20, Jan. 1972.
- ³³ B. S. Perlman, *A Study of Space-Charge Instabilities and Negative Resistance Amplification in Transferred Electron Devices*, Ph.D. Dissertation, Polytechnic Institute of Brooklyn, New York, N. Y. (1973).
- ³⁴ G. Dohler, "Shockley's Positive Conductance Theorem for Gunn Materials with Field-Dependent Diffusion," *IEEE Trans. Electron Devices*, Vol. ED-18, p. 1190, Dec. 1971.
- ³⁵ P. S. Hauge, "Static Negative Resistance Gunn Effect Materials with Field-Dependent Carrier Diffusion," *IEEE Trans. Electron Devices*, Vol. ED-18, p. 390, June 1971.
- ³⁶ J. G. Ruch and W. Fawcett, "Temperature Dependence of the Transport Properties of Gallium Arsenide Determined by a Monte Carlo Method," *J. Appl. Phys.* Vol. 41, p. 3843, Aug. 1970.
- ³⁷ P. N. Butcher and W. Fawcett, "Calculation of the Velocity-Field Characteristics for GaAs," *Phys. Letters*, Vol. 21, p. 420, June 1966.
- ³⁸ J. G. Ruch and G. S. Kino "Transport Properties of GaAs," *Phys. Rev.*, Vol. 174, p. 921, Oct. 1968
- ³⁹ J. G. Ruch and G. S. Kino, "Measurement of the Velocity-Field Characteristics of Gallium Arsenide," *Appl Phys. Letters*, Vol. 10, p. 40, Jan. 1967.
- ⁴⁰ T. Ohmi and S. Hsiro, "Dynamic Properties of Electrons in Two-Valley Semiconductors," *Proc. Int'l. Conf. on Physics of Semiconductors*, 1970.
- ⁴¹ M. Suga and K. Sekido, "Effects of Doping Profile upon Electrical Characteristics of Gunn Diodes," *IEEE Trans. Electron Devices*, Vol. ED-17, p. 275, April 1970.
- ⁴² H. Pollmann and R. W. H. Engelmann, "On Supercritical Reflection-Type Amplification and the Stability Criterion in Bulk GaAs Devices," *Proc. MOGA Conference*, Amsterdam, Sept. 1970 (Kilmer-Deventer 1970).
- ⁴³ R. Charlton, K. R. Freeman and G. S. Hobson, "Stabilization Mechanism for 'Supercritical' Transferred Electron Amplifiers," *Electronic Letters*, Vol. 7, p. 575, Sept. 1971.
- ⁴⁴ W. Fawcett and H. D. Rees, "Calculation of the Hot Electron Diffusion Rate for GaAs," *Phys. Letters*, Vol. 29A, p. 578, Aug. 1969.

Millimeter-Wave Phase Shifter

B. J. Levin and G. G. Weidner

RCA Advanced Technology Laboratories, Camden, N. J.

Abstract—A technique particularly applicable at millimeter wavelengths is described for electronically varying the phase shift per unit length in rectangular waveguides using a distributed p-i-n diode. Design, construction, and experimental evaluation at 140 GHz are described.

Introduction

The utilization of frequencies in the millimeter-wave band (considered here as frequencies above 16 GHz) is expected to increase significantly within the next two decades. This increase is being brought about by a number of related causes including:

- a. the crowded condition of the lower frequency spectrum,
- b. the wide bandwidths and narrow beamwidths available at millimeter wavelengths,
- c. the successful extension of a number of microwave components, notably solid-state sources, into the millimeter-wave region,¹ and
- d. the secure communications nature of certain frequencies in the millimeter-wave band.

For these reasons, electronic systems for communications, reconnaissance and surveillance, control, and monitoring are beginning to appear at millimeter-wave frequencies. The specific advantages of using the higher frequencies vary depending on the application, while

the disadvantages include increased atmospheric attenuation and a lack of "off-the-shelf" components. The performance of many microwave devices degrades as the techniques and design parameters are extended to higher and higher frequencies. Indeed, many of the phenomena used in the successful development of microwave devices cease to exist or become impossible to implement (due to extremely severe tolerances) at millimeter-wave frequencies, thereby requiring new approaches to device implementation.

One such device is the electronically controllable phase shifter needed for scanned phased-array antenna applications. These antennas, consisting of an aperture filled with many individual radiating elements, permit fast, inertialess scanning of a radiated electromagnetic beam. The beam geometry is varied by adjusting the relative phase (and amplitude) of the various elements. The heart of the array is the digital phase shifter where the active phase control is exercised.

At the lower microwave frequencies, electronically controllable phase shift is obtained with ferrites² or p-i-n diode switches.³ At millimeter-wave frequencies, however, the losses introduced by these devices become excessive and the required mechanical tolerances become extremely difficult to maintain.

This paper discusses a novel approach to the problem of low-loss electronically controlled phase shifting at millimeter-wave frequencies using a bulk semiconductor in a guided-wave structure.⁴ Phase shift is produced by the electronic modulation of the width of a rectangular waveguide. The change in effective width of the waveguide is accomplished by means of a p-i-n diode that is literally distributed along a sidewall of the waveguide as shown in Fig. 1. With no bias applied to the diode, the transmission line is a rectangular waveguide of width a loaded with a dielectric slab of width t . Application of a suitable bias signal causes injection of free charge carriers into the i region of the diode in sufficient density for its millimeter-wave conductivity to be raised to a high value, thereby moving the effective waveguide wall to the free surface of the diode and changing the width of the waveguide to d in Fig. 1. The result is a change in the waveguide propagation constant and, therefore, a change in phase shift per unit length relative to the unbiased condition.

The following section contains a theoretical discussion of the slab-loaded waveguide. Various geometries are considered and the relevant parameters are determined. Following this, experimental results are presented and discussed. In the concluding section a unique array antenna particularly suited for millimeter-wave applications and quite compatible with the distributed p-i-n diode phase shifter is discussed.

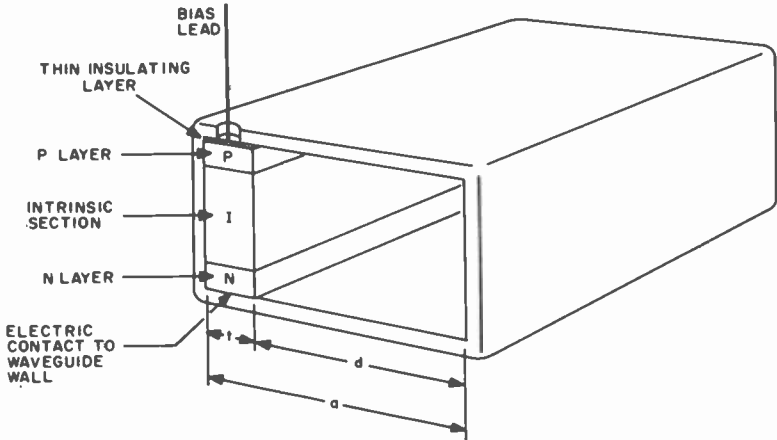


Fig. 1—Phase-shifter geometry.

Theory

In the distributed p-i-n diode phase shifter, the diode has the effect of a semiconductor slab loaded in a section of rectangular waveguide. In order to obtain a quantitative description of the device operation, a theoretical analysis of the propagation in loaded waveguides was undertaken.

The multiple slab geometry considered in the analysis is shown in Fig. 2. Each region is assumed to be uniform and homogeneous, with

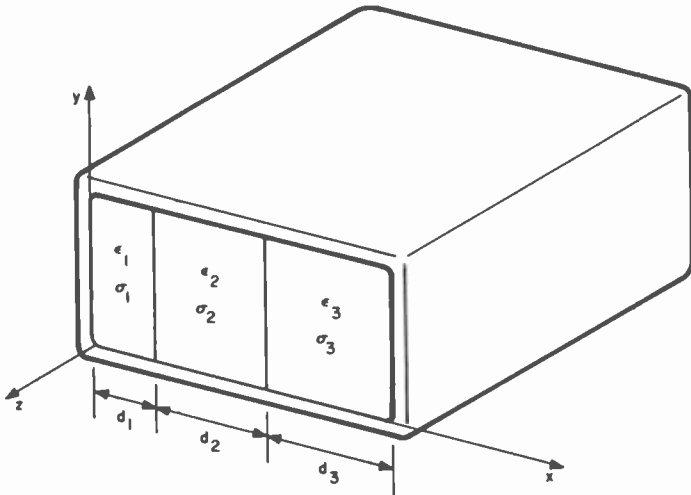


Fig. 2—Multiple-slab-loaded waveguide geometry.

a dielectric constant ϵ_i and conductivity of σ_i . For a p-i-n diode mounted on the narrow waveguide wall (as shown in Fig. 1) region 1 in Fig. 2 is a semiconductor slab and regions 2 and 3 are free space. For a p-i-n diode mounted on a dielectric slab, region 2 is the semiconductor, region 1 is a low-loss dielectric, and region 3 is free space. (This latter geometry will be shown to have certain advantages.)

The normal modes of propagation for a waveguide loaded with a dielectric slab are not, in general, transverse electric (TE) or transverse magnetic (TM) modes, but a combination of a TE and TM mode.⁵ However, the normal modes are either transverse electric or transverse magnetic with respect to the slab boundary planes. This orientation is due to the fact that normal to the slab boundary the "guide" appears uniform, with the narrow walls acting as a short-circuit load. The field components are, in this case, derived from a single vector potential that is directed normal to the slab boundary plane. The resultant fields are either transverse electric or transverse magnetic to the interface normal. For the former the electric field lies in the longitudinal interface plane, and the mode is referred to as a longitudinal-section electric (LSE) mode. For the latter the magnetic field lies in the longitudinal interface plane, and the mode is referred to as a longitudinal-section magnetic (LSM) mode. A special case of the LSE mode is the TE_{N0} of rectangular waveguide. These modes are the natural modes for the geometry of Fig. 2, both because of the slab orientation and because the fields will be launched by a TE_{10} wave in empty waveguide.

Propagation along the waveguide for the geometry of Fig. 2 is given by the exponential factor of $e^{\gamma z}$ and must be the same in each region if the boundary conditions at the interfaces are to be satisfied for all arbitrary values of z . Here, $\gamma = \alpha + j\beta$ is the composite propagation constant for the composite waveguide structure. The real part, α , is the attenuation per unit length, while the imaginary part, β , is the phase shift per unit length. These quantities (actually the ratio β/α) are useful in describing phase shifter performance.

If we apply the boundary conditions that the fields are continuous across the various interfaces and that the tangential component of electric field vanishes on the perfectly conducting waveguide walls, we can obtain the characteristic equation for the propagation constant. This equation is transcendental and requires the use of numerical techniques for a solution. A root-search algorithm used in conjunction with a high-speed digital computer has produced useful solutions.⁶ The root-search method used is a modified version of the method of steepest descent.

Initial results were obtained for a single semiconductor (silicon) slab on the waveguide sidewall, as shown in Fig. 3. The computer-generated results are shown in Fig. 4. Here the real (attenuation) and imaginary (phase shift) parts of the propagation constant are plotted as functions of the slab conductivity with relative slab thickness as a parameter. The frequency is 140 GHz and the waveguide type is RG-138/U.

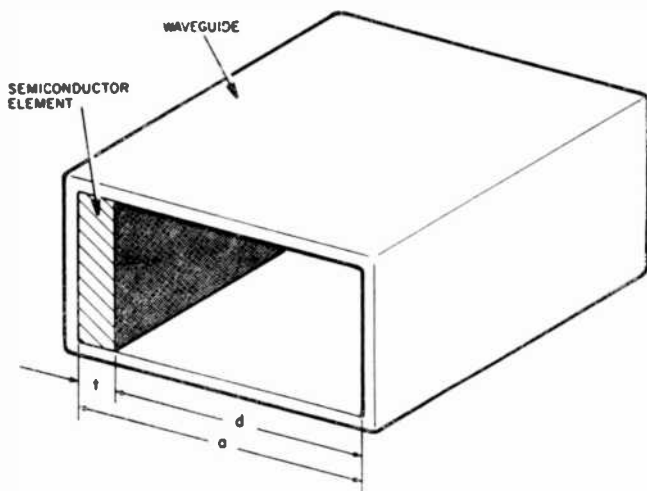
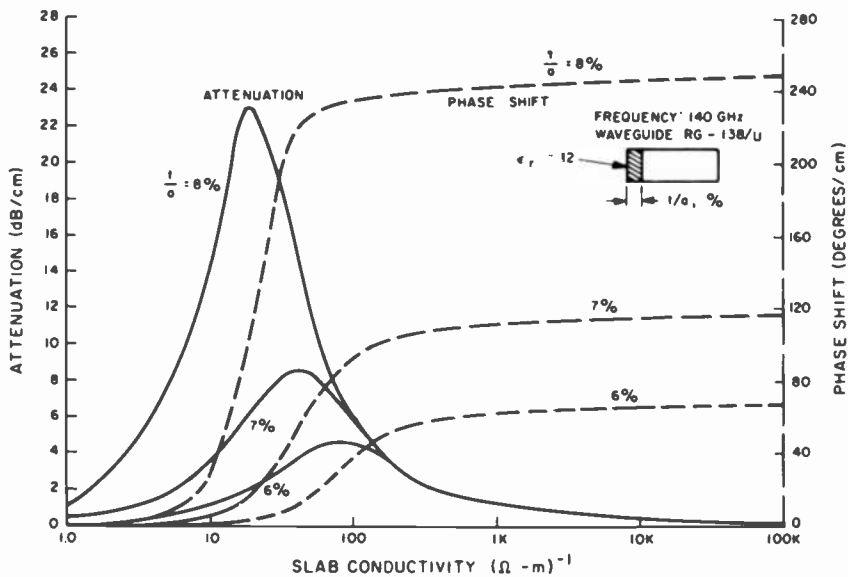


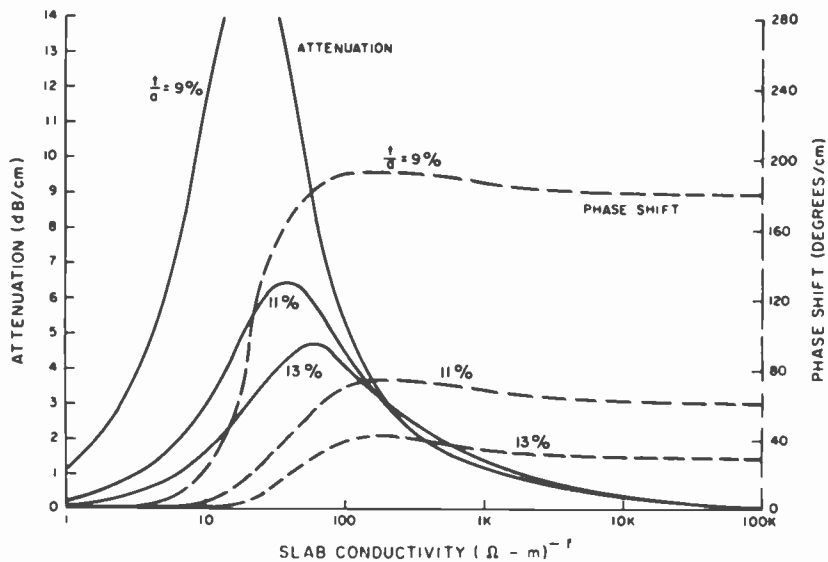
Fig. 3—Single semiconductor slab on waveguide sidewall.

Examination of these curves indicates that maximum phase shift is obtained for a relative slab thickness t/a of about 8%. This slab thickness corresponds to approximately one-quarter wavelength at 140 GHz. For slab thicknesses greater than this critical thickness, the electric and magnetic field distribution in the waveguide is altered. The fields become concentrated in the semiconductor slab or at its surface and they decay exponentially into the unloaded section of the waveguide.⁷ This effect is responsible for the increase in attenuation and the decrease in phase shift.

The analytical results have been extended to a number of other slab geometries. Among them are a semiconductive slab mounted off the narrow wall of the waveguide (with and without a dielectric spacer between the slab and the wall) and two slabs mounted symmetrically at each of the narrow walls. All of these cases can be treated as a waveguide containing three homogeneous regions, as shown in Fig. 2. Typical computer-generated results are shown in Figs. 5,



(a)



(b)

Fig. 4—Computed phase shift and attenuation for a semiconductor slab loaded waveguide: (a) Slab thickness $\leq 8\%$ and (b) slab thickness $> 8\%$.

6, and 7. For the curves in Fig. 5, the slab width is maintained constant and the slab is spaced progressively off the narrow wall. These curves are useful for tolerance studies; they show that if the slab is located slightly off the narrow wall the device performance can

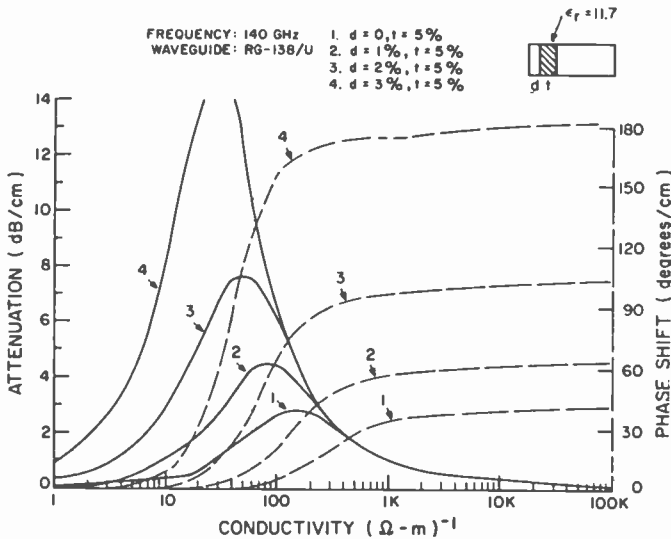


Fig. 5—Phase shift and attenuation for a single slab spaced away from the waveguide sidewall.

be significantly affected. The curves in Fig. 6 correspond to a semiconductor mounted on a dielectric slab (whose dielectric constant is the same as that of the semiconductor). In this case the sum of the two slab widths has been maintained constant. These curves indicate that the same amount of phase shift is obtained as we make the semiconductor slab thinner but maintain the total thickness of the semiconductor slab and dielectric constant. There is a limit to how far this can be carried, in that the semiconductor thickness must be at least one skin depth in its high-conductivity state. Assuming the semiconductor to be quasi-metallic in the high-conductivity state, the skin depth δ can be approximated by⁸

$$\delta = \frac{1}{(\pi f \mu \sigma)^{1/2}} \text{ (meters)}$$

where f is the frequency, μ the slab permeability, and σ the slab con-

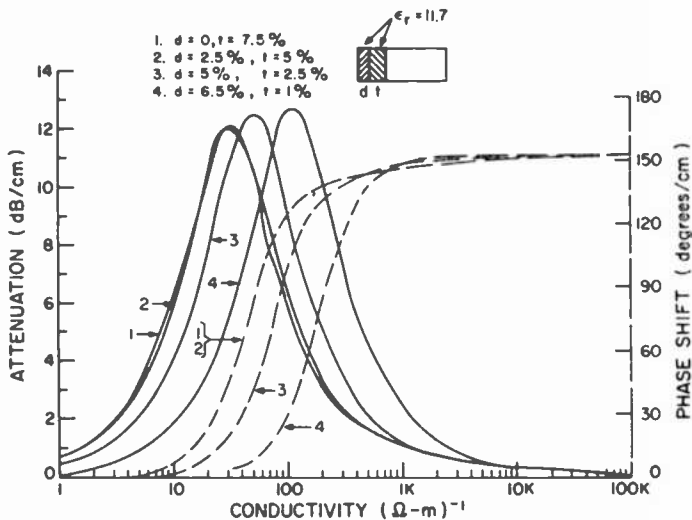


Fig. 6—Phase shift and attenuation for dielectric spacer between single slab and waveguide sidewall.

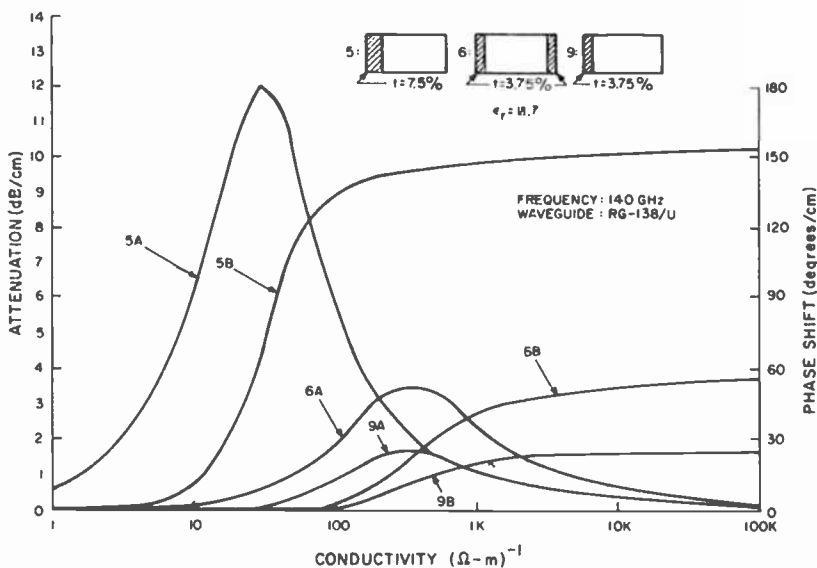


Fig. 7—Phase shift and attenuation for symmetrically and asymmetrically loaded wave guide at 140 GHz.

ductivity. At 140 GHz, with $\sigma = 10^4$ (ohm-meters) $^{-1}$, and $\mu = \mu_0$, the skin depth is about 0.053 mil, or about 1.3 micrometers. This depth corresponds to a relative slab thickness of less than 0.1%. Another requirement on the composite structure is that the sum of the semiconductor and dielectric-slab thicknesses be kept less than one-quarter wavelength in order to avoid the surface-type waves discussed above, where the field becomes concentrated in the lossy semiconductor. One possibility for obtaining the two-layer structure is to epitaxially grow the thin semiconductor structure on a high-resistivity substrate. Epitaxial-silicon technology has become highly advanced over the past decade and appears to be readily applicable to the distributed p-i-n diode phase-shifter elements.

The curves in Fig. 7 compare the symmetrically and asymmetrically loaded slab waveguides. These curves show that, in general, dividing the slab along its width and mounting the two resulting slabs symmetrically on opposite narrow walls will result in less phase shift as compared to the original slab mounted asymmetrically. The lower phase shift result from the fact that the thinner slabs are in regions of weaker electric field for the TE_{10} type waves that are being propagated. The symmetrical arrangement may be advantageous when using two semiconductor slabs whose sum is greater than a quarter wavelength and also for the case of two thinned semiconductor slabs mounted on lossless dielectric slabs. For this latter case, a slab whose relative thickness is 2% of the waveguide width, mounted on 14% thick dielectric, would lead to surface waves in the semiconductor. Making the arrangement symmetrical (i.e., two 1% slabs on 7% dielectrics) might lead to a useful, efficient device. To date, however, these structures have not been studied, either theoretically or experimentally.

Experimental Results

Initial measurements were performed on two sets of bulk-silicon slabs of various conductivity. All the slabs were 40 mils high by 1 cm long, and their conductivities covered the range from 1 (ohm-m) $^{-1}$ to 10^4 (ohm-m) $^{-1}$. The slabs of one set were 6.2 mils wide ($t/a = 7.8\%$), whereas those of the other set were 13 mils wide ($t/a = 16\%$). The slabs were placed, one at a time, along the sidewall of a section of RG-138/U waveguide and their insertion loss and relative phase shift were measured at 140 GHz. Attenuation was measured by the standard substitution technique using a calibrated variable attenuator. Phase-shift measurements were obtained by means of a waveguide bridge, using a slotted line to track changes in phase shift.

The results for the thinner slabs are shown in Fig. 8. For comparison, the computer-generated data corresponding to a slab thickness of 7.5% are also shown. As can be seen, there is favorable agreement between the experimental and theoretical curves. The higher measured losses at low and high conductivities can be accounted for by the discontinuities at the boundaries between the unloaded and loaded sections of the waveguide. In the experimental setup, no matching has

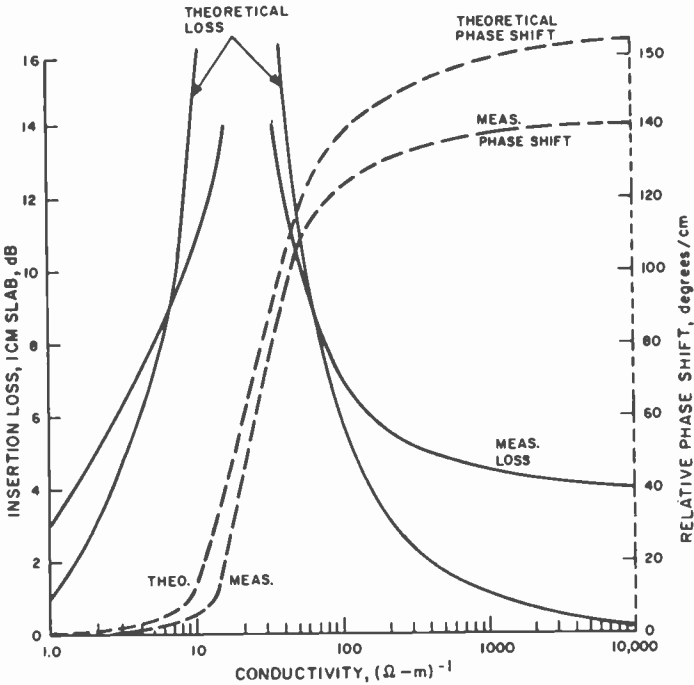
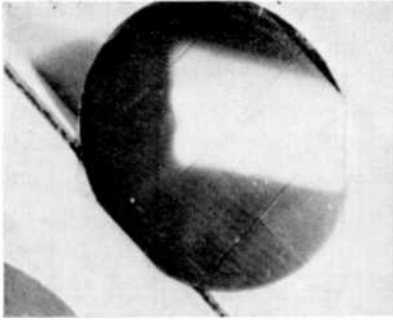


Fig. 8—Measured and theoretical phase shift and insertion loss for a silicon slab on a waveguide sidewall at 140 GHz.

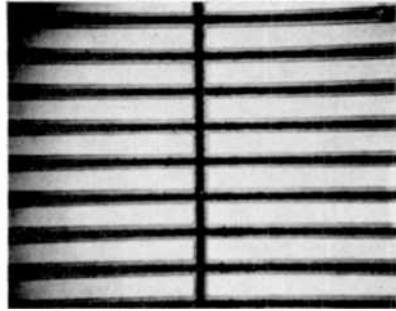
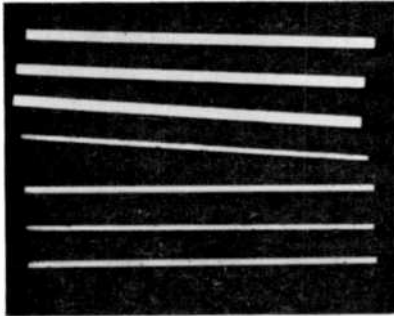
been introduced to decrease reflections at these boundaries, whereas in the theoretical analysis the waveguide is assumed to be uniformly loaded and thus these boundaries do not exist.

Only limited results have been obtained from the thicker (16%) slabs. These showed little phase shift ($< 10^\circ$) even for the high-conductivity slabs. This result agrees with the theoretical results, which indicated a continual decrease in phase shift for slab widths greater than 8%.

A number of batches of p-i-n diodes were fabricated in order to demonstrate electronically controlled phase shift at millimeter-wave



WAFER PATTERNS APPLIED

WAFER FACE AFTER
LASER SCRIBING

FINISHED DIODES

Fig. 9—p-i-n diodes before and after dicing.

frequencies. The diodes were formed by means of conventional diffusion techniques. The "intrinsic" material from which sample diodes were made was n-type silicon having resistivities in the range 50 to 1600 ohm-cm. The wafer thickness was in the range 6 to 13 mils. The heavily doped n^+ and p^+ layers were formed by phosphorus and boron diffusions, respectively, to depths of 2 to 15 μm . Metal contacts were then sputtered onto the faces of the wafer, followed by a masking and etching step to delineate the individual diodes. Dicing was done by means of a laser scriber or a multiple wire saw. Fig. 9 shows the diodes before and after separation.

Measurements were made of the diodes spreading resistance, I - V characteristics, and excess carrier lifetime. These measurements confirmed that conductivity modulation was occurring. The excess carrier lifetime was measured by a pulse technique to be in the range of 2 to 4 μs . This result implies an ambipolar diffusion length of only

about 3 mils and indicates that the conductivity modulation in a 10-mil-high diode would probably not be uniform throughout the entire length of the i region. This nonuniform conductivity modulation would be worse for thicker diodes, thus limiting the diode thickness to less than 10 mils. This limitation would be relaxed if the excess carrier lifetime could be increased by at least an order of magnitude.

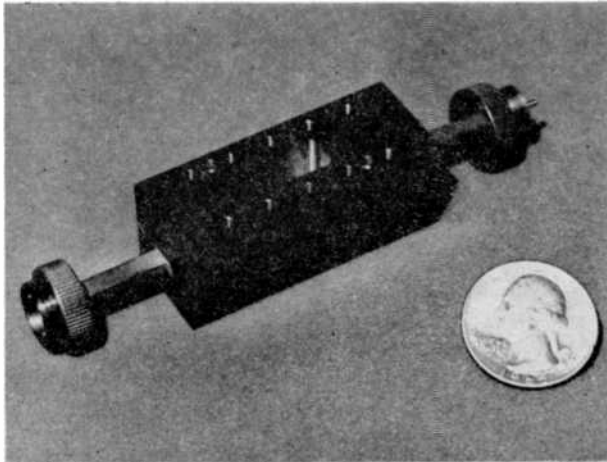
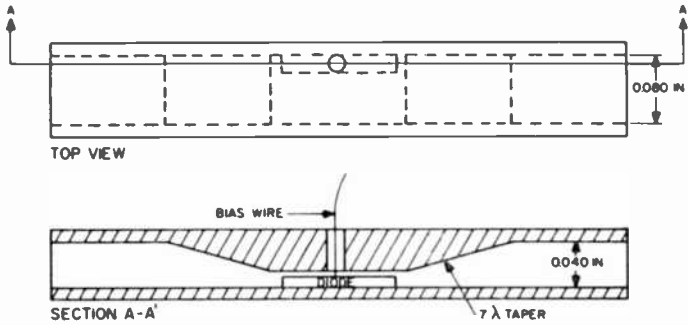


Fig. 10—Experimental diode mount.

In the rf evaluation of these diodes, the waveguide height was tapered from its 40-mil standard to 20 mils. Any further taper (to match more closely the approximate 10-mil height of the diodes) was found to lead to high test-mount insertion loss (> 10 dB) due to the concentrated nature of the fields. Fig. 10(a) shows a cross-sectional view of the diode mount, looking through the narrow wall of the

waveguide; Fig. 10(b) is a photograph of the assembled mount. The diodes were held in place in the mount by low-density polyfoam spacers or wedges of Rexolite 1422. The dc bias was established by allowing one contact strip of the diode to rest against the bottom of the waveguide, while a fine insulated wire was inserted through a small hole in the top of the waveguide to make contact with the other diode contact strip.

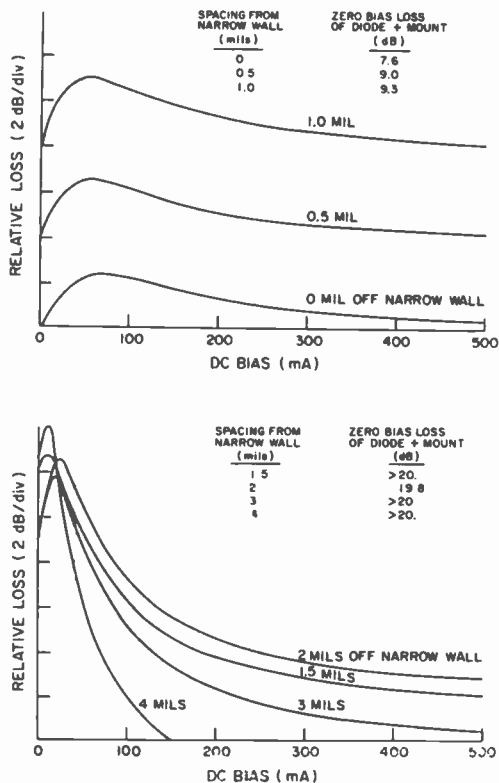


Fig. 11—Loss characteristic of diode G19-1F for various mounting positions.

The various distributed p-i-n diode samples were tested for attenuation and phase shift at 140 GHz. All diodes were 1 cm long and were tested for forward-bias currents in the 0 to 500 mA range. The test results were found to be quite sensitive to the position of the diode within the mount. For any given diode, the strongest effects were due to the proximity of the diode to the waveguide sidewall. Fig. 11 shows the loss characteristic for a typical diode as a function of its position with respect to the sidewall. The indicated spacings

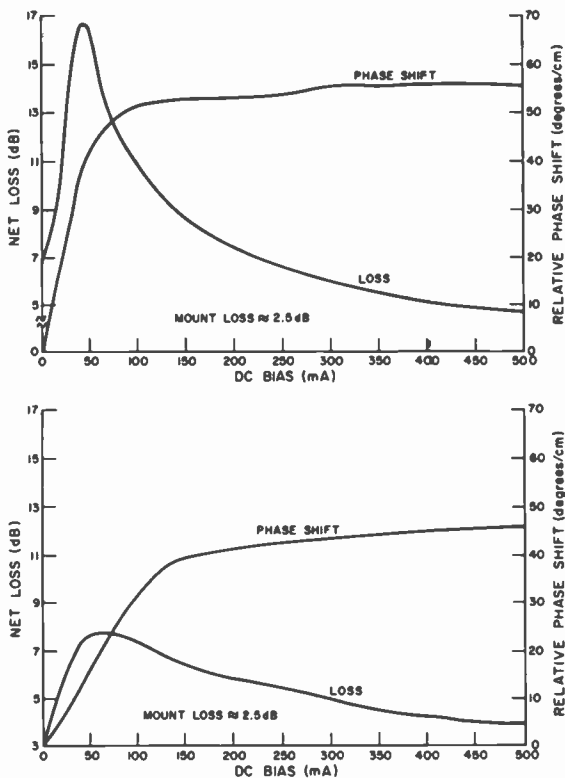


Fig. 12—Measured phase shift and insertion loss for two different p-i-n diodes at 140 GHz.

were obtained by means of Mylar shims placed between the diode and the waveguide wall.

The phase shift and insertion loss of two other diodes are shown in Fig. 12. Diodes G3-D2 had a 50 ohm-cm resistivity i layer, while diode G9-D2 had a 1600 ohm-cm resistivity i layer. The higher resistivity material is seen to introduce less loss, which is desirable for efficient phase shifters.

Applications

The computer-generated phase shift and insertion loss characteristics of a silicon slab of varying conductivity, shown in Fig. 4a, indicate that a phase shifter with attractive performance (i.e., 100°/dB or

better) is possible. The measured data on bulk silicon slabs, shown in Fig. 8, tend to confirm the theoretical predictions and indicate that there are no fundamental reasons why a conductivity-modulation phase shifter cannot be built that will offer attractive performance at 140 GHz or other millimeter wave frequencies. The measured data for p-i-n diodes has the same form as the theoretical data. The similarity is only qualitative, however, primarily because the p-i-n diodes tested did not fill the entire height of the waveguide and the conductivity modulation effect was incomplete in that it did not extend uniformly through the entire i layer due to limited excess carrier lifetime.

The "storage time" of these p-i-n diodes is of the same order of magnitude as the excess carrier lifetime. Since, in striving for efficient conductivity modulation, one seeks to maximize the lifetime in the distributed p-i-n diodes, "very-high-speed" applications, such as phase modulators for wideband communication channels, are automatically eliminated. In addition, the high attenuation exhibited by the distributed p-i-n diodes at intermediate phase-shift settings generally precludes their use as analog phase shifters. We are left with a phase shifter having moderately fast switching speed (a few microseconds) and an inclination toward binary operation. Such a device has an important application as the heart of an electronically steerable antenna.

Digital beam steering control in a phased array requires that any combination of several bits of phase shift be selectable for each antenna element. A typical requirement is that each element have a 4-bit phase shifter. That is, each phase shifter must be capable of producing any combination of 180° , 90° , 45° , or 0° of relative phase shift. For the distributed p-i-n diode phase shifter, the 4 bits will be obtained by placing four p-i-n diodes end to end. Each diode will be of appropriate length for one of the phase shift bits and each will have a separate bias control.

When considering a "package" for the distributed p-i-n phase shifter, it is desirable to avoid reduced height waveguide. The concentrated fields in the reduced height guide invariably result in increased attenuation relative to full height guide. Yet the p-i-n diode cannot be made to more than about $\frac{1}{4}$ the waveguide height. A solution to this problem can be found in the technique of diode stacking, whereby a number of diodes are physically bonded together in series. This technique is used in the manufacture of high-voltage rectifiers.

Fig. 13 is a line drawing of a unique array antenna⁹ particularly suited for millimeter-wave applications and quite compatible with the

distributed p-i-n phase shifter. The antenna radiates a linearly polarized pencil beam that may be electronically scanned in one plane. The principal feature is a completely confined space feed in the form of a lens-corrected dual-mode sectoral horn. The use of optical techniques is important, since the losses in a transmission line feed would be substantial at 140 GHz.

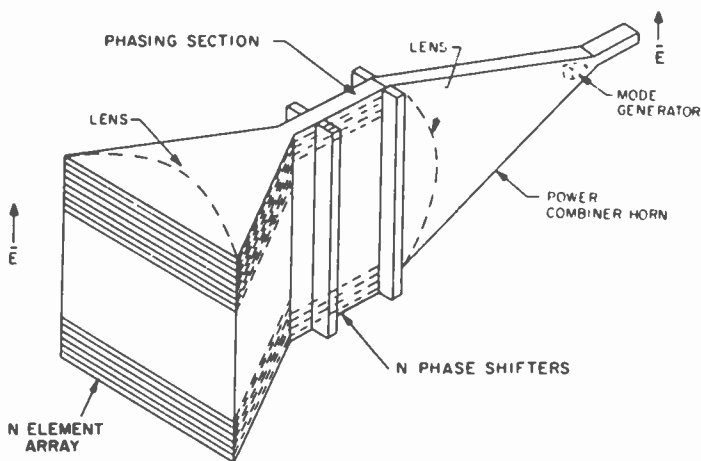


Fig. 13—Line drawing of array antenna.

Conclusions

The distributed p-i-n diode phase shifter has been shown useful for array applications at millimeter wavelengths. At 140 GHz, the possibility of a moderate-resolution (beam widths less than 1° are easily obtainable) array antenna appears promising. An imaging or tracking system based on such an antenna will be readily portable for airborne as well as ground applications, will offer better range in poor visibility conditions than a visible/IR system, and will offer improved resolution over a microwave system of comparable size and weight. Aside from its simplicity, the unit is economical to fabricate and utilizes currently available semiconductor and microwave/millimeter wave technologies.

Acknowledgments

Computer programming was performed by C. Riggi of the RCA Advanced Technology Computation Center. J. Mitchell of RCA Lab-

oratories was responsible for diode fabrication. Useful discussions were held with J. J. Rudnick, H. Sobol, and C. P. Wen. Technical assistance was provided by A. S. Panebianco, H. Walters and L. D. Moore.

References:

- ¹ H. Sobol, private communication.
- ² L. R. Whicker, "Review of Ferrite Phase Shifter Technology," GMTT Microwave Symp., Boulder, Colorado June 4-6 1973.
- ³ J. F. White, "High Power PIN Diode Controlled, Microwave Transmission Phase Shifters," *IEEE Trans. Microwave Theory and Tech.*, Vol. MTT-13, p. 233, March 1965.
- ⁴ B. J. Levin and G. G. Weidner, "A Distributed PIN Diode Phaser for Millimeter Wavelengths," GMTT Microwave Symp., Boulder, Colorado, June 4-6, 1973.
- ⁵ R. F. Collin, *Field Theory of Guided Waves*, p. 224, McGraw-Hill Book Co., New York, 1960.
- ⁶ G. G. Weidner and B. J. Levin, "Millimeter Wave Phase Shifter," Final Report, ECOM-0168-F, (U.S. Army Electronics Command) April 1973.
- ⁷ B. Lax and K. J. Button, *Microwave Ferrites and Ferrimagnetics*, McGraw-Hill Book Co., New York, 1962.
- ⁸ S. Ramo, J. R. Whinnery, and T. Van Duzer, *Fields and Waves in Communication Electronics*, p. 252, John Wiley, New York, 1965.
- ⁹ C. F. Profera, "Evaluation of a Low Sidelobe Phase Array Antenna," NASA Contract Report CR-1741, April 1969.

Design of a Light-Weight Microwave Repeater for a 24-Channel Domestic Satellite System

M. V. O'Donovan, C. M. Kudsia, and L. A. Keyes

RCA Limited, Quebec, Canada

Abstract—The transponder described in this paper has 24 channels, each of which has a pass bandwidth of 36 MHz. The receive frequency band is 5925–6425 MHz and the transmit band is 3700–4200 MHz. The wideband receiver-driver portion of the transponder is all solid state. The characteristics of this design are compared with those of a receiver-driver incorporating driver traveling-wave-tube amplifiers; detailed trade-offs, in terms of performance, weight, reliability and power requirements, are provided.

The input and output multiplexers in the transponder use a graphite fiber epoxy composite as the basic waveguide material. This material, though significantly lighter weight than Invar, possesses a similar thermal expansion coefficient. Details of the performance and weight of multiplexer filters fabricated in graphite fiber epoxy composite are presented and compared with the results achieved with equivalent filters manufactured using Invar. The influence of multipath effects on the overall multiplexer design is also analyzed.

The impact of different communication traffic models on the complexity and weight of the transponder is discussed, and finally, the performance characteristics, weight, and reliability of a baseline 24-channel transponder are presented.

1. Introduction

Communications satellites have undergone continuous evolution since the launch of Telstar in 1962; the net result has been a great increase in capacity produced by increases in the complexity of the communica-

tions payload and in launcher size. Lower cost per channel has resulted because the increase in communications capacity has been greater than the increase in launcher and satellite costs. This increased capacity has occurred in part because the weights of most subsystems do not increase in direct proportion to overall spacecraft weight and, therefore, a larger fraction of the payload is available for communications. The long anticipated introduction of communications satellites into domestic service will offer the opportunity to apply recent advances in materials and techniques to make the best use of this payload weight resource.

This paper describes a proposed 24-channel, all rf single-heterodyne 6-GHz up-channel/4-GHz down-channel transponder designed particularly for use in a geosynchronous, equatorial orbit satellite for the U.S. domestic communications systems. Several such systems have been described in filings before the Federal Communications Commission (FCC).¹ The launch vehicles considered—the Thor Delta, Atlas Centaur, and Titan derivatives—would be used for small, medium, and large-capacity satellites, respectively.

The small satellite is a 12-channel design based on the current Canadian domestic satellite ANIK or Hughes HS333. It would be launched on a 1250-pound transfer orbit capability Delta vehicle. The medium-size satellite is a 24-channel design based on Intelsat IV, which was launched by an Atlas Centaur of 3600-pound transfer orbit capability.

The serious prospect of launcher developments that would raise the transfer orbit rating of the Delta vehicle to the 1800-2000 pound range created a challenge to spacecraft designers. It was estimated that if significant savings could be made in communications payload weight per rf channel over that achieved in Intelsat IV and ANIK, it would be possible to put 24 channels on a Delta-launched satellite.² Alternative uses for weight saving would be increased subsystem hardware redundancy and increased secondary propulsion fuel for longer lifetime.

Most of the transponder weight of previous satellites has been in the traveling-wave-tube amplifiers (TWTA's), especially their power conditioners, and in the multiplexing filters used to separate the channels and recombine them after power amplification. Although the application of solid-state devices to replace TWTA's has been continuously examined, no devices have yet appeared with the combination of dc/rf efficiency, adequate intermodulation, bandwidth, and gain to effectively compete with the output TWTA; consequently no weight saving can be expected in this area. The multiplexer waveguide filters

showed the greatest prospect for weight savings. These devices have been made of relatively thick (0.060-inch) Invar waveguide material forming coupled cavity filters with extra sections being added for amplitude and group delay equalization. Invar was used to achieve stability with temperature, as was dictated by the environment and the narrow bandwidth of the filters relative to their center frequency. Some weight savings could be achieved by machining or eroding away unnecessary material, but it was decided that use of graphite fiber epoxy composite (GFEC) material could achieve the greatest possible weight saving with good temperature stability, although its use introduces problems of fabrication and metallization.

The elimination of equalizers provides further weight saving and the impact of this deletion on performance will be discussed later.

Continuous improvements in the bandwidth, gain, and intermodulation of microwave transistors have now made it possible to replace the 4-GHz driver TWTA with a transistor amplifier. In the transponder described here, double redundancy has been used to achieve adequate reliability based on the most pessimistic, but necessarily preliminary, failure-rate data. It is quite likely that as experience is accumulated and more devices are qualified, single redundancy will prove adequate.

2. Design Criteria

Detailed Intelsat IV transmission objectives are well known, and form a basis of comparison for domestic requirements. Apart from obvious differences between Intelsat and domestic satellite in antenna coverage requirements, which establishes transponder gains and TWT power levels, the major difference is in the multiple-access requirement of the two systems. For both systems we will consider mainly FDMA FM for both message and TV. The Intelsat traffic model typically has many relatively small users (say 12 to 24 voice channels per carrier) accessing a single channel, whereas the domestic traffic tends to concentrate in single large users accessing a channel with up to 1000 voice channels per carrier. The requirement for FM TV transmission are essentially the same for both systems. The Intelsat model places emphasis on achieving low multicarrier intermodulation in the TWTA's and in carefully controlling the amplitude and phase characteristics of the multiplexing filters at band edge to achieve low cross talk. The domestic model places emphasis on getting a high dc/rf efficiency in the TWTA's to minimize power subsystem weight at the expense of multicarrier intermodulation and increased AM/PM conversion.

This latter effect, when coupled with gain slopes introduced mainly by input multiplexers, produces an intelligible cross talk between carriers that rises with modulation frequency and so limits the maximum number of voice channels per carrier in multi-access operation.

The most complete statement of assumptions from which transponder requirements can be derived is given in the ATT August '71 System Application filing to FCC.³ In this document, system noise budgets and link calculations are presented from which main performance parameters of the transponders can be calculated using conventional methods such as those summarized in Reference [4]. For channels that may be used exclusively with a single access such as for TV distribution, it is not necessary to provide the level-setting attenuators used in channels for multi-access use. Although a weight saving is realized it is no longer possible to use all channels interchangeably, so that system reliability may be affected. Level-setting attenuators may be deleted entirely but this will result in unusually high up-link thermal noise contributions if multiple carrier back off operation is planned.

The weight of multiplexing filters is kept low in the present design by not providing amplitude and group delay equalizers. The performance of the resulting filters is adequate for TV, wide-band data, or up to 1000 voice channels in single-access operation. Improvements in system performance or capacity can be expected if compensation is applied at the ground stations in the sending and receiving signal paths. Although the technique of compensating spacecraft group delay on the ground had been tried successfully from the earliest Telstar and Relay experiments, the Intelsat satellites used built-in compensation of the input multiplexer in order to simplify requirements for the large number of earth terminals involved. System compensation of the group delay of the output multiplexer is relatively simple to achieve by inserting equalizers in the earth terminal intermediate-frequency chain prior to FM detection. Amplitude compensation is not considered necessary because the components in the receive chain have low AM/PM conversion and consequently a small amount of AM is not troublesome.

Compensation of the input multiplexer group delay at the sending terminal is more difficult. If a predistorting equalizer is placed in the transmitting chain before the final amplifier, it is probable that the AM/PM of the power amplifier (PA) will interact with the predistorted signal to produce the same kind of distortion that would otherwise be produced in the spacecraft. If the power amplifier AM/PM is low enough, then the system is effectively linear up to the satellite input multiplexer, and the compensation prior to the PA will be effective.

These problems can be circumvented by placing the equalizers after the power amplifier, with the penalty that the equalizers must now pass the full power output of the PA with attendant problems of loss, temperature, cost, and general inflexibility. Further difficulty occurs if the PA must pass two or more carriers, as each carrier may require an equalizer.

The Canadian domestic satellite system is the first to apply the techniques of equalization and predistortion to an operating system in order to minimize spacecraft complexity and weight.

To achieve adequate transponder reliability, two means are used. The first is by use of conventional hardware-switched redundancy and the second is by use of frequency spectrum in the form of spare channels to back up active channels.

3. Transponder Design

The proposed satellite has 24 rf channels, each occupying a 40-MHz band. The available 500-MHz frequency band is re-used by virtue of transmitting and receiving 12 channels with vertical polarization and the other 12 with horizontal polarization. The center frequencies for the two polarization are staggered by 20 MHz.

The transponder has two similar sets of redundant receiver chains—one for each type of polarization. This chain consists of tunnel-diode amplifiers, transistor amplifiers, and a hybrid. The hybrid has two outputs, with each output connected to six channel band-pass filters via a manifold. Any of these sets of six channel-separation band-pass filters is referred to as the input Mux assembly. Each individual channel is amplified by a separate traveling-wave tube (TWT) amplifier. The output of the TWT's is combined by band-pass filters in sets of six channels—a structure similar to the input Mux assembly with the input/output ports reversed. These combining networks are referred to as output Mux assembly.

The output of these six-channel combining networks feeds into the separate ports of the transmit antenna. This effectively combines the two sets of six channels on the same polarization in space. All these features are shown in Fig. 1.

3.1 Solid-State Receiver-Driver

The transponder uses an all-solid-state wide-band receiver-driver that consists of 6-GHz tunnel-diode amplifiers (TDA's), a local oscillator-mixer assembly and a transistorized amplifier to drive the output

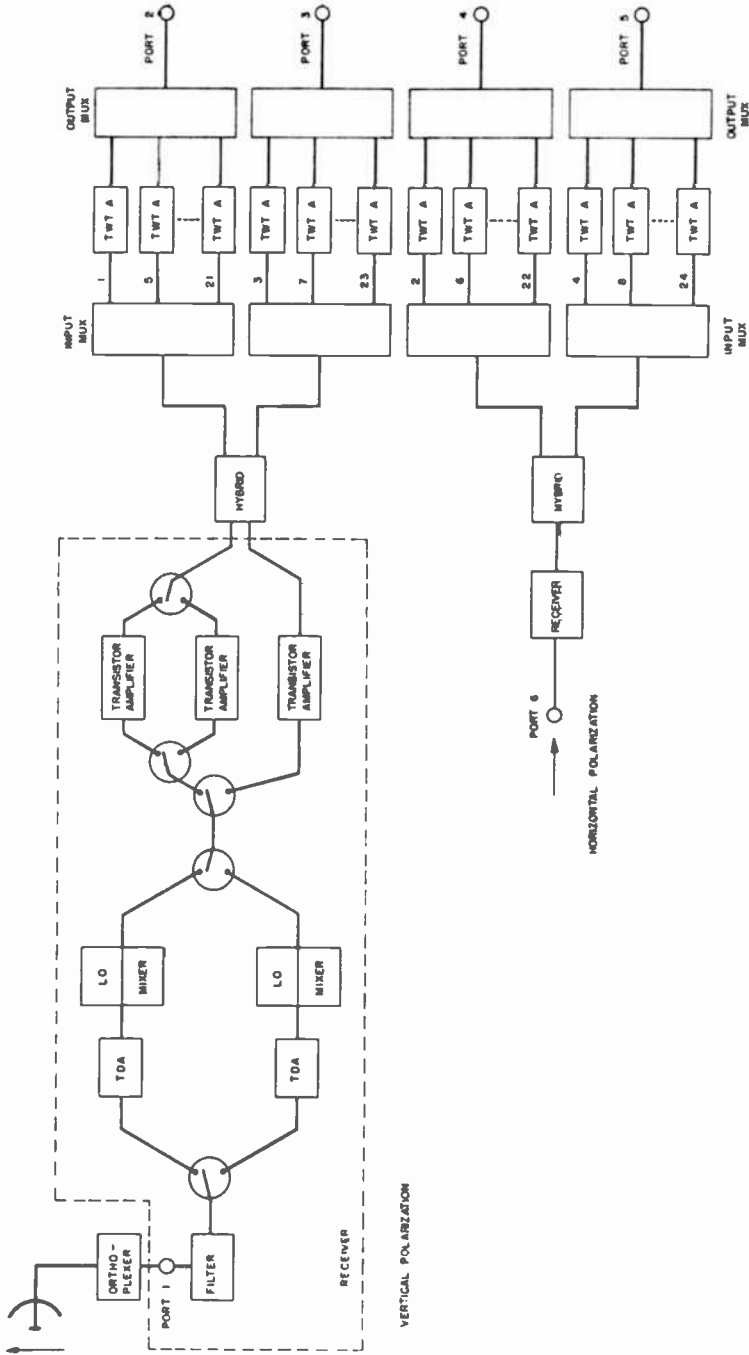


Fig. 1—Block diagram of the proposed transponder.

TWTA. The TDA-mixer portion is singly redundant whereas the transistor amplifier is doubly redundant as shown in Fig. 1. The conventional design of wide-band receiver-driver uses a TWTA instead of the transistor amplifier. The performance of these two designs (transponders A and B in Fig. 2) in terms of their noise contribution, weight, dissipation, and reliability is compared in the subsequent sections. It is assumed that the total gain requirement of the transponder is about 100 dB.

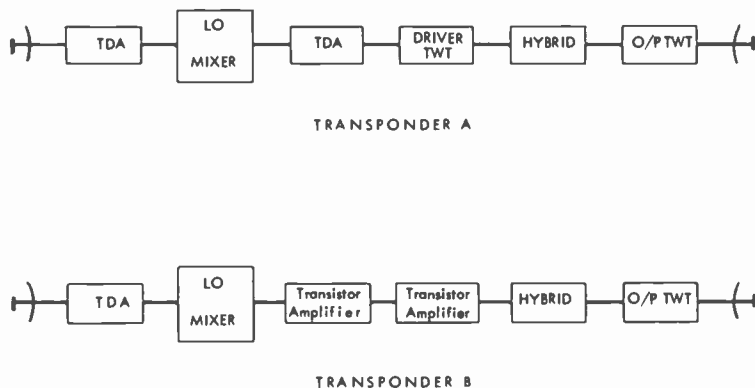


Fig. 2—Representative channels of transponders A and B.

3.1.1 Noise Performance

The total noise power in any channel is made up of thermal noise and intermodulation noise. The makeup of a single channel for the two designs is shown in Fig. 2. The values of parameters assumed for each of the transponders are given in Table 1.

The total gain for each chain is made equal to 98.6 dB. Both thermal noise and intermodulation noise are calculated for each stage. The thermal noise is referred to the input of the first stage and the intermodulation noise is expressed as a carrier to intermodulation ratio. The intercept point concept is used to calculate the level of a single intermodulation product. In the present application, the low-level stages are assumed to have 12 equispaced carriers, while the output stage has a separate TWT for each carrier. Thus, the output stage contributes no intermodulation even though it is

saturated; this is accomplished in the calculation by making the intercept point equal to 200 dBm.

An amplifier with 12 equally spaced carriers has intermodulation products that are coincident with the carriers. As an example, the sixth carrier has 5 third-order products of the form $2f_1 - f_2$ and 40 third-order products of the form $f_1 + f_2 - f_3$. The former have a power

Table 1—Parameters used to calculate carrier to noise performance of transponders A and B.

Element	Loss dB	Gain dB	NF dB	Intercept Point dBm
Transponder A				
6-GHz TDA	0.7	14	5.5	-13.5
Mixer	0.3	-6.5	7.5	- 8.6
4-GHz TDA	0.1	10	7.0	- 6.0
Driver TWT	0.1	32.3	18.5	33.6
Output TWT	5.0	55.0	28.0	200.0
Transponder B				
6-GHz TDA	0.7	14	5.5	-13.6
Mixer	0.3	-6.5	7.5	- 8.6
Trans. Amp. (First Stage)	0.1	14.3	8.0	15.0
Trans. Amp. (Last Stage)	0.1	28.0	8.0	27.0
Output TWT	5.0	55.0	28.0	200.0

weight of unity while the latter have a weight of four, giving a total weighted intermodulation product of 165. Thus, the carrier to intermodulation ratio calculated from the intercept point is reduced by the ratio $165 = 22.18$ dB to give the carrier/total intermodulation for channel No. 6, which is the worst channel. Higher-order intermodulation products are neglected.

The intermodulation noise power and the thermal noise power are calculated, both referred to the input to the first stage, added and the carrier to total noise power determined as a function of drive level. This has been plotted for the two transponder channels as a function of input backoff and is shown in Fig. 3. The carrier to total noise improves as the signal drive level is raised towards saturation. This is because below saturation all channels are dominated by thermal noise. As the drive level is raised, the thermal noise remains constant but the intermodulation increases 2 dB for every 1 dB increase in the input power. Thus, at high drive levels, the intermodulation power

dominates over thermal noise and the carrier to total noise decreases again.

The conclusion that can be drawn from Fig. 3 is that transponder B, using transistor amplifiers, gives the best carrier-to-noise performance in the region of saturation. The improvement (of the order

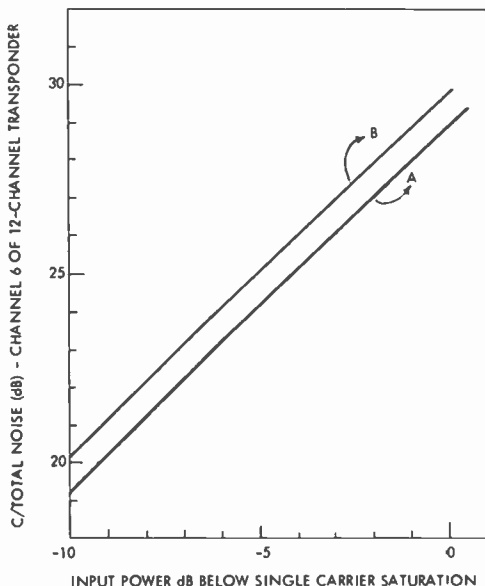


Fig. 3—Carrier to noise ratio for transponders A and B.

of 1 dB compared to a transponder using a driver TWT) is significant in that it allows a decrease in the saturated power level of the transponder by the same amount. This results in a reduction in solar-array area and weight as well as a weight savings in the power-supply units and heat sinks for the output power amplifiers.

3.1.2 Weight and Power Considerations

A survey of available transistor amplifiers for aircraft or possible space applications indicates a pessimistic total weight of 12 ounces including the power conditioning for an amplifier with a gain between 42-45 dB in the 4-GHz band. Such an amplifier in double redundancy will have a total weight of 3.0 lbs. This compares favorably with a driver TWTA that typically weighs 4.0 lbs, including its electronic

power condition (EPC), and exhibits a gain of about 33 dB in the 4-GHz band.

Table 2 gives a detailed comparison in terms of weight and power requirements of the all-solid-state receiver-driver against the design that uses a driver TWTA. This comparison is based on the best available data to date. As can be seen, for the complete 24-channel transponder, the use of transistor amplifiers gives a weight reduction of nearly 13 lbs and reduction in power consumption of 6.0 watts.

Table 2—Weight and Power Comparison between Transponder Receivers using a Driver TWT and Transistor Amplifiers

ITEM	Redundant DTWT Receiver				Redundant Trans. Amp. Receiver			
	No.	Unit Weight (ozs)	Total Weight (ozs)	Power Consump. (watts)	No.	Unit Weight (ozs)	Total Weight (ozs)	Power Consump. (watts)
6 GHz TDA	2	10	20	—	2	10	20	—
Mixer & LO	2	20	40	—	2	20	40	—
4 GHz TDA	2	10	20	—	—	—	—	—
Driver TWT + EPC	2	64	128	4.0	—	—	—	—
Hybrid	1	1	1	—	1	1	1	—
Switch	1	2	2	—	6	2	12	—
Trans Amp					3	12	36	1.0
Misc.								
Hardware			32				32	
TOTAL			243	4.0			141	1.0

3.1.3 Redundancy Considerations

The prediction of failure rate for transistor amplifiers poses problems at present owing to lack of life data on such devices. This uncertainty constitutes the major disadvantage of the solid-state design.

The reliability comparison in this paper is based on the failure rates as depicted in Table 3. It is to be emphasized here that the failure rate of TWTA's is based on their life data in space. The failure rates of the transistor amplifier is based on a combination of parts count and device life data in a laboratory environment. Owing to this uncertainty, comparisons are carried out for an optimistic and a pessimistic failure rate for the transistor amplifier. Failure rates of all other units are consistent with the current standards in the space industry. The failure rate of a standby unit is assumed to be one-tenth its failure rate when active.

The relatively large number of switches that are necessary to

incorporate the redundancies into the alternative designs tend to influence the overall reliability in a significant manner. The switch under consideration is a latching ferrite type built in a three-port package. It is similar to a three-port isolator but with an added coil to reverse the saturation magnetization in the ferrite and thus switch the rf energy to the alternate output port.

Table 3—Failure Rates

UNIT	Failure Rate per 10 ⁹ Hours (FIT)
Driver TWT (with EPC)	1800
TDA	330
Mixer + LO	922
Transistor Amp	
Optimistic	100 FIT/dB
Pessimistic	160 FIT/dB
Ferrite Switch	
Coil	10
Ferrite	10

Two failure modes are recognized for the switch. First, it may fail to switch when required, due, for example, to an open coil. Second, the rf performance may be degraded so that the transponder performance is outside specified performance characteristics, due, for example, to fracture of the ferrite caused by temperature cycling and resulting in high loss, high reflection, or poor isolation. This second failure mode is similar to that experienced by ferrite isolators of the same design. The failure rate of these isolators is usually taken as 10 FIT. The overall switch failure rate is usually taken as 20 FIT, which allots 10 FIT for coil failure and 10 FIT for fracture of the ferrite material.

A failure due to an open (or short) in the driving coil prevents the switch from being operated. It does not affect the reliability of the active chain but it prevents the redundant chain from being put into service. If the failure in the coil occurs after the redundant chain has been switched in, the failure does not affect the reliability of the overall system. On the other hand, switch failure due to fracture of the ferrite will affect both the active and the standby chains. However, this failure mode is likely to cause only a degradation in the performance and not a catastrophic failure. For reliability calculations here, we assume degraded performance as a failure. Thus the failure due to ferrite fracture could be considered as a series multiplicative factor,

while the failure rate due to driving coils could be added to the failure rate of the standby units.

The reliability models for the two alternative configurations (transponders A and B) are shown in Figs. 4(a) and 4(b). Since the computation of reliability of transponder B (Fig. 4b) in a rigorous manner is complicated, this model is simplified to the one shown in Fig. 4(c). Here, all the 5 switches are put in series, and this model

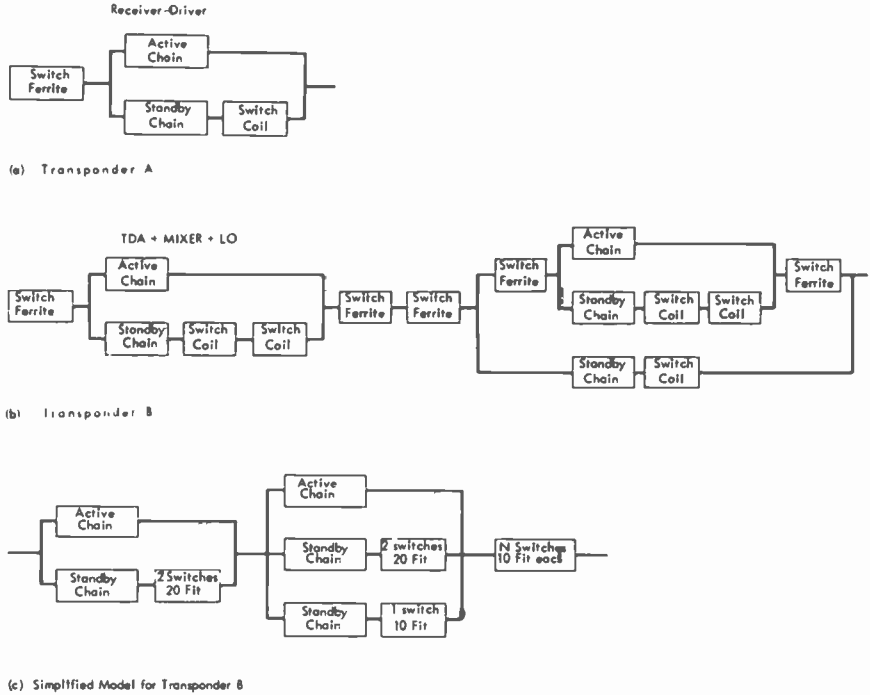


Fig. 4—Reliability models of transponders A and B.

therefore is likely to yield slightly pessimistic results insofar as failure due to ferrite fracture is concerned. An optimistic case would be to put only the three switches in series for ferrite fracture. The correct reliability will lie somewhere in between, and results for both these cases are computed and described in Fig. 5.

The mathematical relationships used to compute the reliability for a single redundant chain is

$$R = R_1 \left[1 + \frac{\lambda_1}{\lambda_2} (1 - R_2) \right];$$

for a doubly redundant chain it is

$$R = \frac{(\lambda_1 + \lambda_2)(\lambda_1 + 2\lambda_2)}{2\lambda_2^2} R_1 \left(1 - \frac{2\lambda_1}{\lambda_1 + \lambda_2} R_2 + \frac{\lambda_2}{\lambda_1 + 2\lambda_2} R_2^2 \right).$$

Here $R_1 = \exp \{-\lambda_1 t\}$ is the reliability of the active chain, $R_2 = \exp \{-\lambda_2 t\}$ is the reliability of the standby chain(s), λ_1 is the failure rate for active units, and λ_2 is the failure rate for standby units.

These equations include the requirement that the standby units assume the failure rate of the active chain when and if they are put into service.

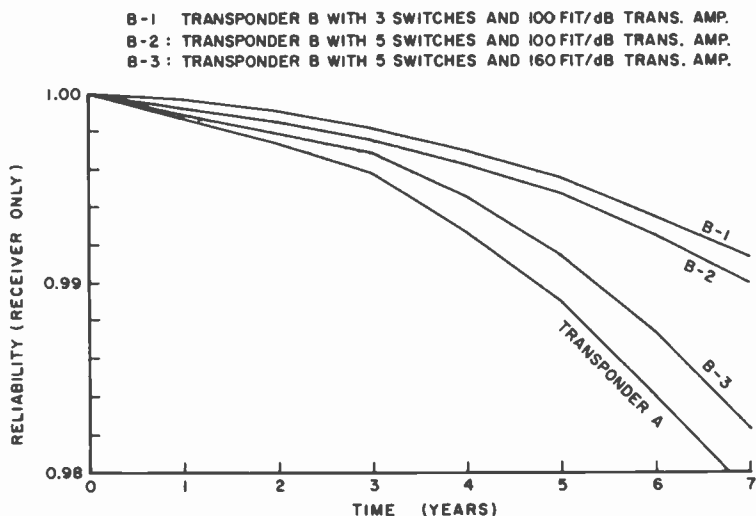


Fig. 5—Comparison of reliability of transponders A and B.

3.2 In-Band Noise—Multipath Effects

In a bandwidth-limited system such as the one under consideration, band-pass filters are required for each FM carrier to permit a minimum carrier separation in order to maximize the channel capacity. The specification of the filter requirements is a compromise between interference from the adjacent carriers and in-band distortion.

3.2.1 Adjacent-Channel Interference

For the system under consideration, there are 24 FM carriers. For any one carrier, the remaining 23 act as interfering carriers. From

this large number of interfering carriers, however, only four could be of any significance. These are:

- (a) Two channels whose center frequencies are 40 MHz above and below the center frequency of the desired channel, reduced in amplitude only by the suppression of the input and output Mux filters.
- (b) Two channels whose center frequencies are 20 MHz above and below the center frequency of the desired channel, reduced in amplitude mostly by the cross-polarization discrimination and to some extent by the suppression and shaping of the input and output Mux filters.

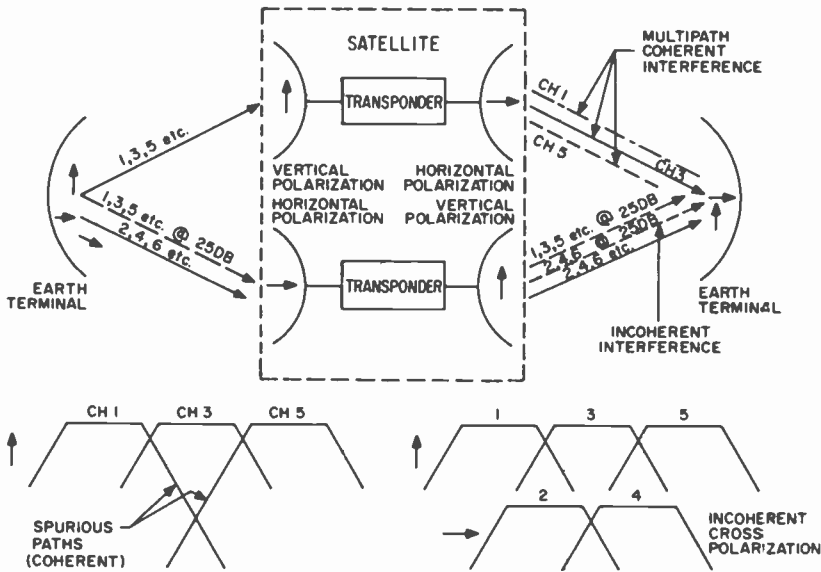


Fig. 6—Multipath effects in the transponder.

All these interfering vectors are incoherent. Furthermore, each cross-polarized interfering channel contributes two interfering vectors as shown in Fig. 6. These channels provide most of the adjacent-channel interference and therefore the cross-polarization discrimination is a critical parameter. Consequently, the communications capacity of this satellite is critically dependent on the expected isolation between the vertically and horizontally polarized waves. The amount of this type of distortion can be computed by the well-established methods of convoluting the spectra of the wanted and unwanted signals.

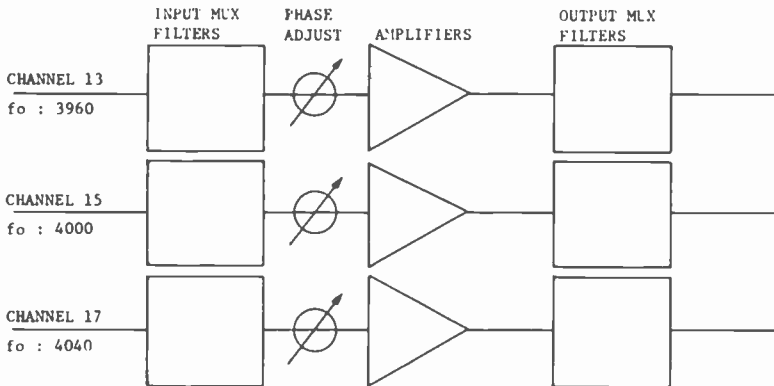
3.2.2 In-Band Distortion

Any passive element, especially the narrow-band band-pass filters, exhibit gain and phase dispersion with respect to frequency. This causes distortion in the signals passing through them.

In addition, distortion arises owing to the transmission of signals via the unwanted, indirect paths through adjacent channels. The strength of the signals through these indirect paths is dependent on the relative gains they provide to the signals and the rejection by the filters. At the output, all these unwanted signals combine with the main signal in a coherent manner. This can be looked upon as additional gain and phase dispersion by virtue of the superposition theorem. The term multipath interference is used here to describe this effect.

Fig. 6 depicts the transmission of a signal between two earth stations via the satellite. Of the various transmission paths for a signal, the channels that are adjacent to the desired channel are the only significant ones. These paths are shown in the figure. Other paths will attenuate the signal by a large amount, making their interfering effect negligible. This is especially true where Chebyshev-type filter functions are used. This type of function exhibits a monotonic increase in attenuation with frequency outside its pass band. The interfering vector (coherent) that is transmitted through the adjacent cross-polarized channel is shown to be 50.0 dB down compared to the main signal. This is based on a 25.0 dB discrimination by the antennas owing to cross polarization. This interfering vector is found to have negligible effect.

The model used to compute the overall channel characteristics is shown in Fig. 7. This model is based on the filtering requirements as derived from Ref. [3] and as outlined in Appendix 1. For purposes of comparison, the Intelsat IV type requirements are described in Appendix 2. All active components are assumed to add constant amounts of gain and phase. The multipath effect is determined by the vector addition of phasors corresponding to the amplitude and phase of any two filter characteristics. The resultant of this can be added vectorially to any other interfering phasor and so on. Arbitrary amounts of gain or phase changes can be introduced in any transmission path. As described earlier, the filter characteristics are simulated by generating the poles and zeros of the proposed filter functions. Appendix 3 describes the poles and zeros for Chebyshev functions. The formulas representing the amplitude and phase response and their derivatives in terms of the poles and zeros are also included in this appendix.



Electrical Characteristics of Filters

	Input Mux Filters	Output Mux Filters
No. of Sections	9	5
Return Loss	-26.0 dB	-26.0 dB
Equal Ripple Bandwidth	37.0 MHz	41.2 MHz
Filter Type	Chebyshev	Chebyshev
Unloaded Q	7,000	10,000

Fig. 7—Simulation model.

3.2.3 Total Group Delay/Gain Slope Response of the Proposed Model

Figs. 8 and 9 depict the total group delay and gain slope, respectively, including the effects of multipath interference. These responses are depicted in parametric form with the phase difference between adjacent channels as a parameter. This phase difference is assumed to be the same between any two adjacent channels on the same polarization. Physically this implies a difference of line lengths between adjacent channels. As can be seen from these responses, multipath interference has a pronounced effect at the band edges. The relevant formulas that include the multipath effects are described in Appendix 4. A sample calculation of intermodulation distortion owing to transmission deviations caused by these filters is outlined in Appendix 5.

3.3 The Use of Ultra-Light-Weight Multiplexer Filters

One of the significant differences between this and previous transponders lies in the substantial weight reduction resulting from the

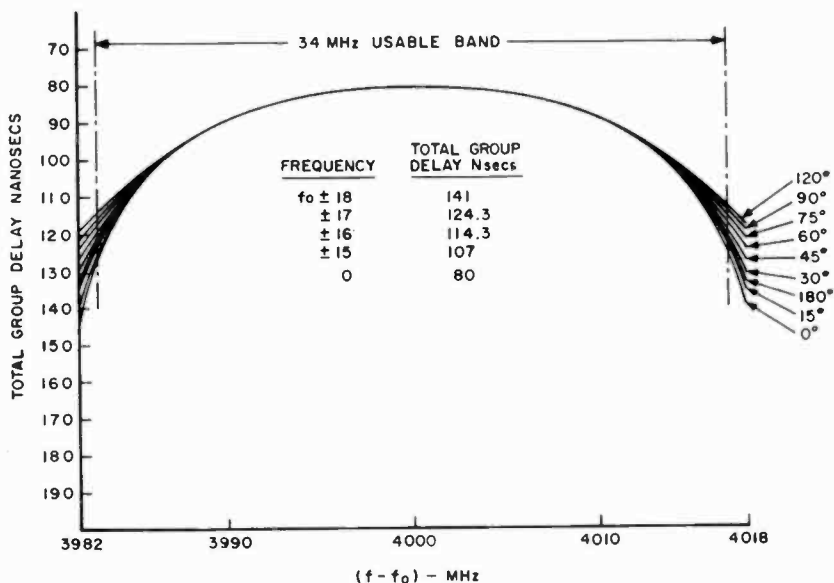


Fig. 8—Total group delay response.

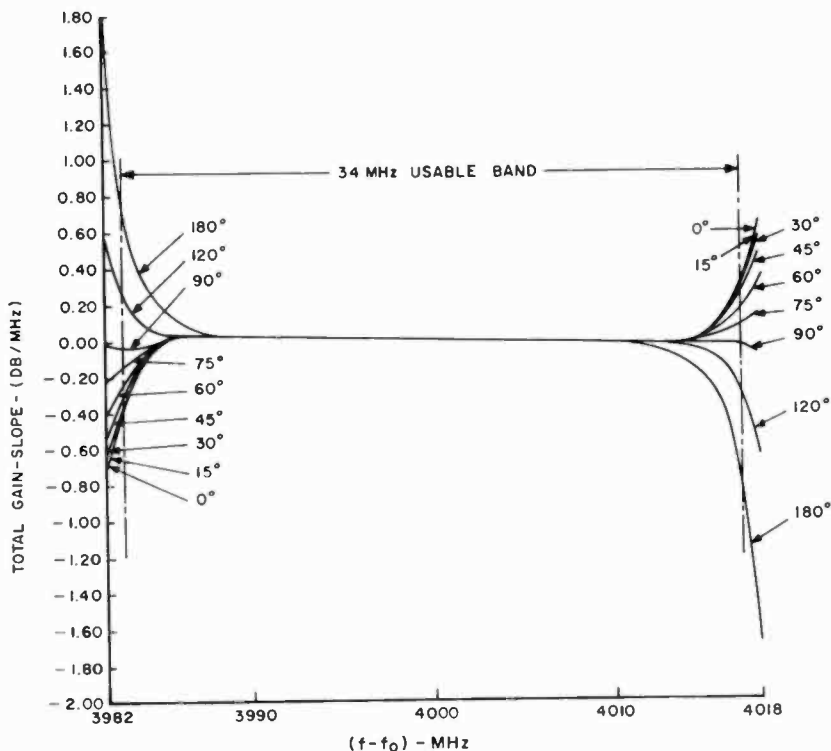


Fig. 9—Total gain slope response.

replacement of Invar filters in the input and output multiplexers by filters fabricated using graphite fiber epoxy composite (GFEC) as the basic waveguide material. This material is much lighter in weight than Invar but possesses a similar coefficient of thermal expansion.

The use of this type of filter is the direct outcome of a two-year development and qualification program in which

- (a) the basic design and manufacturing processes necessary for the production of GFEC waveguide filters exhibiting performance characteristics similar to those of Invar filters have been established, and
- (b) GFEC filters manufactured using formal, aerospace quality, processes have successfully withstood qualification level thermal and mechanical environmental testing.

This program emphasized the requirements of filters in the 4-GHz and 12-GHz frequency bands. The major areas of technological difficulty were: (1) the fabrication of waveguide with a good internal surface finish and dimensional stability; (2) the deposition of high-conductivity plating, and (3) the assembly of filter components into a design exhibiting a frequency drift with temperature equivalent to that of Invar.

Surface Finish and Conductivity

The primary quality factor used in assessing the surface finish of a waveguide band-pass filter is its unloaded Q . An unloaded Q of 11,000 can be achieved with silver-plated Invar filters fabricated in WR229 waveguide and operating in the 4-GHz frequency band. Silver-plated GFEC filters exhibiting unloaded Q 's greater than 10,000 have been consistently manufactured.

The pass-band insertion loss of a six-section output multiplexer filter is shown in Fig. 10. The only non-GFEC materials used in the manufacture of this filter, which has an unloaded Q of 10,800, are the Invar flanges, tuning screws, and bushings.

Frequency Drift with Temperature

GFEC material consists of layers of graphite fiber bonded with interleaved layers of cured epoxy resin, and is not homogeneous. This factor coupled with constraints associated with the mechanics of fiber application to the waveguide cross section result in a waveguide laminate design that provides a coefficient of thermal expansion similar to that of Invar along the length of the waveguide and across the

waveguide width. The obstacles will, however, have a significantly different expansion characteristic.

In Fig. 11, the frequency drift with temperature of a six-resonator direct-coupled GFEC filter is compared with that of an Invar filter with identical electrical characteristics. This graph shows that the effective coefficient of expansion of the GFEC filter is similar in magnitude but opposite in sign to that of the Invar filter. The graph also illustrates that some success can be achieved in minimizing the frequency drift over a typical operating temperature range.

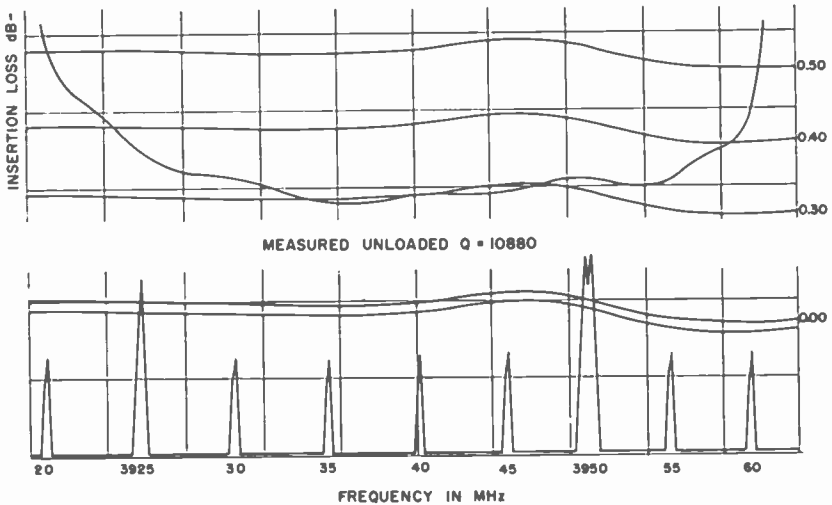


Fig. 10—Passband insertion loss of GFEC filter.

Weight Comparison between Invar and GFEC Multiplexers

The weight of 24-channel input and output multiplexers fabricated using Invar and GFEC filters are compared in Table 4. Five-section direct-coupled Chebyshev filters are used in the output multiplexer and nine-section filters are used in the input multiplexer.

To alleviate the spacecraft layout and mechanical design problems introduced by the large physical size of the 24-channel input multiplexer, the filters are designed in a waveguide whose height is one third that of a standard waveguide. The waveguide height was chosen on the basis of the maximum allowable pass-band gain slope and insertion loss. No other electrical parameter is affected by this design stratagem, which also results in a further weight reduction. Standard-

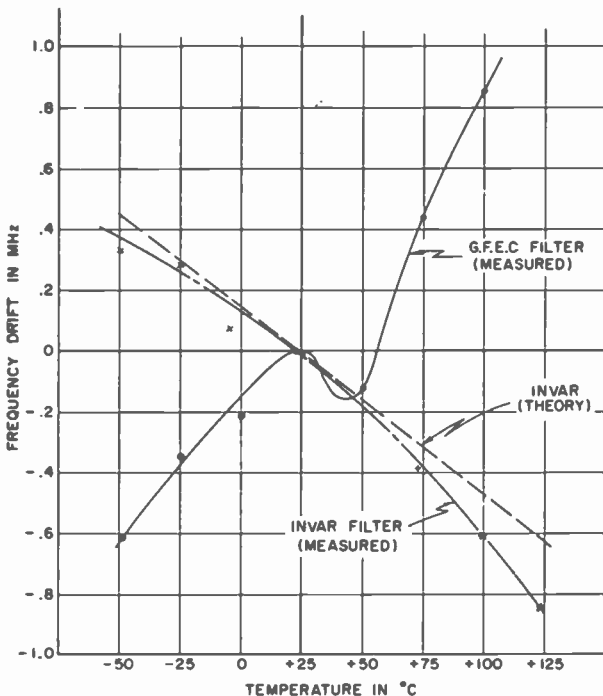


Fig. 11—Temperature versus frequency drift in a GFEC filter.

height waveguide is used in the output multiplexer to minimize output circuit losses.

The Invar multiplexer weights of Table 4 are based on selective spark erosion of the waveguide walls to a thickness of approximately 0.02 inch. A thickness of 0.050 inch is maintained in areas of high electric field intensity. The wall thickness of the GFEC filters is a uniform 0.050 inch.

The weight reduction of 35 lbs achieved through the use of GFEC filters was arrived at on the basis of actual weights of existing GFEC and Invar filters.

3.4 Subsystem Reliability

Adequate transponder reliability is achieved by two means. The first is the application of conventional one-for-one hardware redundancy. Substitution switching of individual units is not considered practical, since a point of diminishing returns is reached when the reliability

and performance of the switches themselves begin to limit the overall reliability and performance of the transponder. Grouping the components into larger functional blocks such as a broad-band front end also eases the problems of matching the performance of the transponder in all possible switched configurations.

Table 4—Weight Comparison of Invar and GFEC Multiplexers

UNIT	Qty.	Lightweight Invar		Graphite Fiber Composite	
		Unit Wt. (lb)	Total Wt. (lb)	Unit Wt. (lb)	Total Wt. (lb)
<u>Output Multiplexer</u>					
5-Section Filter	24	1.30	31.20	0.50	12.00
Input Isolators	24	0.085	2.04	0.085	2.04
Combining Manifold	4	1.10	4.40	1.10	4.40
Mounting Hardware	—	2.00	2.00	2.00	2.00
			39.64		20.44
<u>Input Multiplexer</u>					
9-Section Filter	24	1.25	30.00	0.535	12.85
Triplexing Manifold	8	0.40	3.20	0.40	3.20
Coax. Isolators	28	0.085	2.58	0.085	2.58
Coax. Circulator	4	0.085	0.34	0.085	0.34
3-dB Hybrid	2	0.10	0.20	0.10	0.20
Mounting Hardware	—	3.00	3.00	3.00	3.00
Interconnecting Coax	—	1.00	1.00	1.00	1.00
			40.32		23.17
Total			79.96		48.61

The second means of achieving system reliability concerns the output traveling-wave tubes, which are not redundant and effectively use frequency spectrum as protection instead of hardware redundancy. In the case of a 12-channel group it is possible in principle to provide one spare TWT that can be switched into any of the 12 positions; in practice this is not justified due to weight, reliability, and performance limitations of the resulting switching network. Any more-complex schemes such as 2 tubes protecting 12 is even more impractical. Experience has shown that the only reasonably practical means is a one for one, or possibly one for two, switching scheme. If we propose that any one channel of a 12-channel group be treated as spare and available to assume the function of any of the remaining eleven, then we have defined a very flexible and reliable model in which the survival of any 11 of the 12 channels constitutes complete success. The proba-

bility of complete success increases dramatically if we further assume that any 10 out of 12 constitutes success. The inference is made here that the use of a modest percentage of the available spectrum for channel protection is superior to the use of the extra weight that would be necessary to achieve the same system reliability by hardware redundancy.

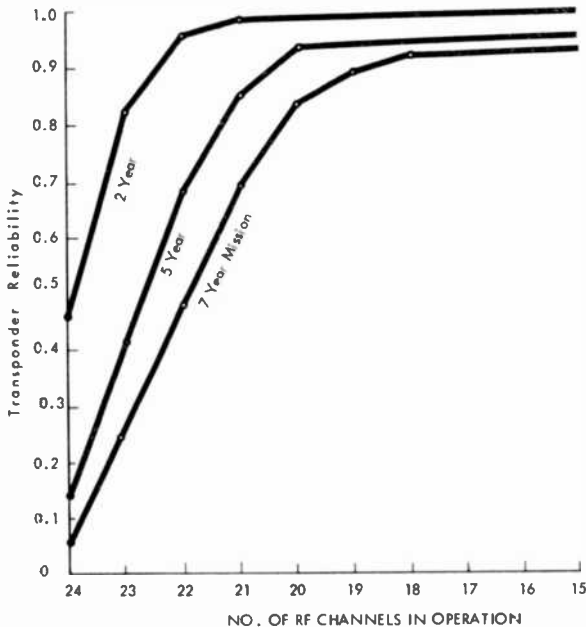


Fig. 12—Subsystem reliability as a function of operating channels.

Fig. 12 describes the reliability of the whole transponder as a function of the number of operating channels, with lifetime in years as a parameter. The failure rate of the output TWTA's, including EPC's, is assumed to be 1850 FIT. The failure rate of each passive component, such as isolators, band-pass filters, hybrids, and manifolds for input/output multiplexers, is assumed to be 10 FIT.

From these parametric curves, it can be concluded that the main limitation to successful operation of 19 or more channels over a period of 7 years is the reliability of the output TWTA's. For successful operation of a lesser number of channels over the same period, the limiting factor is the receiver-driver electronics.

4. Summary

The weight budget for the transponder is presented in Table 5. No allowance is made for either output TWTA thermal heat sinks or any power conditioning that may be necessary at the interface between the transponder and the telemetry and command subsystem.

Table 5--Weight Budget for 24-Channel Transponder

Unit	Wt (lb)	Qty	Total Wt (lb)
Input Filter	1.0	2	2.0
Receiver	9.0	2	18.0
Input Mux	5.8	4	23.2
TWTA	3.5	24	84.0
Output Mux	5.1	4	20.4
Output Filter	1.2	4	4.8
Output Isolator	0.85	4	3.4
Waveguide Harness and misc. hardware	6.0	1 set	6.0
Level-setting Attenuator	0.3	6	1.8
			<hr/> 163.6

The GFEC multiplexer filters and all-solid-state receiver-drivers are the main lightweight elements in the transponder. Chebyshev filters are used in the multiplexers since the synthesis, design, and manufacturing techniques for this type of filter are well established. The realization of elliptic function filters in a waveguide media has recently been demonstrated.⁵ This type of filter was considered as a candidate because it represented another area of potential weight reduction. The considerable development time that would be necessary, coupled with the additional complications inherent in a qualification program involving new design techniques in addition to new processes and materials, led to the decision not to use elliptic filters in the baseline transponder.

In addition to the reduced weight requirements of the all-solid-state receiver relative to those of the design incorporating a driver TWTA, the solid-state design results in an improved carrier to noise ratio and a reduced power drain, as shown in the transponder power budget of Table 6. The receiver trade-offs have been examined in detail and the main area of concern, namely, the long-term reliability of microwave transistor amplifiers, has been analyzed from both an optimistic and a pessimistic viewpoint. The impact of multipath effects on subsystem performance has also been dealt with, and it is shown that the multiplexer designs are sufficiently conservative to ensure adequate protection.

Table 6—Power Budget for 24-Channel Transponder

Unit	DC Input Power	Total Power per Transponder
Output TWTA*	17.50 watts	420 watts
Receiver	4.50 watts	9 watts
Total Power Requirements = 429 watts		
* TWTA Output Power:	5.00 watts	
TWT Efficiency:	35%	
EPC Efficiency:	81.5%	

Finally, a summary specification of transponder performance is presented in Table 7.

Table 7—Transponder Summary Specification

Number of RF Channels	24
Power per Channel	4.0 watts
Bandwidth	36 MHz
Configuration	All rf Single heterodyne
Noise Figure	7 dB
Input Signal (single carrier)	-90 dBw
Frequency and polarization plan	2 groups of 12 orthogonally polarized
Power	28 volts dc, 429 watts
Weight	163.6 lbs.

Acknowledgments

The authors wish to thank their colleagues for the assistance given them. They wish to thank N. Epstein for his excellent programming, H. Moody for his contribution to the trade-off study of the all-solid-state receiver-driver portion of the transponder, and G. Lo who provided the measured results on GFEC filters.

Appendix 1—Filter Requirements for a Domestic Satellite System

Input		Output	
<u>Isolation Requirements</u>		<u>Isolation Requirements</u>	
<u>Frequency</u>	<u>Attenuation</u>	<u>Frequency</u>	<u>Attenuation</u>
$f_o \pm 23$ MHz	20.0 dB min.	$f_o \pm 29$ MHz	6 dB min.
$f_o \pm 29$ MHz	45.0 dB min.	$f_o \pm 40$ MHz	18 dB min.

$f_o \pm 40$ MHz and beyond within the range 3700-4200 MHz 50.0 dB min.

$f_o \pm 63$ MHz and beyond within the range 3700-4200 MHz 40 dB min.

Gain Slope

Frequency	Input Gain Slope (dB/MHz)
$f_o \pm 10$ MHz	0.05
$f_o \pm 12$ MHz	0.13
$f_o \pm 14$ MHz	0.18
$f_o \pm 16$ MHz	0.22

Total Gain Slope

Frequency	Total Gain Slope (dB/MHz)
$f_o \pm 12$ MHz	0.20
$f_o \pm 14$ MHz	0.30
$f_o \pm 16$ MHz	0.40

Group Delay

Frequency	Input Group Delay Nanoseconds
$f_o \pm 8$ MHz	6
$f_o \pm 12$ MHz	13
$f_o \pm 16$ MHz	32
$f_o \pm 17$ MHz	44

Total Group Delay

Frequency	Total Group Delay Nanoseconds
$f_o \pm 8$ MHz	7
$f_o \pm 12$ MHz	15
$f_o \pm 16$ MHz	37
$f_o \pm 17$ MHz	51

Appendix 2—Filter Requirements for Intelsat IV

<u>Input</u>		<u>Output</u>	
<u>Isolation Requirements</u>		<u>Isolation Requirements</u>	
<u>Frequency</u>	<u>Attenuation</u>	<u>Frequency</u>	<u>Attenuation</u>
$f_o \pm 25$ MHz	30 dB min.	$f_o \pm 30$ MHz	15 dB min.
$f_o \pm 40$ MHz	50 dB min.	$f_o \pm 40$ MHz	30 dB min.
<u>Gain Slope</u>		<u>Gain Slope</u>	
<u>Frequency</u>	<u>Input Gain Slope (dB/MHz)</u>	<u>Frequency</u>	<u>Output Gain Slope (dB/MHz)</u>
70% of usable* Bandwidth	0.03	80% of usable Bandwidth	0.03
80% of usable Bandwidth	0.05	90% of usable Bandwidth	0.10
90% of usable Bandwidth	0.2	100% of usable Bandwidth	0.20
100% of usable Bandwidth	0.7		
<u>Group Delay</u>		<u>Group Delay</u>	
<u>Frequency</u>	<u>Input Group Delay Nanoseconds</u>	<u>Frequency</u>	<u>Output Group Delay Nanoseconds</u>
$f_o \pm 12$ MHz	1.1/-2.0	$f_o \pm 12$ MHz	6.0/-1.0
$f_o \pm 14$ MHz	3.3/-2.2	$f_o \pm 14$ MHz	8.8/-1.0
$f_o \pm 16$ MHz	14.0/-3.0	$f_o \pm 16$ MHz	13.9/-1.0
$f_o \pm 17$ MHz	26.0/-4.0	$f_o \pm 17$ MHz	17.8/-1.0
$f_o \pm 18$ MHz	50.0/-5.0	$f_o \pm 18$ MHz	20.0/-1.0

* Usable Bandwidth (BW) = 36 MHz

Appendix 3—Amplitude and Phase Response of Chebyshev Functions

The transfer function $Z_{12}(S)$ of any two-port electrical network can be represented by

$$Z_{12}(S) = \frac{H_o(S - S_1)(S - S_3) \dots (S - S_{2n-1})}{(S - S_2)(S - S_4) \dots (S - S_{2n})}$$

where S is the complex frequency variable, $S_1, S_3, \dots, S_{2n-1}$ are the zeros of the functions, S_2, S_4, \dots, S_{2n} are the poles of the function, and H_o is an arbitrary constant.

The amplitude response and its derivatives can be shown to be given by⁶

$$\begin{aligned} \alpha &= 20 \log_{10} e [\ln |S - S_2| + \ln |S - S_4| + \dots + \ln |S - S_{2n}| \\ &\quad - \ln |S - S_1| - \ln |S - S_3| - \dots - \ln |S - S_{2n-1}|] \\ &\quad - 20 \log_{10} e \cdot H_o \text{ in dB} \end{aligned}$$

$$\frac{d\alpha}{d\omega} = 20 \log_{10} e \left[\sum_{\text{poles}} \frac{\omega - \omega_K}{|S - S_K|^2} - \sum_{\text{zeros}} \frac{\omega - \omega_K}{|S - S_K|^2} \right] \text{ dB/rad}$$

$$\begin{aligned} \frac{d^2\alpha}{d\omega^2} &= 20 \log_{10} e \left[\sum_{\text{poles}} \left(\frac{1}{|S - S_K|^2} - 2 \frac{(\omega - \omega_K)^2}{|S - S_K|^4} \right) \right. \\ &\quad \left. - \sum_{\text{zeros}} \left(\frac{1}{|S - S_K|^2} - 2 \frac{(\omega - \omega_K)^2}{|S - S_K|^4} \right) \right] \end{aligned}$$

$$\begin{aligned} \frac{d^3\alpha}{d\omega^3} &= 20 \log_{10} e \left[\sum_{\text{poles}} \left(8 \frac{(\omega - \omega_K)^3}{|S - S_K|^6} - 6 \frac{(\omega - \omega_K)}{|S - S_K|^4} \right) \right. \\ &\quad \left. - \sum_{\text{zeros}} \left(8 \frac{(\omega - \omega_K)^3}{|S - S_K|^6} - 6 \frac{(\omega - \omega_K)}{|S - S_K|^4} \right) \right] \end{aligned}$$

$$\begin{aligned} \frac{d^4\alpha}{d\omega^4} &= 20 \log_{10} e \left[\sum_{\text{poles}} \left(-\frac{6}{|S - S_K|^4} + 48 \frac{(\omega - \omega_K)^2}{|S - S_K|^6} - 48 \frac{(\omega - \omega_K)^4}{|S - S_K|^8} \right) \right. \\ &\quad \left. - \left[\sum_{\text{zeros}} \left(-\frac{6}{|S - S_K|^4} + 48 \frac{(\omega - \omega_K)^2}{|S - S_K|^6} - 48 \frac{(\omega - \omega_K)^4}{|S - S_K|^8} \right) \right] \right] \end{aligned}$$

Where α is the insertion loss in dB,

$$S_K = \sigma_K + \hat{j}\omega_K, \hat{j} = \sqrt{-1}$$

represents a pole if K is even and a zero if K is odd,

$$|S - S_K| = [\sigma_K^2 + (\omega - \omega_K)^2]^{1/2}$$

since the function is evaluated at real frequencies, i.e., at $S = \hat{j}\omega$.

Similarly, it can be shown that the phase response and its derivatives are given by

$$\begin{aligned} \beta(\omega) &= \sum_{\text{poles}} \tan^{-1} \frac{\omega - \omega_K}{\sigma_K} - \sum_{\text{zeros}} \tan^{-1} \frac{\omega - \omega_K}{\sigma_K} \\ \frac{d\beta}{d\omega} &= \sum_{\text{poles}} \frac{\sigma_K}{\sigma_K^2 + (\omega - \omega_K)^2} - \sum_{\text{zeros}} \frac{\sigma_K}{\sigma_K^2 + (\omega - \omega_K)^2} \\ \frac{d^2\beta}{d\omega^2} &= \sum_{\text{zeros}} 2\tau_K^2 \tan \beta_K - \sum_{\text{poles}} 2\tau_K^2 \tan \beta_K \\ \frac{d^3\beta}{d\omega^3} &= \sum_{\text{zeros}} 2\tau_K^3 (3 \tan^2 \beta_K - 1) - \sum_{\text{poles}} 2\tau_K^3 (3 \tan^2 \beta_K - 1) \\ \frac{d^4\beta}{d\omega^4} &= \sum_{\text{zeros}} 24\tau_K^4 \tan \beta_K (\tan^2 \beta_K - 1) \\ &\quad - \sum_{\text{poles}} 24\tau_K^4 \tan \beta_K (\tan^2 \beta_K - 1) \\ \frac{d^5\beta}{d\omega^5} &= \sum_{\text{zeros}} 24\tau_K^5 (5 \tan^4 \beta_K - 10 \tan^2 \beta_K + 1) \\ &\quad - \sum_{\text{poles}} 24\tau_K^5 (5 \tan^4 \beta_K - 10 \tan^2 \beta_K + 1) \end{aligned}$$

where β is the phase angle in radians and τ_K is the group delay in seconds,

$$\tau_K = - \frac{d\beta_K}{d\omega} = \sum_{\text{zeros}} \frac{\sigma_K}{\sigma_K^2 + (\omega - \omega_K)^2} - \sum_{\text{poles}} \frac{\sigma_K}{\sigma_K^2 + (\omega - \omega_K)^2}$$

For a Chebyshev type of filter response, the poles are given by

$$S_K = -\sinh \left[\frac{1}{n} \sinh^{-1} \frac{1}{\epsilon} \right] \sin \left(\frac{2K-1}{n} \frac{\pi}{2} \right) \\ + j \cosh \left[\frac{1}{n} \sinh^{-1} \frac{1}{\epsilon} \right] \cos \left(\frac{2K-1}{n} \frac{\pi}{2} \right)$$

where n = number of sections in the filter,

$$\epsilon^{-1} = \sqrt{\rho^{-2} - 1},$$

ρ = maximum reflection coefficient of the equi-ripple pass band.

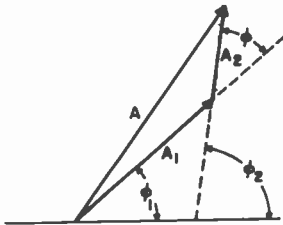


Fig. 13—Vector representation of two coherent signals at output of microwave repeater.

Appendix 4—Multipath Effects

The vector representation of two coherent signals at the output of the microwave repeater is shown in Fig. 13. From the figure,

A_1 is the amplitude of the main signal

A_2 is the amplitude of the interfering signal

A is the amplitude of the resultant signal

ϕ_1 is the phase of the main signal

ϕ_2 is the phase of the interfering signal,

ϕ is the phase of the resultant signal.

$$A^2 = A_1^2 + A_2^2 + 2A_1A_2 \cos \phi.$$

Taking the first, second, and third derivatives with respect to ω and rearranging the terms gives,

$$\frac{dA}{d\omega} = \frac{1}{A} \left[\frac{dA_1}{d\omega} (A_1 + A_1 \cos \phi) + \frac{dA_2}{d\omega} (A_2 + A_1 \cos \phi) \right. \\ \left. - A_1 A_2 \sin \phi \cdot \frac{d\phi}{d\omega} \right]$$

$$A \frac{d^2 A}{d\omega^2} = - \left(\frac{dA}{d\omega} \right)^2 + \left(\frac{dA_1}{d\omega} \right)^2 + \left(\frac{dA_2}{d\omega} \right)^2 \\ + \frac{d^2 A_1}{d\omega^2} (A_1 + A_2 \cos \phi) + \frac{d^2 A_2}{d\omega^2} (A_2 + A_1 \cos \phi) \\ + 2 \cos \phi \cdot \frac{dA_1}{d\omega} \frac{dA_2}{d\omega} \\ - 2 \sin \phi \cdot \frac{d\phi}{d\omega} \left(A_2 \frac{dA_1}{d\omega} + A_1 \frac{dA_2}{d\omega} \right) \\ - A_1 A_2 \left[\frac{d^2 \phi}{d\omega^2} \sin \phi + \cos \phi \cdot \left(\frac{d\phi}{d\omega} \right)^2 \right]$$

$$A \frac{d^3 A}{d\omega^3} = -3 \left(\frac{dA}{d\omega} \frac{d^2 A}{d\omega^2} - \frac{dA_1}{d\omega} \frac{d^2 A_1}{d\omega^2} - \frac{dA_2}{d\omega} \frac{d^2 A_2}{d\omega^2} \right) \\ + A_1 \frac{d^3 A_1}{d\omega^3} + A_2 \frac{d^3 A_2}{d\omega^3} + \cos \phi \left(A_2 \frac{d^3 A_1}{d\omega^3} \right. \\ \left. + A_1 \frac{d^3 A_2}{d\omega^3} + 3 \frac{dA_1}{d\omega} \frac{d^2 A_2}{d\omega^2} \right. \\ \left. + 3 \frac{dA_2}{d\omega} \frac{d^2 A_1}{d\omega^2} \right) - 3 \sin \phi \cdot \frac{d\phi}{d\omega} \left(A_2 \frac{dA_1}{d\omega} \right. \\ \left. + A_1 \frac{d^2 A_2}{d\omega^2} + 2 \frac{dA_1}{d\omega} \frac{dA_2}{d\omega} \right) - A_1 A_2 \left(\frac{d^3 \phi}{d\omega^3} \sin \phi \right. \\ \left. + 3 \cos \phi \frac{d\phi}{d\omega} \frac{d^2 \phi}{d\omega^2} - \frac{d^3 \phi}{d\phi^3} \sin \phi \right)$$

$$-3 \left[A_1 \frac{dA_2}{d\omega} + A_2 \frac{dA_1}{d\omega} \right] \left[\frac{d^2\phi}{d\omega^2} \sin \phi + \left(\frac{d\phi}{d\omega} \right)^2 \cos \phi \right]$$

If A represents the amplitude in volts and if we assume 1 volt as our reference, then the amplitude response is

$$\begin{aligned} \alpha &= 20 \log_{10} A \text{ in dB} \\ &= 20 \log_{10} e \ln A \text{ in dB.} \end{aligned}$$

For resultant phase and derivatives

$$\phi = \tan^{-1} \left(\frac{A_2 \sin \phi}{A_1 + A_2 \cos \phi} \right) + \phi_1.$$

Defining $A_2/A_1 = p$, the first derivative of ϕ is

$$\frac{d\phi}{d\omega} = \left[\frac{p^2 \frac{d\phi}{d\omega} + p \frac{d\phi}{d\omega} + \frac{dp}{d\omega} \sin \phi}{1 + p^2 + 2p \cos \phi} \right] + \frac{d\phi_1}{d\omega}.$$

Differentiating with respect to ω again

$$\begin{aligned} \frac{d^2\phi}{d\omega^2} &= (p + \cos \phi) \left(2 \frac{d\phi}{d\omega} \frac{dp}{d\omega} + p \frac{d^2\phi}{d\omega^2} \right) \\ &+ \sin \phi \cdot \left(\frac{d^2p}{d\omega^2} - p \left(\frac{d\phi}{d\omega} \right)^2 \right) (1 + p^2 + 2p \cos \phi)^{-1}. \end{aligned}$$

Similarly, higher derivatives of resultant phase can be determined.

Appendix 5—Sample Calculation of Intermodulation Distortion

Intermodulation noise is computed here for 900 telephone channels multiplexed on a single rf carrier. The assumptions made for this computation⁹ are:

Baseband: 0.564 – 4.532 MHz

Peak Factor: 12 dB

Pre-emphasis (P.E.): 4.0 dB

Weighting Advantage (W): 2.5 dB

Average Talker Power: -16 dBmO

The effective signal to noise ratio in the top baseband channel is given by

$$\frac{S}{N} = \text{NPR} + \text{BWR} - \text{NLR} + \text{P.E.} + \text{W}$$

$$\text{Where Bandwidth Ratio (BWR)} = 10 \log_{10} \left(\frac{4.532}{3.1} \right)$$

$$\text{Noise Load Ratio (NLR)} = -16 + 10 \log_{10} 900$$

For the design considered in this paper, only the second-order group delay coefficient contributes significantly to intermodulation distortion. The noise power ratio (NPR) due to this component is given by⁴

$$\text{NPR} = 10 \log_{10} \frac{7.5 \times 10^5}{\pi^2 B_2^2 \sigma^4 f_m^2}$$

where f_m is the maximum modulating frequency in MHz,

σ is the multi-channel rms frequency deviation in MHz,

B_2 is the 2nd order group delay coefficient in nsec/MHz²

For the present design,

$$f_m = 4.532 \text{ MHz}$$

$B_2 \approx .1$ over the band containing 99.9% of signal energy,

$\sigma = 3.13$ MHz for a 12-dB peak factor.

Therefore

$$\frac{S}{N} = 60.46 \text{ dB}$$

$$\text{Noise in picowatts} = \text{Antilog} \frac{(90-S/N)}{10}$$

$$= 900$$

In addition, intermodulation distortion is also caused by conversion of AM to PM by the output TWT's. The NPR for second-order group delay followed by AM to PM conversion is given by⁴

$$\text{NPR} = \frac{4.3 \times 10^7}{\pi^2 K_{po}^2 B_2^2 \sigma^2 f_m^2}$$

Where K_{po} is the AM to PM transfer coefficient of the TWT in degrees/dB. Assuming that B_2 is essentially the same as 0.1 nsec/MHz² at the TWT input,

$$\text{NPR} = 44.38 \text{ dB for } K_{po} = 2^\circ/\text{dB}$$

$$\text{and } \frac{S}{N} = 68.98 \text{ dB}$$

$$= 126 \text{ picowatts}$$

Any compensation of the second-order group delay on ground can substantially cut down this 1026 picowatts of intermodulation noise in the satellite.

If a TV signal is passed through the above rf channel, the differential phase (DP) owing to the second-order group delay component is given by⁵

$$\text{DP} = B_2(\Delta f)^2 f_s 2\pi \times 10^{-3} \times \frac{360}{2\pi} \text{ degrees,}$$

where B_2 is the second-order group delay coefficient in nsec/MHz²

Δf is the frequency separation from band center in MHz

f_s is the search frequency in MHz

For the present design, we shall assume

$f_s = 3.58$ MHz (baseband frequency of color subcarrier).

Therefore, $DP = 0.129 (\Delta f)^2$ degrees

$= 2.06$ degrees for $\Delta f = 4$ MHz.

References:

¹ M. Barmat, "Domestic Satellites Promise Major Communications Advance," *Telecommunications*, p. 36, Nov. 1971.

² J. E. Keigler, W. J. Lindorfer, and L. Muhlfelder, "Stabilite Attitude Control for Synchronous Communications Satellite," AIAA 4th Communications Satellite Systems Conf., Wash., D. C., April 24-26, 1972.

³ AT & T Application for a Domestic Communications Satellite System Submitted to Federal Communications Commission, Wash., D. C., March 3, 1971.

⁴ G. J. Garrison, "Intermodulation Distortion in Frequency-Division Multiplex FM Systems—A Tutorial Summary," *IEEE Trans. Communication Tech.*, Vol. COM-16, No. 2, April 1968.

⁵ A. E. Atia and A. E. Williams, "New Types of Waveguide Bandpass Filters for Satellite Transponders," *COMSAT Tech. Rev.*, Vol. 1, No. 1, p. 21, Fall 1971.

⁶ C. M. Kudsia and M. V. O'Donovan, *Microwave Filters for Communication Systems*, Book to be published by Artech House Inc. in October 1973.

Recent Papers by RCA Authors

Listing is alphabetical by name of publication. For copies of reprints the reader should contact the publication directly.

- A. Akselrad, "Detection of Magnetic Imperfections in Thin Films of Uniaxial Garnets," **AIP Conf. Proc. on Magnetism and Magnetic Materials**, No. 10, p. 408, 1973.
- J. J. Hanak and J. I. Gittleman, "Iron-Nickel-Silica Ferromagnetic Cermets," **AIP Conf. Proc. on Magnetism and Magnetic Materials**, No. 10, p. 961, 1973.
- S. Larach and R. E. Shrader, "Cathode-Ray Excited Emission Spectrometry of Trace Rare Earths in Yttrium Oxide via Yttrium Oxysulfide Conversion," **Analytica Chimica Acta**, Vol. 63, p. 459, 1973.
- F. J. Hughes, Jr., "Application of Optimal Control Techniques to a Dual-Spin Spacecraft Incorporating Flexible Appendages," BS/MS Thesis for MIT.
- A. H. Firester, "Properties and Fabrication of Micro Fresnel Zone Plates," **Appl. Opt.**, Vol. 12, p. 1698, Aug. 1973.
- J. M. Hammer, D. J. Channin, and M. T. Duffy, "Fast Electro-Optic Waveguide Deflector Modulator," **Appl. Phys. Lett.**, Vol. 23, p. 176, 15 Aug. 1973.
- H. Kressel and J. Ladany, "Photocurrent Measurements on GaP:N Green Light Emitting Diodes," **Appl. Phys. Lett.**, Vol. 22, p. 224, March 1, 1973.
- G. D. Cody and G. W. Cullen, "Longitudinal and Transverse Critical Currents of Chemically Deposited Nb₃Sn in the Temperature Range of 14.5°K to 17.5°K," **Appl. Phys., J. of**, Vol. 44, p. 2843, June 1973.
- G. W. Cullen and G. D. Cody, "Field, Angular, and Defect Dependence of the Critical Current of Nb₃Sn for $t \leq 4.2^\circ\text{K}$," **Appl. Phys., J. of**, Vol. 44, p. 2838, June 1973.
- M. Ettenberg, H. Kressel, and S. L. Gilbert, "Minority Carrier Diffusion Length and Recombination Lifetime in GaAs:Ge Prepared by Liquid-Phase Epitaxy," **Appl. Phys., J. of**, Vol. 44, p. 827, Feb. 1973.
- A. C. Ipri and J. N. Zemel, "Impurity Centers in Silicon Films on Sapphire," **Appl. Phys., J. of**, Vol. 44, p. 744, Feb. 1973.
- H. Kressel, C. J. Nuese, and J. Ladany, "Luminescence from In_{0.8}Ga_{0.2}P Prepared by Vapor-Phase Epitaxy," **Appl. Phys., J. of**, Vol. 44, p. 3266, July 1973.
- W. Rehwald, "Anomalous Ultrasonic Attenuation in Be₁₂GeO₂₀, Bi₁₂SiO₂₀, and Bi₁₂(Ge_{0.5}Si_{0.5})O₂₀," **Appl. Phys., J. of**, Vol. 44, p. 3017, July 1973.
- A. Rothwarf, "Plasmon Theory of Electron-Hole Pair Production: Efficiency of Cathode-Ray Phosphors," **Appl. Phys., J. of**, Vol. 44, p. 752, 1973.
- R. O. Winder, "A Data Base for Computer Performance Evaluation," **Computer**, Vol. 6, p. 25, March 1973.
- C. Wronski, "Charge Transport in Sb₂S₃ Evaporated Films," **Electrets Charge Storage and Transport in Dielectrics**, p. 382, 1973.
- B. R. Schwartz, "Interconnections," **Electromechanical Design**, April 1973.
- M. T. Duffy, C. C. Wang, G. D. O'Clock, Jr., S. H. McFarlane III, and P. J. Zanzucchi, "Epitaxial Growth and Piezoelectric Properties of AlN, GaN, GaAs on Sapphire or Spinel," **Electronic Materials, J. of**, Vol. 2, p. 259, 1973.
- R. Feryska, J. O. Preisig, and E. D. Menkes, "COS/MOS Phase Comparator," **IEEE Intl. Solid-State Circuits Conf. Proc.**, p. 184, Feb. 16, 1973.

- A. S. Clorfeine, "Driving Under the Influence of Electronics," *IEEE Spectrum*, Vol. 10, p. 32, May 1973.
- J. Shefer and R. J. Klensch, "Harmonic Radar Helps Autos Avoid Collisions," *IEEE Spectrum*, Vol. 10, p. 38, May 1973.
- H. Urkowitz, "The Effect of Limiting Upon the Mean Cross Section of Lognormal Radar Clutter," *IEEE Trans. Aerospace and Electronic Systems*, Vol. 19, March 1973.
- A. Waksberg, "FM Laser Noise Effects on Optical Doppler Radar Systems," *IEEE Trans. Aerospace and Electronic Systems*, Vol. AES-8, Nov. 1972.
- C. V. Greenman, "A Simple Analytical Model for the Envelope Distribution of Sinusoidal Carrier in Atmospheric Radio Noise," *IEEE Trans. Comm. Technology*, Vol. COM-21, p. 254, March 1973.
- D. Hampel, "Design of Multi-Function Threshold Gates," *IEEE Trans. on Computers*, March 1973.
- H. Huang, "A Modified GaAs IMPATT Structure for High-Efficiency Operation," *IEEE Trans. Electron Devices*, Vol. ED-20, p. 482, May 1973.
- K. P. Weller, "A Study of Millimeter-Wave GaAs IMPATT Oscillator and Amplifier Noise," *IEEE Trans. Electron Devices*, Vol. ED-20, p. 317, June 1973.
- P. Bura, "MIC Ku Band Upconverter," *IEEE Trans. Microwave Theory and Tech.*, March 1973.
- K. Suzuki, R. Hirota, and K. Yoshikawa, "Amplitude-Modulated Soliton Trains and Coding-Decoding Applications," *Int. J. Electronics*, Vol. 34, p. 777, 1973.
- K. Suzuki, R. Hirota and K. Yoshikawa, "The Properties of Phase Modulated Soliton Trains," *Japanese J. Appl. Phys.*, Vol. 12, p. 361, March 1973.
- H. Kressel, H. Schade and H. Nelson, "Heterojunction Cold-Cathode Electron Emitters of (AlGa)As-GaAs," *Luminescence, J. of*, Vol. 7, p. 146, 1973.
- J. I. Pankove, "Luminescence in GaN," *Luminescence, J. of*, Vol. 7, p. 114, 1973.
- J. I. Pankove, E. A. Miller, and J. E. Berkeyheiser, "Electroluminescence in GaN," *Lumin. of Crystals, Molecules, and Solutions*, Plenum Pub. Corp., NY, NY.
- R. Hirota, "Exact Envelope-Solutions of a Nonlinear Wave Equation," *Mathematical Phys., J. of*, Vol. 14, p. 805, July 1973.
- R. Hirota, "Exact N-Soliton Solutions of the Wave Equation of Long Waves in Shallow-Water and in Nonlinear Lattices," *Mathematical Phys., J. of*, Vol. 14, p. 810, July 1973.
- D. Meyerhofer and E. F. Pasierb, "Light Scattering Characteristics in Liquid Crystal Storage Materials," *Mol. Cryst. and Liquid Cryst.*, Vol. 20, p. 279, 1973.
- A. H. Firester, D. M. Hoffman, E. A. James, and M. E. Heller, "Fabrication of Planar Optical Phase Elements," *Optics Commun.*, Vol. 8, p. 160, June 1973.
- D. A. deWolf, "Angle-of-Arrival Difference Spectrum of a Simple Interferometer in Turbulent Air," *Optical Soc. of America, J. of*, Vol. 63, p. 657, June 1973.
- H. Kiess and T. Freund, "Charge Transfer of Absorbed Ozone," *Phys. Chem., J. of*, Vol. 77, p. 556, Feb. 15, 1973.
- D. Redfield, "Observation of Log on $T^{-1/2}$ in Three Dimensional Energy-Band Tails," *Phys. Rev. Lett.*, Vol. 30, p. 1319, June 1973.
- E. S. Sabisky and C. H. Anderson, "Onset for Superfluid Flow in He⁴ Films on a Variety of Substrates," *Phys. Rev. Lett.*, Vol. 30, p. 1122, May 1973.
- P. Sheng, B. Abeles, and Y. Arie, "Hopping Conductivity in Granular Metals," *Phys. Rev. Lett.*, Vol. 31, p. 44, July 1973.
- R. Gelck, E. F. Steigmeier, and H. Auderset, "Raman Effect in Selenium-Tellurium Mixed Crystals," *Physica Status Solidi (b)* 54, p. 623, 1972.
- V. S. Ban and M. Ettenberg, "Mass Spectrometric and Thermodynamic Studies of Vapor-Phase Growth of In_{(1-x)Ga_xP}," *Phys. and Chem. of Solids, J. of*, Vol. 34, p. 1119, 1973.
- T. Takahashi, S. Osaka, and O. Yamada, "Crystallographic and Optical Properties of Rare-Earth Chromium Sulfides RCrS₂," *Phys. and Chem. of Solids, J. of*, Vol. 34, p. 113, 1973.
- M. Bosch, W. Kanzig, and E. F. Steigmeier, "Molekul-und Gitterschwingungen im Natriumhyperoxid," *Physik der kondensierten Materie*, Vol. 16, p. 107, 1973.
- N. Feldstein, "Reliability in Printed Circuitry Metallization—A Case for Improved Catalyzing Systems," *Plating*, Vol. 60, June 1973.
- K. G. Hernqvist, "CW Metal-Vapor Lasers," *Proc. of the First European Electro-Optics Markets and Technology Conf.*, p. 94.
- W. J. Merz, "Ferroelectricity and Its Applications," *Proc. of 2nd European Solid State Device Research Conf.*, p. 3, 1972.
- K. Sadashige, "Selected Topics on Modern Magnetic Video Recording Technology," *Proc. of the Inst. of Electronic and Radio Engineers*.
- H. Kressel, H. F. Lockwood, F. H. Nicoll, and M. Ettenberg, "Spontaneous and Stimulated Recombination in p+n-n+p (AlGa)As-GaAs Heterojunction Laser Diodes," *Quantum Electronics, J. of*, Vol. QE-9, p. 383, Feb. 1973.
- R. W. Bernal, "J-K Bistable Multivibrator," *RCA Technical Note*, May 1, 1973.
- T. Takahashi and O. Yamada, "Crystallographic and Magnetic Properties of the Cd(OH)₂ Layer Structure Compound TiS₂ Containing Extra Iron," *Solid State Chem., J. of*, Vol. 7, p. 25, 1973.

- W. Czaja, L. Krausbauer, B. J. Curtis, and P. J. Dean, "The 7-line Luminescence Spectrum of (Neh) in GaP:N, a Correction," **Solid State Commun.**, Vol. 12, p. 807, 1973.
- E. F. Steigmeier, H. Auderset, and G. Harbeke, "Critical Opalescence in SrTiO₃," **Solid State Commun.**, Vol. 12, p. 1077, 1973.
- J. J. Tietjen, R. E. Enstrom, V. S. Ban and D. Richman, "Vapor-Phase Growth of Several III-V Compound Semiconductors," **Solid State Technol.**, Vol. 15 p. 42, Oct. 1972.
- G. T. Tseng, "Constant and Variable Amplitude Limit Cycles in Dual-Spin Spacecraft," **Spacecraft and Rockets, J. of**, Nov. 1972.
- C. H. Anderson and E. S. Sabisky, "Acoustic Phonon Spectroscopy," **Surface Science**, Vol. 37, p. 914, June 1973.
- H. R. Brunner and B. J. Curtis, "The Vapour Pressures of Several Metal-2,2,6,6-Tetramethyl-3,5-Heptanedione Complexes Measured by a Knudsen Effusion Method," **Thermal Analysis, J. of**, Vol. 5, p. 111, 1973.
- J. J. O'Neill and J. L. Vossen, "Cr-Cu and Cr-Cu-Cr Thin Film Metallization," **Vacuum Science and Technol., J. of**, Vol. 10, p. 533, July/Aug. 1973.

Patents Issued to RCA Inventors

April

- R. L. Barbin** Magnetic Beam Adjusting Arrangements (3,725,831)
H. R. Beelitz Voltage Driver Circuit (3,725,801)
M. Caulton Semiconductor Assembly (3,728,589)
W. J. Davis Simultaneous Digital Transmission in Both Directions Over One Line (3,725,582)
S. S. Eaton, Jr. Phase Shift Oscillators Using Insulated-Gate Field-Effect Transistors (3,725,822)
G. R. Fadner, Jr. Method for Making a Kinescope Comprising a Color Selection Mask with Temporary Corridors (3,725,065)
G. D. Hanchett Switching Circuits (3,727,080)
W. A. Heibig, Sr. Computer Input-Output Chaining System (3,728,682)
G. V. Jacoby and G. J. Meslener Digital Signal Decoder Using Two Reference Waves (3,728,716)
C. F. Madrazo and R. G. Saenz Input Circuit for Multiple Emitter Transistor (3,727,072)
D. R. Melrose and D. S. Binge Suspension System (3,727,865)
T. E. Nolan High Power Laser System (3,725,822)
R. L. Pryor Carry Skip-Ahead Network (3,728,532)
C. L. Sachtleben and E. H. Steiner Web Transport (3,724,734)
J. R. Sandercock Stabilized Multipass Interferometer (3,729,261)
R. A. Sunshine Gate Protective Device for Insulated Gate Field-Effect Transistors (3,728,591)
A. W. Thomas, J. M. S. Neilson, and L. S. Greenberg Integral Thyristor-Rectifier Device (3,727,116)
P. K. Weimer Signal Transfer System for Panel Image Sensor (3,728,555)
J. A. Welsbecker Computer Memory with Improved Next Word Accessing (3,728,686)
K. P. Weller and C. P. Wen Method of Making Semiconductor Devices Mounted on a Heat Sink (3,728,236)
W. M. Yim and P. N. Yocom Electroluminescent Device Comprising a Transition Metal Oxide Doped with a Trivalent Rare Earth Element (3,728,594)
J. M. Yongue Common Base Amplifier Terminating Circuit for High Impedance Detecting Apparatus (3,725,577)

May

- G. A. Alphonse** Apparatus for Efficiently Converting Acoustic Energy into Electrical Energy (3,736,533)
C. H. Anderson and B. R. Feingold Maser Incorporating Crystal Having F-Centers (3,736,518)
L. R. Avery Vertical Deflection Circuits Utilizing Both Regenerative and Degenerative Feedback for Generating Voltages (3,735,192)
D. M. Baugher and K. W. Awkward Switching Regulator Overload Protection Circuit (3,736,469)
J. J. Brandinger Television Camera System with Enhanced Frequency Response (3,735,033)
R. E. Busch Method for Dicing Materials Having a Hexagonal Crystal Structure (3,731,861)
R. L. Buttle and W. D. Bailey Electronic Device Package (3,730,969)

D. J. Channin and J. M. Hammer Unitized Internally-Modulated Gas Laser (3,736,525)
G. W. Cullen, S. R. Bolin, A. D. Morrison, and C. C. Wang Czochralski-Grown Spinel for Use as Expitaxial Silicon Substrate (3,736,158)
P. Debruyne Vibrating Web Transport Apparatus (3,731,317)
W. F. Gehweiler Two Phase Logic Circuit (3,731,114)
J. Gross and W. H. Barkow Color Television Deflection Yoke Having Reduced Variation in Beam Trio Distortion (3,735,299)
P. E. Haferl Video Signal Processing Stage Which Performs Plural Functions (3,736,378)
J. J. Hanak and J. P. Russell Sputter-Etching Technique for Recording-Holograms or Other Fine-Detail Relief Patterns in Hard Durable Materials (3,733,258)
L. A. Harwood Automatic Chroma Control Circuits (3,732,358)
K. G. Hernqvist and D. C. Pultorak Method for Fabricating a Gas Laser Tube (3,730,606)
I. H. Kalish and H. Khajezadeh Zener Diode for Monolithic Integrated Circuits (3,735,210)
G. S. Kaplan and J. Shefer Electronic Fence Vehicle Locator Transmitter and System Using Same (3,735,299)
N. S. Klein Microwave Semiconductor Device Assembly (3,731,160)
E. Lachocki Energy Pump Voltage Regulator (3,736,496)
H. B. Law Method and Article for Color Kinescope Screen and Mask Production (3,730,719)
R. L. Loper Means for Superimposing a Marker Signal Onto a Composite Video Signal (3,735,038)
L. S. Napoli Balanced Mixer (3,735,267)
L. S. Napoli and J. J. Hughes Frequency Translator Circuit (3,731,180)
P. E. Norris and F. B. Micheletti Method of Making an MOS Transistor Including a Gate Insulator Layer of Aluminum Oxide and the Article so Produced (3,735,482)
R. Peter Dynamic Convergence Circuits (3,735,191)
D. H. Pritchard and W. E. Sepp Television Camera System with a Sinusoidally Varing Indexing Signal (3,735,038)
A. E. Roswell and G. K. Clymer Thermal Fatigue Lead-Soldered Semiconductor Device (3,735,208)
R. F. Sanford Grounded Faceplate Kinescope System (3,730,969)
J. R. Thompson and R. L. Schoenbeck Channel Monitoring System (3,733,430)
L. J. Thorpe Differential Amplifier (3,733,559)
D. R. Tshudy Electrophoretic Deposition of Powered Material on an Insulating Support (3,734,847)
H. S. Veloric Radio Frequency Transistor Employing High and Low-Conductivity Base Grids (3,736,478)
J. L. Vossen and J. J. O'Neill Thermographic Print Head and Method of Making Same (3,736,406)
J. P. Watson Document Picker (3,735,976)
O. M. Woodward Multifrequency Antenna System Including an Isolation Section Open Circuited at Both Ends (3,735,413)
C. M. Wright Conversion of Base B Number to Base R Number, Where R is a Variable (3,736,412)

June

A. A. A. Ahmed Triggered Flip-Flop (3,737,682)
R. D. Altmanshofer Amplitude Control Circuits (3,742,126)
H. Amemiya Differential Amplifier (3,737,797)
S. R. Bolin Modified Czochralski Grown Spinel Substrate by Solid State Diffusion (3,740,261)
J. D. Callaghan Antenna Structures (3,739,388)
J. D. Callaghan and R. M. Wilson Adapter for Coaxial Cable Connector (3,740,453)
D. R. Carley Transistor Employing Variable Resistance Ballasting Means Dependent on the Magnitude of the Emitter Current (3,740,621)
W. F. W. Dietz Voltage Supplies (3,740,474)
H. J. Digneffe Protective Switching Circuit for Providing Power to a Load From an Alternating Current Source Having Peak-to-Peak Excursions Within or Above a Given Range (3,742,337)
D. P. Dorsey Television Frame Storage Apparatus (3,740,465)
F. S. Easter Transformer Coupled Switching Regulator (3,740,639)
S. S. Eaton, Jr. Frequency Divider (3,742,248)
W. V. Fitzgerald, Jr. Width Control Circuit for a Television Receiver (3,740,472)
J. T. Gorman Bus Bar with Integral Terminals (3,740,693)

- I. Gorog and F. W. Spong** Holographic Recording System for Large Objects (3,740,111)
- L. A. Harwood** Electronic Signal Processing Circuit (3,740,456)
- L. A. Harwood** Detector Circuits with Self-Referenced Bias (3,740,461)
- L. A. Harwood** Automatic Chroma Gain Control System (3,740,462)
- R. C. Heuner, S. J. Niemiec, and D. K. Morgan** Liquid Crystal Display (3,740,717)
- M. R. Horton and R. S. Kutay** Fabrication Method for Gas Lasers Having Integral Mirrors (3,740,110)
- S. W. Kessler, Jr.** Transcendent Semiconductor Device (3,739,235)
- I. Kudman and C. M. Schmelz** Protected Thermoelectric Elements and Method of Protecting Same (3,737,345)
- A. Laker** Method of Making a Semiconductor Device (3,738,880)
- N. L. Lindburg, R. A. Bonnette, and T. E. Deegan** Numerical Display Device Having Filamentary Light Sources (3,737,706)
- H. F. Lockwood and M. Eltenberg** Method of Depositing an Epitaxial Semiconductor Layer From the Liquid Phase (3,741,825)
- J. T. Mark** Single Bore Tube Gas Laser (3,739,297)
- J. H. McCusker and S. S. Perlman** Power Control System Employing Piezo-Ferroelectric Devices (3,740,582)
- L. P. Nahay** M-Ary FSK Digital Modulator (3,740,669)
- J. I. Pankove and P. E. Norris** Electroluminescent Semiconductor Device for Generating Ultra Violet Radiation (3,740,622)
- R. B. Platt and B. B. McCue** Method for Separating Chemically-Oxidizable Phosphor Particles from Mixtures with Essentially Nonoxidizable Phosphor Particles (3,740,342)
- A. Presser** Semiconductor Carrier for Microwave Applications (3,740,672)
- R. L. Pryor** Logic Circuit (3,739,193)
- J. A. Rajchman and W. F. Kosonocky** Electrically and Optically Accessible Memory (3,742,464)
- R. S. Ronen** Method of Making Semiconductor Device (3,740,280)
- A. Schwarzmann** Self Loaded Uneven Power Divider (3,742,392)
- R. S. Silver** Bistable Storage Device and Method of Operation Utilizing a Storage Target Exhibiting Electrical Breakdown (3,737,715)
- R. V. Tompkins** Wire Stripping Apparatus and Method (3,739,818)
- H. R. Warren** Recording Web Transport Apparatus (3,739,969)
- D. H. Willis** Horizontal Oscillator Control for Plural Operating Mode Television Receivers (3,740,489)
- D. H. Willis** Video Amplifiers (3,742,376)

AUTHORS



John P. Carroll graduated from RCA Institutes T-3 program in 1965. In 1966, he joined the RCA Astro Electronics Division and in 1968 transferred to RCA Laboratories where he is currently a member of the RCA Electronic Components Electro-Optics laboratory. He has worked on the development of the silicon vidicon mosaic target and on epitaxial growth of silicon layers.



A. Danforth Cope received the B.A. degree from Colgate University in 1938 and continued in graduate study at Yale University. He joined RCA in 1941 as a manufacturing process and development engineer working with gas-filled phototubes and television camera tubes at the Harrison, N. J., and Lancaster, Pa. plants. Mr. Cope was liaison engineer in carrying the image orthicon from research into production during 1943 and 1944. He continued to be concerned with image orthicon processing improvements until 1949 when he transferred to RCA Laboratories, Princeton, N. J. From 1949 to 1960, Mr. Cope was engaged in research related to television camera tubes, particularly the photoconductor problems related to the vidicon. Late in 1960, Mr. Cope joined the Physical Research Group of RCA Astro Electronics Division to continue work on photoconductor materials and their application in image sensing systems. From 1966-1972, as a member of the Electro-Optics Laboratory of RCA Electronic Components, Princeton, N. J., he continued the same line of activity. Mr. Cope served as project engineer in a research study of electron optics of the Image Isocon, and was part of the team concerned with the development of the silicon mosaic target for the vidicon and the silicon intensifier target tube. His most recent project has been the development of a silicon cold cathode for a vidicon tube. At present Mr. Cope is assigned to the Process and Applied Materials Research Laboratory of RCA Laboratories.

Mr. Cope is a member of Sigma Xi and the Optical Society of America. He was the recipient of RCA Laboratories Achievement Awards in 1950, 1957, and 1968.



John L. Druguet received the BSEE degree from Villanova University in 1968. He is currently attending Villanova working toward his MSEE degree. Mr. Druguet joined RCA Laboratories in 1969 where he has worked on plated wire and disk file memories and on optical detection of bubble domains for domain memories. He is currently a member of the physical electronics research laboratory. Mr. Druguet is a member of IEEE.



Alvin Malcolm Goodman attended the Drexel Institute of Technology, Philadelphia, Pa., and received a B.S.E. in 1952. He did graduate work at Princeton University, receiving an M.A. in 1955 and a Ph.D. in 1958. From June 1956 to January 1957 he served as Research Assistant at Princeton University, and then as Assistant Professor of Electrical Engineering at the Case Institute of Technology up to June 1959. He performed research at RCA Laboratories as a summer employee in 1954, 1955, and 1958. He has been a Member of the Technical Staff since June 1959. Dr. Goodman has specialized in solid-state physics. His thesis

subject was "Dember Effect and Trap Levels in Silver Chloride". He has received two RCA Laboratories Achievement Awards for work on metal-semiconductor contacts (1963) and MNOS (metal-nitride-oxide-silicon) memory devices (1969).

He is a member of the American Physical Society, Sigma Xi and the Institute of Electrical and Electronics Engineers, and is listed in American Men of Science.



Karl G. Hernqvist graduated in Electrical Engineering at the Royal Institute of Technology, Stockholm, Sweden, in 1945. He received the Licentiate of Technology degree in 1951 and the Doctor of Technology degree in 1959. From 1946 to 1952 he was employed by the Research Institute of National Defense in Stockholm, working in the field of microwave electronics. From 1948 to 1949, Dr. Hernqvist was a trainee of the American-Scandinavian Foundation at RCA Laboratories, to which he returned in 1952; he is presently working on gas lasers. Dr. Hernqvist is a Member of the Institute of Electrical and Electronics Engineers and Sigma Xi.



Lorne Keyes graduated in 1954 with a BSc in electrical engineering from Queen's University. He has been continuously employed at RCA Ltd., Montreal, since that time in the field of telecommunication and satellite systems engineering. His responsibilities have included design and systems engineering of VHF transceivers, UHF troposcatter, and heavy route microwave telephony. He was engaged on design and system engineering for the NASA Relay Communications satellite, the ISIS-A and ISIS-B scientific satellites and more recently the Canadian Communications technology satellite (CTS). He has participated in numerous

communications satellite studies and proposals and is currently a staff engineer in the Aerospace department concerned mainly with Domestic satellite communications.

He is a member of the Quebec Corporation of Engineers, The Engineering Institute of Canada, and the IEEE.



Chandra M. Kudsia received his B.Sc degree with honors in Physics from Delhi University in 1961; B.E. degree with distinction in Electrical Communication Engineering from Indian Institute of Science, Bangalore, in 1964 and M.S. degree in Electrical Engineering from McMaster University, Hamilton, Ontario in 1966. After a year with Amphenol Canada Limited, Toronto, he joined the Antenna Group of RCA Limited in May 1967. At RCA, he worked on the design of microwave components and sub-systems for high quality microwave radio-relay links and ground stations for satellite communications. In 1969, he joined the Aerospace Group

where he participated in the conceptual and project definition phase of the ANIK satellite and the Communications Technology Satellite (CTS). At present he is involved in the hardware phase of the SHF Transponder for CTS and advance development work in the area of transponders for the U.S. Domestic Communications Satellite. In January 1973, he was appointed to the position of Senior Member of Technical Staff.

Mr. Kudsia is a member of IEEE.



B. J. Levin received the BSEE degree from Drexel University in 1964, a MSEE degree from MIT in 1965, and a PhD in Electrical Engineering from the University of Pennsylvania in 1969. He worked on the design of digital circuits on the Early Bird Satellite program at Bell Telephone Laboratories in 1964. In the summer of 1966, he worked on the development of GaAs microwave diode avalanche oscillators as a member of the technical staff of the RCA Laboratories. In the summer of 1967 he worked on frequency locking of microwave diode avalanche oscillators at American Electronics Laboratories. In September 1967 he became a Research Associate at the Moore School of Electrical Engineering. He was concerned with various theoretical and experimental problems of millimeter wave imaging. His dissertation was a detailed analysis of the reflection mode-photoconductive readout millimeter wave image converter. In July 1969 Dr. Levin joined the Applied Physics Laboratory of RCA's Advanced Technology Laboratories in Camden, N. J. At ATL he has continued his investigation of millimeter wave imaging techniques. His work has included extending the imaging system to higher frequencies, the study of various readout techniques, the experimental imaging of complex targets, and various quasi-optical approaches to improving the target recognition ability of the imaging system. Since July 1970, he has also made a major contribution to the development of an electronically controlled low-loss phase shifter operating in the 100 GHz region. Recently, Dr. Levin has worked on the development of high power, high efficiency GaAs Impatt diodes at RCA Laboratories in Princeton, N. J. and on the Combat Theater Ground Communications (CTGC) study program conducted by RCA Government Communications Systems.

Dr. Levin is a member of the IEEE, Sigma Xi, Tau Beta Pi, Eta Kappa Nu, and Phi Kappa Phi.



Eduard Luedicke received his degrees in Electrical Engineering from the Technical University at Berlin and at Karlsruhe, West Germany—the Diplom Engineer in 1950, the Doctor degree (*summa cum laude*) in 1955. From 1941 to 1945, he was a development engineer for radar and guidance techniques in the Telefunken Laboratories, Berlin, Germany and from 1951 to 1955 a development engineer in the field of industrial television at the Zentral Laboratorium of Siemens in Karlsruhe, West Germany. In 1955 he joined the RCA Victor Company Ltd., Montreal, Canada as a development engineer for television components. He was appointed

manager of engineering of the RCA Victor Renfrew Plant in Canada in 1956. In 1959, Dr. Luedicke transferred to the RCA Solid State Division, Somerville, N. J., working initially on micromodules and later on a computer in the 1000 megacycle range. From 1962 to 1967, Dr. Luedicke was a member of the Astro-Electronics Division, working on television camera tubes for use in space applications and in studies of astronomy. In 1967, he transferred to the Electro-Optics Laboratory at the David Sarnoff Research Center in Princeton, N. J., where he has made extensive studies of the dynamic characteristics of camera tubes at various scan rates and contributed to the development of TV storage tubes and the double-gun vidicon. Most recently, he has been working on a cold cathode vidicon. He received an RCA Laboratories Outstanding Achievement Award and an IR100 Award in 1971, and is presently a member of the television systems research group at RCA Laboratories.

Dr. Luedicke is a member of Fernseh Technische Gesellschaft, Germany, and of SMPTE.



L. J. Nicastro received the BA in Physics from La Salle College in 1953, the MS in Radiation Biology from the University of Rochester in 1956, and the Ph.D. in Physics from Temple University in 1970. Dr. Nicastro was an instructor in Chemistry and Physics at La Salle College, 1953-1954; a Physicist in Ballistics at the Frankford Arsenal, 1954-1955; and a Health Physicist at the Brookhaven National Laboratories during the summer of 1956. From 1956 to 1959, he worked in the Neutron Physics Section of the National Bureau of Standards on neutron spectrometry, measurements of neutron age, and the response of various scintillators to alpha particles.

Since coming to RCA early in 1959, Dr. Nicastro has done experimental work in the areas of gaseous molecular frequency standards, laser radar, and measurement of plasma properties using lasers. Dr. Nicastro has been involved in experimental and analytical studies in the general area of display techniques, including modulation of light by means of magneto-optic rotators and electro-optic crystals, laser displays, and measurements of the negative resistance effect in cadmium selenide powders. Recently, Dr. Nicastro has been engaged in work on the development of liquid-crystal displays.



Valentine O'Donovan graduated as an electrical engineer from the Cambridge College of Technology in England in 1959. He joined RCA Limited in 1963. From 1965 to 1969 he was a Group Leader in charge of a development group responsible for the design of microwave devices and sub-systems for Radio Relay and Satellite Earth Terminal products. In 1964 he joined the Aerospace Engineering Dept. and is currently the Supervisor of an engineering group responsible for the design of microwave Transponders for Communications Satellite Applications.

Mr. O'Donovan is a member of the IEEE and is registered as a professional engineer in the Province of Quebec, Canada.



Elmer L. Offenbacher is Professor of Physics at Temple University in Philadelphia, Pa. He joined the Temple faculty after completing work for his Ph.D., at the University of Pennsylvania in 1951, on the Theory of the Directional Effects of Electric Breakdown in Ionic Crystals. He also taught an extension course in Solid State Physics at RCA in Camden, N. J. He has supervised a number of ph.D. theses from engineers at various RCA installations. He has worked in the field of Electron Spin Resonance and most recently on mechanical properties of single crystals of ice.



Barry S. Perlman received the B.E.E. from the City College of New York in 1961 and the M.S.E.E. and the Ph.D. in Electrophysics from Brooklyn Polytechnic Institute in 1964 and 1973 respectively. From 1961 to 1968 he was a member of the staff of the RCA Advanced Communications Laboratory in New York City, becoming a senior member of the technical staff in 1966. He was primarily concerned with advanced receiver techniques such as the development of all solid state microwave troposcatter and relay subsystems, airborne X-band receivers, integrated circuits, high level parametric circuits, dielectric and superconducting microwave filters, and fabrication and application of Si avalanche devices. In June of 1968 he joined the Microwave Technology Center at the RCA David Sarnoff Research Center, Princeton, New Jersey, as a member of the technical staff, where he is presently working on the microwave applications of active GaAs semiconductors, computer aided design (CAD) and advanced measurement techniques. In 1969 he received an engineering achievement award for his part in the development of advanced microwave devices, and in 1970 he was the recipient of an RCA Laboratories Outstanding Achievement Award for a team effort in the development of wideband GaAs transferred electron amplifiers.

Dr. Perlman is a member of Sigma Xi, the IEEE, and NYSSPE.



Rabah Shahbender is head of the Applied Electronics Research, Physical Electronics Research Laboratory, RCA Laboratories, Princeton, N. J. He received the BEE from Cairo University, Cairo, Egypt, the MSEE from Washington University, St. Louis, Missouri, and the PhD from the University of Illinois. From 1946 to 1948, he worked for the Anglo-Egyptian Oilfields Ltd. in seismic exploration. From 1951 to 1955, he was on the staff of Honeywell Controls Division where he conducted research in the behavior of nonlinear closed loop systems. He joined RCA in Camden in 1955 and worked in the areas of adaptive systems, nonlinear

filters, electron beam devices, ultrasonic devices, and airborne fire control systems. He transferred to RCA Laboratories in 1959, and has been active in the area of digital devices and systems. In 1961 he was appointed Head, Digital Research. Dr. Shahbender received the AFIPS Best Paper Award in 1963, IR-100 Awards in 1964 and 1969, and RCA Laboratories Achievement Awards in 1960 and 1963. From 1960 to 1966 he was Chairman of the Department of Electronic Physics, at La Salle College, Evening Division. Dr. Shahbender is a Fellow of IEEE, a member of AAAS, Sigma Xi and Eta Kappa Nu, and a Fellow of the University of Illinois.



Gary G. Weidner received the BSEE degree from the Milwaukee School of Engineering in 1965, and the MSEE degree from the University of Pennsylvania in 1972. Mr. Weidner has worked extensively in the field of low-noise microwave amplifiers, particularly in the development of wideband traveling-wave masers, and is currently involved in the development of various millimeter wave technologies. He is a Senior Member of the Engineering Staff, RCA Advanced Technology Laboratories.

